Lappeenranta
University of Technology

Ming Li

STIFFNESS BASED TRAJECTORY PLANNING AND FEEDFORWARD BASED VIBRATION SUPPRESSION CONTROL OF PARALLEL ROBOT MACHINES

Supervisors   Professor Heikki Handroos
Laboratory of Intelligent Machines
Department of Mechanical Engineering
Lappeenranta University of Technology
Finland

Associate Professor Huapeng Wu
Laboratory of Intelligent Machines
Department of Mechanical Engineering
Lappeenranta University of Technology
Finland

Reviewers   Professor Gangbing Song
Smart Materials and Structures Laboratory
Department of Mechanical Engineering
University of Houston
USA

Associate Professor Luc Rolland
Faculty of Engineering and Applied Sciences
Memorial University of Newfoundland
Canada

Opponents   Professor Gangbing Song
Smart Material and Structures Laboratory
Department of Mechanical Engineering
University of Houston
USA

Associate Professor Luc Rolland
Faculty of Engineering and Applied Sciences
Memorial University of Newfoundland
Canada

ABSTRACT

Ming Li

Stiffness based trajectory planning and feedforward based vibration suppression control of parallel robot machines

The dissertation proposes two control strategies, which include the trajectory planning and vibration suppression, for a kinematic redundant serial-parallel robot machine, with the aim of attaining the satisfactory machining performance.

For a given prescribed trajectory of the robot's end-effector in the Cartesian space, a set of trajectories in the robot's joint space are generated based on the best stiffness performance of the robot along the prescribed trajectory.

To construct the required system-wide analytical stiffness model for the serial-parallel robot machine, a variant of the virtual joint method (VJM) is proposed in the dissertation. The modified method is an evolution of Gosselin's lumped model that can account for the deformations of a flexible link in more directions. The effectiveness of this VJM variant is validated by comparing the computed stiffness results of a flexible link with the those of a matrix structural analysis (MSA) method. The comparison shows that the numerical results from both methods on an individual flexible beam are almost identical, which, in some sense, provides mutual validation. The most prominent advantage of the presented VJM variant compared with the MSA method is that it can be applied in a flexible structure system with complicated kinematics formed in terms of flexible serial links and joints. Moreover, by combining the VJM variant and the virtual work principle, a system-wide analytical stiffness model can be easily obtained for mechanisms with both serial kinematics and parallel kinematics. In the dissertation, a system-wide stiffness model of a kinematic redundant serial-parallel robot machine is constructed based on integration of the VJM variant and the virtual work principle. Numerical results of its stiffness performance are reported.

For a kinematic redundant robot, to generate a set of feasible joints' trajectories for a prescribed trajectory of its end-effector, its system-wide stiffness performance is taken as

the constraint in the joints trajectory planning in the dissertation. For a prescribed location of the end-effector, the robot permits an infinite number of inverse solutions, which consequently yields infinite kinds of stiffness performance. Therefore, a differential evolution (DE) algorithm in which the positions of redundant joints in the kinematics are taken as input variables was employed to search for the best stiffness performance of the robot. Numerical results of the generated joint trajectories are given for a kinematic redundant serial-parallel robot machine, IWR (Intersector Welding/Cutting Robot), when a particular trajectory of its end-effector has been prescribed. The numerical results show that the joint trajectories generated based on the stiffness optimization are feasible for realization in the control system since they are acceptably smooth. The results imply that the stiffness performance of the robot machine deviates smoothly with respect to the kinematic configuration in the adjacent domain of its best stiffness performance.

To suppress the vibration of the robot machine due to varying cutting force during the machining process, this dissertation proposed a feedforward control strategy, which is constructed based on the derived inverse dynamics model of target system. The effectiveness of applying such a feedforward control in the vibration suppression has been validated in a parallel manipulator in the software environment. The experimental study of such a feedforward control has also been included in the dissertation. The difficulties of modelling the actual system due to the unknown components in its dynamics is noticed. As a solution, a back propagation (BP) neural network is proposed for identification of the unknown components of the dynamics model of the target system. To train such a BP neural network, a modified Levenberg-Marquardt algorithm that can utilize an experimental input-output data set of the entire dynamic system is introduced in the dissertation. Validation of the BP neural network and the modified Levenberg-Marquardt algorithm is done, respectively, by a sinusoidal output approximation, a second order system parameters estimation, and a friction model estimation of a parallel manipulator, which represent three different application aspects of this method.

ACKNOWLEDGEMENTS

Like most doctoral students, I did not carry out my research in isolation in a wild cave. Consequently, many hearts and minds contributed to the accomplishment of my doctoral study and this dissertation.

First, I would like to express my deepest gratitude to my supervisors, Professor Heikki Handroos and Associate Professor Huapeng Wu, for supporting me during these past five years. I am very grateful to Professor Handroos and Associate Professor Wu for providing me with the opportunity to study as a doctoral student in the Laboratory of Intelligent Machines, and for all their subsequent help: for organizing the financial support of my research; and for their inspiring guidance, valuable suggestions and constant encouragement throughout my studies.

Professor Heikki Handroos is an excellent model and an example of a successful scientific researcher and professor. I am very thankful to him for giving me the maximum freedom to do the research I wanted, while at the same time continuing to contribute valuable feedback, advice and encouragement. Besides the science, his skills and excellent performances on the guitar introduced me to another colorful world.

Associate Professor Huapeng Wu is someone you will instantly love and never forget once you meet him. He is also a man you can always speak to whenever you are faced with a problem, no matter in research or daily life. He is one of the smartest people I know. His precise insights, extensive expertise and wide-ranging experience always bring inspiration and help in finding a way to overcome any adversity. The joy, enthusiasm, selflessness and sacrifice he has for his research and daily life are contagious and motivational, even during the tough times.

I am extremely appreciative of my dissertation reviewers and opponents, Professor Gangbing Song and Associate Professor Luc Rolland, for their constructive and insightful comments and suggestions, which were a great help and improved the quality of the dissertation considerably. A big thank you goes to Mr. Peter Jones for his help with the language of the dissertation. His detailed comments and corrections improved the dissertation immeasurably.

CONTENTS

LIST OF PUBLICATIONS

As an outcome of the research work related to the dissertation, there are eight published scientific peer reviewed articles, among which five refereed articles are selected to comprise the main contents of the dissertation (indicated by asteroid), while the rest three are listed as the supplementary materials:

Refereed scientific journal articles

1*. Wu Huapeng, Wang Yongbo, Li Ming, Al-Saedi Mazin, Handroos Heikki. Chatter suppression methods of a robot machine for ITER vacuum vessel assembly and maintenance. *Fusion Engineering and Design*, Volume 89, Issues 9-10, October 2014, Pages 2357-2362. (Principle article of dissertation)

2*. Li Ming, Wu Huapeng, Handroos Heikki. Static stiffness modeling of a novel hybrid redundant robot machine. *Fusion Engineering and Design*, Volume 86, Issues 9-11, October 2011, Pages 1838-1842. (Principle article of dissertation)

3. Li Ming, Wu Huapeng, Handroos Heikki, Yang Guangyou. Software design of the hybrid robot machine for ITER vacuum vessel assembly and maintenance. *Fusion Engineering and Design*, Volume 86, Issues 9-10, October 2013, Pages 1872-1876. (Supplementary article of dissertation)

4. Yang Guangyou, Li Ming, Zhang Daode, Xu Wan. Ethernet interface of high speed data acquisition system based on ARM-FPGA. *Advanced Science Letters*, Volume 4, Issue 6-7, Pages 2538-2542, 2011. (Supplementary article of dissertation)

5. Wu Huapeng, Handroos Heikki, Lehtonen JT, Pale P, Li Ming. Manufacturing of the ITER TF coils radial plates by means of P/M HIP and a hybrid machining center. *Fusion Engineering and Design*, Volume 86, Issue 6-8, 2011, Pages 1369-1372. (Supplementary article of dissertation)

Refereed conference articles

6*. Li Ming, Wu Huapeng, Handroos Heikki, Ceccarelli Marco, Carbone Giuseppe. Vibration control for parallel manipulator based on the feedforward control strategy. *ASME Conference Proceedings, Volume 4B: Dynamics, Vibration and Control*. ASME 2013 International Mechanical Engineering Congress and Exposition, San Diego, California, USA, November 15–21, 2013. (Principle article of dissertation)

7*. Li Ming, Wu Huapeng, Handroos Heikki. Stiffness-maximum trajectory planning of a hybrid kinematic-redundant robot machine. *Proceedings of IECON 2011* - 37th Annual

Conference on IEEE Industrial Electronics Society, Melbourne, Australia, November 7-11, 2011. (Principle article of dissertation)

8*. Li Ming, Wu Huapeng, Handroos Heikki. Stiffness modelling of hybrid parallel robot machine. *Proceedings of IMCM 2010, Volume 54, Pages 743-750*, International Chemnitz Manufacturing Colloquium, Chemnitz, Germany. (Principle article of dissertation)

LIST OF FIGURES

LIST OF TABLES

LIST OF SYMBOLS AND ABBREVIATIONS

ALANN	Functional Link Artificial Neural Network
ANN	Artificial Neural Network
BP	Back Propagation
CR	Crossover Rate of the DE Algorithm
D	Individual Index of the DE Algorithm
DE	Differential Evolution
DH	Denavit-Hartenberg
DOF	Degree of Freedom
F	Mutation Scale Factor of the DE Algorithm
ITER	International Thermonuclear Experimental Reactor
IWR	Intersector Welding/Cutting Robot
LM	Levenberg-Marquardt
MLP	Multilayer Perceptron
MSA	Matrix Structural Analysis
RBFNN	Radial Basis Function Neural Network
RMS	Root Mean Square
TIG	Tungsten Inert Gas
VJM	Virtual Joint Method
VV	Vacuum Vessel

PART I: OVERVIEW OF THE DISSERTATION

CHAPTER 1

INTRODUCTION

1.1 Background and Motivation

The research work presented in this dissertation arises from control strategy development for a hybrid serial-parallel kinematic redundant robot machine, the IWR (Intersector Welding/Cutting Robot) used for the ITER (International Thermonuclear Experimental Reactor) vacuum vessel (VV) assembly and maintenance [1]-[4]. The elements of the control strategy discussed in the dissertation mainly encompass two aspects: trajectory planning in the joint space for a prescribed trajectory of the robot end-effector and a feedforward control method used to suppress chatter vibration of the robot during the machining process. The aim of the work is to obtain better machining and handling performance to meet the demanding requirements of ITER VV manufacture.

Fig.1 shows ITER's vacuum vessel, which presents a toroidal form from an overall perspective and consists of nine sectors from the manufacturing point of view.

a) Vacuum vessel of ITER   b) Sector
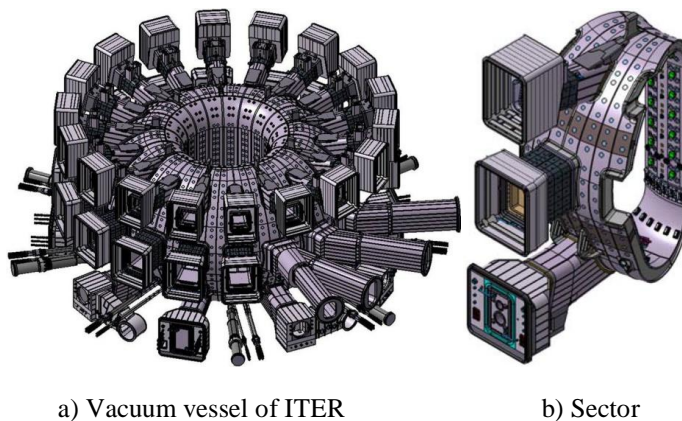
Fig.1 Vacuum vessel of ITER. (19 meters across by 11 meters high.)

There exists an approximate 60 mm wide gap between any two adjacent sectors of the vacuum vessel when all the sectors have been placed together in preparation for further assembly work. In order to join the adjacent sectors together seamlessly, a mobile robotic machine that can carry out the welding and machining work over the gap area from inside the VV would appear to be the most promising solution.

To achieve such a task, the robotic machine must possess multi-function capabilities, which include the integration of the handling functions for a heavy splice plate, heavy TIG (tungsten inert gas) welding tool set and laser welding tool set, and the milling, drilling and threading functions on hard materials and parts, such as the stainless steel and tungsten stuffing slice.

CHAPTER 1

According to the manufacturing requirements of ITER VV, the positioning tolerance for material handling is required to be under $\pm$ 0.1 mm for a handling payload that may reach around a maximum of 150 kg; concurrently, to guarantee a satisfactory machining surface quality over the welded area, the trajectory tracking accuracy of the cutting tool bit is expected to be under 0.01 mm for machining work implemented on hard splicing materials; and the workspace of the machining device should reach all the inner surface of the VV sector.

To meet these stringent requirements in the manufacture of ITER VV, a hybrid serial-parallel 10 DOF robot machine – IWR (Intersector Welding/Cutting Robot) – has been developed in the Laboratory of Intelligent Machines, Lappeenranta University of Technology, Finland, who is also one of the official European Union participants in ITER.

To be able to handle the heavy materials involved and produce a satisfactory finished result when machining the complex contoured inner surface of the VV sectors, the key requirements of high payload ability, high stiffness performance and high dexterity have to be taken into account and embraced in design of the robot machine, IWR. To meet these aims, a well-known parallel structure – the Stewart platform – was adopted as the front-end of IWR, which is hydraulically driven in view of the heavy payload ability required and the need to be contamination-free. Such platform inherits the intrinsic high stiffness characteristics of a parallel structure and can provide 6 DOF motion to the end-effector, which endows the robot with the dexterity needed to machine free-from surfaces.

To overcome the weakness of the small workspace intrinsic to this parallel platform structure and thus meet the large workspace requirement of manufacturing the ITER VV, a compact 4 DOF serial structure based carriage was added, to which the Stewart platform is attached. Fig.2 shows the prototype of IWR and its in-situ working position.
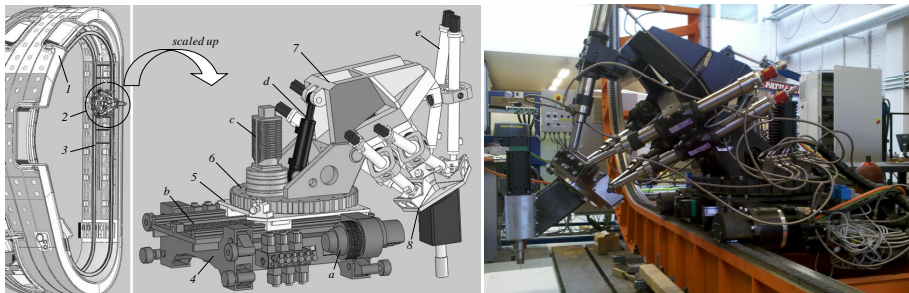
1. Vacuum vessel sector   2. Hybrid robot   3. Track   4. Carriage base   5. Moving plate   6. Rotation table   7. Stewart base   8. End-effector

a. Driving motor on track   b. Linear movement motor for moving plate   c. Rotation drive motor   d. Tipping driven cylinder   e. Stewart driving cylinder

Fig.2 10DOF IWR for assembly and maintenance of ITER VV: (i) vacuum vessel sector and (ii) robot used for the assembly and maintenance of vacuum vessel

CHAPTER 1

The serial structure based carriage is mounted on a track equipped with racks, which forms a closed loop path around the inner surface of the sector. The 4 DOF carriage consists of the following motions: travel along the racks, driven by pinion; linear movement perpendicular to the racks, driven by ball screw; rotation around the direction vertical to the carriage plane; and tipping of the Stewart base by a hydraulically driven cylinder.

It is well known that to achieve the best surface finish in a machining process on a freeform surface, a 5-axes synchronized interpolation for the prescribed trajectory is a necessary requirement of the end-effector of the robotic machine. This demand however can be easily fulfilled by the 6 DOF Stewart platform. Indeed, the IWR possesses a total of 10 DOF in the driving joints, which presents a redundancy in the inverse kinematics for the prescribed trajectory. The issue thus arises how to solve the redundant inverse kinematics in the control strategy of such a robot machine.

On the other hand, although the parallel structure of IWR can generally provide high stiffness to its end-effector, the overall stiffness performance of the whole robot machine is dominated by the serial carriage, the stiffness of which can be quite low in some particular poses. The Stewart structure can also exhibit a low stiffness character under certain poses, such as in the pose of fully stretched out driving limbs. It is known that for a machine tool, stiffness is a very important factor in the attainment of good positioning accuracy, good surface finish and long cutting tool life, and thus, the stiffness performance must be taken into account and optimized in the control strategy of IWR.

Therefore, to accomplish a prescribed trajectory, it would be the best solution to conceive a control strategy that can not only solve the problem of redundant inverse kinematics in the trajectory planning in the joint space, but can also optimize the overall stiffness performance of the robot machine. The redundant kinematics of the robot implies that for a given location of end-effector, there exist multiple inverse kinematic solutions for the position of the driving joints that can form the various poses of the robot. Since the stiffness performance of IWR depends on the pose configuration of the robot, the stiffness can then be regarded as an objective of a cost function for an optimization in which the various poses, namely the position of redundant joints, are regarded as input variables. Therefore, the trajectory planning described in this work views the concept as follows: for the prescribed trajectories of end-effector in the station frame of IWR, the corresponding driving joints position values in the joint space of the robot are generated based on the determination of the driving positions of redundant joints, which are generated based on optimizing the overall stiffness performance of IWR.

Since the IWR carries out a machining task on hard material (tungsten), the cutting force is considerably larger than on commonly used materials such as aluminum, steel etc. The varying cutting force required for such machining causes chatter vibration in the end-

effector during the machining process, which not only leads to a deterioration in the trajectory tracking accuracy, but also jeopardizes the functional life of the cutting tool and the robot's passive joints as well as damaging the welded area in the VV sector.

Based on the stiffness optimized trajectories generated in the joint space, the control strategy needs to be further investigated to ensure that it is able to suppress the chatter phenomenon during the machining process. Feedforward compensation control, in which the external cutting force exerted on the tool bit is obtained and fed forward into the corresponding driving joints for driving force compensation, using an inverse dynamics model is a promising solution to achieve such an aim. The resulting extra output force on the end-effector will cancel out the effect of the corresponding cutting force. The critical issue in this feedforward method is accurate construction of the inverse dynamics model of the robot. Thus, the question of how to construct an accurate inverse dynamics model for such robot machines must be studied.

1.2 Objectives of the Study

The objective of the study consists of the following two parts:

a. To solve the redundant inverse kinematics problem for the prescribed trajectories of the end-effector of IWR and generate a set of feasible trajectories in the robot driving joint space. The maximum stiffness performance of IWR is taken as the optimization objective for the generation of joint trajectories so as to guarantee optimal machining performance from the static point of view.

b. To develop a control strategy to suppress chatter vibration in the end-effector of IWR during the machining process and thus ensure a satisfactory finished surface from the dynamic point of view. To meet this aim, an effective feedforward force compensation method needs to be developed.

1.3 Contributions to the Field

The main contribution of this dissertation work lies in the development of control strategies for a redundant kinematic robot machine that aim to deliver optimal machining performance. The definition of control strategies in the dissertation straddle two aspects: 1. trajectories planning/generation in the joint space when a prescribed trajectory of the end-effector of the robot is given; 2. a feedforward control strategy for trajectory tracking that is used in addition to feedback control to suppress chatter vibration caused by external disturbance forces.

Specifically, the contribution consists of the following original contributions, which were developed in the course of the dissertation work:

a. A method of constructing an analytical stiffness model for a hybrid serial-parallel robot is proposed. A variant of the virtual joint method (VJM) is developed for stiffness calculation of flexible links. The principle of virtual work is employed to evaluate the stiffness for combined structures – the serial-parallel robot -- based on the component stiffness computed by VJM. The final obtained stiffness model for the hybrid serial-parallel robot is analytical- and computation-efficient and can easily be used for stiffness evaluation in any deflection direction as well as in stiffness optimization for redundant kinematics robots.

b. A new idea for trajectories generation in the driving joint space of redundant kinematics robots is introduced for cases when the prescribed trajectory of the robot end-effector is given. The trajectories in the joint space generated are termed maximum stiffness trajectories in the dissertation, are determined by the positions of redundant driving joints, and are obtained by optimizing the system-wide stiffness performance of the robot machine.

c. A feedforward control strategy that is based on the derived inverse dynamics model of a parallel manipulator is developed to suppress vibration phenomena of the end-effector of the robot caused by varying external disturbance forces. The disturbance force exerted on the end-effector of the robot is fed forward into the controllers of the joint actuators, which consequently yield an additive compensation driving force against the effect of disturbance.

d. A modified Levenberg-Marquardt (LM) algorithm is introduced for training of the back propagation (BP) neural network in the dissertation. A new concept of utilizing the BP neural network to identify the unknown components of the dynamics of the mechanical system is proposed based on the modified Levenberg-Marquardt algorithm. Such a modified LM algorithm can utilize the input-output data of the whole dynamics system to train a BP neural network constructed to approximate the unknown parts of the whole system. An accurate inverse dynamics model of a parallel manipulator is derived by incorporating the neural network into the model when the friction models of the joints in the inverse dynamics of the parallel manipulator are deemed as the unknown components.

1.4 Organization of the Dissertation

The dissertation consists of two parts: the first part constitutes the larger part of this dissertation and gives an introductory overview of the subject of study and presents the findings of the research; the second part is composed of two original peer reviewed scientific journal papers and three peer reviewed conference papers.

For better understanding of the dissertation, the structure of the first part of the dissertation, which consists of five chapters, is briefly described

CHAPTER 1

In chapter 2, the theoretical background of this dissertation is introduced. The chapter consists of four sub-sections, which cover four different topics, namely: stiffness modelling, trajectory planning, vibration suppression and dynamic model identification. A short literature review of the state-of-the-art of theoretical knowledge of these topics is given, and related innovations presented in the dissertation are introduced.

In chapter 3, stiffness based trajectory planning in the robot's driving joints is introduced for a prescribed trajectory of the end-effector of IWR. The stiffness model of the hybrid robot machine is investigated by employing matrix structural analysis (MSA), a variant of VJM and the virtual work principle. Numerical results of stiffness performance over a specified workspace of IWR are given. By employing a differential evolution (DE) algorithm in which the stiffness performance is taken as the optimization objective, feasible trajectories in the robot's driving joints are generated, along which the maximum stiffness performance of IWR for the prescribed trajectory of end-effector is obtained. Numerical results of the trajectories generated in the driving joints' space are also presented.

Chapter 4 introduces the feedforward control strategy for vibration suppression of the robot machine, which is constructed based on an inverse dynamics model of the target robot. A case study for application of the proposed feedforward strategy with a parallel manipulator is given. Issues related to construction of accurate inverse dynamics models of such robots in practice are discussed in this chapter. To identify the unknown parts of the dynamics system, a new BP neural network structure is proposed, and a modified Levenberg-Marquardt (LM) algorithm is introduced for training of the BP neural network. For validation of the effectiveness of the proposed neural network and the modified LM training algorithm, three examples from different application points of view are presented.

Chapter 5 concludes the dissertation and proposes further research directions.

CHAPTER 2

STATE OF THE ART -- THEORETICAL BACKGROUND AND PROPOSED METHODS

The theories applied in this dissertation relate to four different areas. The stiffness based trajectory planning comprises elements of both stiffness modelling theory of mechanical systems and trajectory planning theory of robotics. Additionally, algorithm-based differential evolution (DE) from the discipline of soft computation is employed in the trajectory planning process for optimization of the stiffness performance. For vibration suppression control of the robotic machine, robust control theory is mainly employed. A feedforward control strategy is utilized, the premise of which is successful application of an accurately constructed inverse dynamics model of the robot system. Thus, dynamic model identification theory is introduced due to the existence of unknown components in the practical robot system. As a solution for the dynamics model, the application of an artificial neural network and its training algorithm for identification and approximation of the dynamic system are investigated.

2.1 Stiffness Modelling

Stiffness modelling theories of mechanical systems can be divided into two broad categories: matrix structural analysis (MSA) based methods and Jacobian matrix based methods [5]-[12][70]. The finite element method (FEM) can be used to compute the deflections of a mechanical structure if the external force is given, but it cannot obtain the analytical stiffness matrix/model directly, thus it is often used to validate analytical stiffness models constructed by MSA or Jacobian methods [13]-[16].

- **Matrix structural analysis and Jacobian methods**

In the MSA method, a mechanical structure is divided into several elements and nodes. By applying the superposition principle, a final analytical stiffness matrix can be formed by assembling all the stiffness matrices of the elements in an order that reflects the relationship between the external force being exerted on the nodes and the corresponding deflections of the nodes [17][18]. Clinton et al. (1997) have used the method to derive a system-wide stiffness model of a Hexapod milling machine, and the modelling results present a 9.0% error compared with experimental measurements [19]. The most probable reason for the error is the postulation that the entire structure of the Hexapod machine can be regarded as being constructed by 25 pin-jointed trusses, a number which could be considered as being insufficient. However, if the number of postulated trusses is increased significantly, a heavy calculation cost would be introduced. From the numerical results of Clinton et al., it can be concluded that MSA modeling is more suited to small size mechanisms that consist of a limited number of nodes and elements, rather than entire robotic structures.

CHAPTER 2

Use of the Jacobian method in the stiffness modelling of robotics has been intensively studied by Tsai [12]. In his stiffness modelling, the major links in industrial robots are assumed to be perfectly rigid, and the compliance of the robot is mainly contributed by the mechanical transmission mechanisms and control systems, which finally appears as the compliance of the actuating joints of the robot. In the practical application of IWR studied in this dissertation, due to the heavy payload exerted on the end-effector, the deflection of the links in the robot cannot be ignored, especially the deflection from the base of the Stewart platform. Thus, the Jacobian method proposed by Tsai needs to be modified to account for the links deformations. In 2000, Gosselin et al. [20] proposed a new stiffness modelling method based on a so-called lumped model. This approach accounts for the flexibilities of both joints and links. In this lumped model, the flexibility of a link is equivalent to the flexibility of a virtual torsional spring in the joint, assuming that the torsional spring joint produces the same tip deflection as the flexible link. The Jacobian method is then used on the basis of this lumped model and a final stiffness model of the target robot obtained that encompasses flexibilities from both joints and links. However, such a lumped model can lead to a different orientation deformation of the link tip. If the link length is large, and the links are connected serially, then the accumulated orientation error cannot be ignored. Moreover, the lumped model only accounts for links deformation along the directions of DH joints, whereas in practice a deformation could occur in any direction of a link.

- **Proposal of the variant of the virtual joint method**

The lumped modelling approach of Gosselin is referred to as a virtual joint method (VJM) since it converts the flexible manipulator components (links, joints and actuators) into equivalent virtual localized spring joints. The concept of VJM is employed in this dissertation, but with a modification that results in a novel variant of VJM. The link deformation in this VJM variant is represented by the displacement of a virtual joint that is attached to the end-tip of the link rather than the start-tip of the link as in the original VJM, which accounts for both translational and orientation deformations at the link's end-tip. The deflection of the link is computed based on the link's stiffness matrix, which is obtained by applying the MSA method. The term of link in this case refers to links in general and thus not only represents a simple slender beam, but can also refer to a composite frame structure as well as a small kinematic chain. Then the system-wide stiffness model of IWR can be obtained by employing the virtual work principle on the virtual joints. The stiffness modelling method proposed in the dissertation consequently encompasses both MSA and Jacobian approaches: the former in derivation of a numerical stiffness matrix of an individual link for application in a virtual joint in a cost-efficient calculation, due to the reduced number of assumed nodes and elements, which nevertheless provides satisfactory accuracy; while the latter, which is essentially deduced

from the virtual work principle, integrates the link deformations into an analytical system-wide stiffness model.

2.2 Trajectory Planning

The concept of trajectory in robotics refers to a geometric path for the robot end-effector under a time law in the Cartesian space, which usually covers a number of via points of interest for a specific application [21]-[23]. Based on the number and distribution of the via points in the path, the trajectory can be classified into two categories: the discrete point-to-point trajectory and the continuous trajectory. It should be noticed that the concept of point-to-point trajectory as used in this dissertation can include several via points in the trajectory, whereas in other literature the point-to-point trajectory refers to a path giving only the initial and final points. The term continuous trajectory as used in this dissertation refers to a geometric path that contains a large number of sequential via points. Such a continuous trajectory is often adopted in the contour machining process and the corresponding via points can be considered as continuous interpolation points in the control system.

Since the different types of trajectory impose different constraints on the motions of the end-effector and driving joints, the strategies or approaches applied in trajectory planning differ from one another.

- **Point-to-point trajectory planning**

For a point-to-point trajectory, a limited number of points of interest for a specific application are prescribed for the end-effector of the robot to pass through, which are often sparsely distributed in the workspace, and the motions of the end-effector at each via point are often constrained by a desired position value under a time law or by a specific velocity and acceleration profile [24]-[26]. Such point-to-point trajectories are often adopted in material handling applications of industrial robots. In practice, the eventual user of such robots is primarily concerned with the motions of the end-effector at the via points of interest, thus the motions between the via points are not specified. The trajectory planning as studied herein refers to generating a geometric path for the end-effector of a robot that not only passes through all the via points of interest with constraints-satisfactory motions but also optimizes the kinematic or dynamic performance of the robot during the motions between the via points. Usually, it is desirable for the motion of the robot to be smooth, thus the cubic polynomial spline is often utilized for trajectory planning between two via points. In consideration of the productivity demand of an industrial robot, minimum time or energy cost trajectories are also often planned for the motions between the via points.

When a set of via points of interest is given, the point-to-point trajectory is also called a prescribed trajectory; however, such a prescribed trajectory is actually incomplete or not

strictly stipulated in the Cartesian space due to the existence of a great variety of motion planning between the via points of interest. Nevertheless, the point-to-point trajectory planning mainly focuses on the path generation of the end-effector in the Cartesian workspace.

However, for robotic machine applications, the prescribed trajectory of the robot end-effector is fully specified by the continuous interpolation points in the contour machining process, thus the trajectory planning in the robotic machine takes place in the joint space under the constraint of inverse kinematics, and the trajectory planning strategy differs from that applied in point-to-point motion of the end-effector.

- **Joint trajectory planning of robotic machine**

For a robotic machine, the most significant characteristic in consideration of trajectory planning is the system-wide stiffness performance, since it can directly affect actions like machining precision. Taking maximum stiffness performance as the optimization objective, Pugazhenthi et al. [27][28] studied optimal trajectory planning for a hexapod machine tool during continuous contour machining for the case that locating the prescribed contour trajectory in the workspace of the machine tool is deemed as a redundant freedom that determines the pose of machine tool as well as the stiffness performance of the entire machine. Clinton et al. [19] considered the same task, i.e. stiffness based tool path planning, for a Stewart-platform based milling machine.

For the IWR in this dissertation, four redundant kinematic DOF exist in the joint space, therefore for a prescribed contour trajectory in the Cartesian workspace of the end-effector, an infinite number of inverse solutions are admissible in the corresponding joint position values, which consequently can form an infinite number of poses and present an infinite number of stiffness performance values in each interpolation point of the prescribed trajectory. As a result, trajectory planning in this dissertation means that for a given contour trajectory of the IWR end-effector, a set of optimized trajectories in the IWR joint space is generated inversely, which, on the one hand, execute the robot's end-effector in the prescribed contour trajectory and, on the other hand, provide the maximum stiffness performance at each interpolation point of the prescribed contour trajectory.

A new issue thus arises, namely, how to define numerically the stiffness performance of a robotic machine along the prescribed trajectory which is used as the optimization objective for joint trajectories generation in the joint space. Since the system-wide stiffness model of a robotic machine is defined by a 6x6 stiffness matrix, it cannot be directly used as the optimization objective. In Pugazhenthi et al. [27], the sum of stiffness values in a constant direction along the prescribed trajectory is taken as the performance index for optimization, while in Clinton et al. [19], average stiffness values are used; both approaches avoid use of the stiffness matrix directly. However in the case of IWR, such

objectives from the entire prescribed trajectory are not applicable, because for every interpolation point of a prescribed trajectory in the end-effector of IWR, even when the location of the prescribed trajectory is fixed in the Cartesian workspace, the robot stiffness performance is still uncertain and depends on the pose configuration of the entire robot, which is shaped by the corresponding joints' position values and exists as infinite possible inverse solutions due to the existence of redundant kinematic DOF in the joint space; while in the work of Pugazhenthi et al. and Clinton et al., the stiffness performance at each interpolation point is fixed, once the location of the prescribed trajectory has been chosen. Thus, for the trajectory planning of IWR in the joint space, the overall stiffness performance at each interpolation point needs to be optimized. Consequently, the eigenvalue of the stiffness matrix is taken as the numerical optimization objective. The least eigenvalue of the six eigenvalues of the stiffness matrix represents the minimum stiffness performance in the direction of the eigenvector compared with the stiffness in an arbitrary direction [10][29]-[31]. Thus, if the least eigenvalues of the stiffness matrix of the end-effector at all the interpolation points of a prescribed trajectory have been maximized by searching all the possible joint space under the inverse kinematic constraint, it can be concluded that corresponding trajectories of joints of IWR have been generated that can yield the maximum stiffness performance for the prescribed trajectory of end-effector in the arbitrary direction.

Since the stiffness performance of the robotic machine depends on the pose of the robot in a highly nonlinear relationship, an optimization algorithm that is capable of searching for an optimum in a multi-dimensional variable space under multi-constraints is needed. In this work, a differential evolution (DE) algorithm is employed due to its global optimization ability and fast convergence property [32].

2.3 Vibration Suppression Method

Vibration suppression methods can be classified into two categories: passive control methods and active control methods [33]-[36]. Passive control methods mainly focus on the work of improving the structural properties of the target system, which is usually achieved by considering three different aspects: stiffening, damping and isolation. Stiffening refers to shifting the resonance frequency of the target system beyond the frequency band of the external disturbance, which is often realized by optimizing the structural design of the robotic machine, such as adopting a parallel structure rather than a serial structure, Damping refers to dissipating the vibration energy into another energy form so that it no longer appears in terms of macro-motions of the position of interest. Fluid damping, which transfers the kinetic energy of the target system into thermal energy of the damper fluid, is mostly adopted for such purposes. Isolation often means introducing an extra-subsystem, that allows relative motion, into the propagation path of

the external disturbance, thus preventing the disturbance from having an effect on the sensitive part of the target system.

Intrinsically, passive control methods can only attenuate the vibration phenomenon caused by the external disturbance, whereas active control methods are capable of suppressing the vibration [37]-[39]. Active control strategies can be divided into two approaches: feedback and feedforward. Feedback control can guarantee system stability, but it is only effective when the frequency of the disturbance is within the bandwidth of the control system. Moreover, feedback control is quite sensitive to phase lag. In feedforward control, an adaptive filter is often adopted, and the disturbance signal is then fed into the filter, which yields a secondary input signal for the target system. The filter coefficient is deemed to be adapted or well-tuned when the error signal of the target system is minimized at one or several points of interest. The principle behind this approach is that the secondary input signal acts on the target system as a counterbalance force that cancels out the effect of the external disturbance. One prominent advantage of such feedforward control is that it can work at any frequency. Furthermore, the control approach is less sensitive to phase lag. However, the performance of such adaptive filters is not global, which means that the filter is only effective on a specific disturbance at specific output points of interest.

Both passive and active control strategies are applied in the vibration suppression control of IWR. From the perspective of passive control, the stiffness optimized trajectory planning can be considered as applying a stiffening method of passive control; the Stewart platform of IWR is driven by hydraulics, which also provide a damping effect on external disturbances from the actuating limbs. Although both feedback and feedforward vibration suppression approaches are employed in the active vibration control strategies used in IWR, this dissertation only considers feedforward control.

An adaptive filter is not applied in the feedforward control discussed in this dissertation, since it cannot guarantee global performance in relation to the external disturbance; in the in-situ application, the IWR has to deal with a range of disturbances. Instead, an inverse dynamics model based feedforward control method is investigated and employed. The chatter vibration that occurs in the IWR during the machining process derives to a great extent from the inferior control performance of the actuators, which employ only PID based feedback control. Thus, in addition to the PID feedback control, an extra compensation force should be added to the actuators by a feedforward loop that can cancel out the effect of the external disturbance on the actuators. As a solution, the inverse dynamics model is the most attractive approach (equivalent position as the adapter filter) for such feedforward control since it can yield the same effective force as the external disturbance through the practical system on the actuators. Therefore, the issue to be solved is the question of how to build an accurate inverse dynamics model for the practical robotic machine. Since some sub-models for the components in the inverse

dynamics of a robotic machine are difficult to construct analytically, for example, friction models for different working conditions in the joints and internal valve leakage models for the hydraulic system, a feasible method for identification of the unknown components of the dynamics model must be investigated.

2.4 Dynamic Model Identification

Generally, dynamic model identification can be classified into two categories: parameter-based model identification and nonparametric model approximation [40]-[44]. In parameter-based model identification, the physical model or function of the dynamic system is known and the identification work focuses on parameter identification of the function using an input-output experimental data set of the target system [45]-[48]. For instance, in dynamics parameter identification for a serial robotic system, an inverse dynamics model that is linear with respect to the parameters being identified is often developed. The dynamics parameters can then be estimated by utilization of numerical optimization methods, such as weighted least squares estimation, Kalman filtering, maximum-likelihood estimation etc., based on the measured data of the inverse dynamics of the practical target system [42][49]. In the case of a parallel robot, although the inverse dynamics model is highly nonlinear with respect to the dynamic parameters, a simplified linear model can still be derived, albeit with a compromised accuracy [50]. In nonparametric model approximation, on the other hand, either no physical insight of the dynamic model is available for the target system or the modelling theory is still under development, and the identification work thus focuses on constructing a mapping model that can best approximate the input-outputs data set of the dynamic system over a domain of interest. Such a knowledge-lacking dynamic system is often deemed a 'black box', and artificial neural network (ANN) approaches are most frequently employed to approximate such black box systems due to their powerful data fitting ability [51]-[54].

- **Artificial neural network in the identification of 'black box'**

In the scientific literature, several ANN structures have been the subject of intensive research and some have been applied successfully in the 'black box' approximation of dynamic systems; for example, the multiplayer perceptron (MLP) neural network, the radial basis function neural network (RBFNN), and the functional link artificial network (ALANN) [55]-[57]. Generally, all these ANN structures are meant for approximating the target system as a whole entity, and a prior input-output data set of the target dynamical system must be measurable and have been obtained in advance. However, in practical applications of the above mentioned neural networks, when the interest domain of the target system covers a large area, and the target dynamic system contains many parameters and exhibits highly nonlinear and time variant behavior, neither the training process of the neural network is efficient, nor the accuracy of approximation of the target dynamic system satisfactory.

CHAPTER 2

In practice, comprehensive knowledge of most parts of the dynamics of a target system are available, and only small parts or subsystems of the dynamics are present as 'black boxes' or incomplete functions. Quite frequently, however, the small number of not-well-known parts of the dynamics are coupled with the dynamic formulation of the entire system and sometimes play a major role in the dynamics; thus, they cannot be ignored in the computation. For instance, if a parallel robot is moving in slow motion under heavy payload and the joints are not well lubricated, the effect of the friction force on the dynamics of the robot cannot be simply ignored. However, deriving individual friction models for such joints is not feasible in a parallel robot, since all the joints are coupled in the entire parallel kinematics and it is impossible to implement an input-output data measurement on an individual joint without inference from the dynamics of other joints.

- **Proposal of a BP neural network for identification of the unknown sub-models**

Currently, none of the ANN structures listed earlier can be applied directly to model or approximate unknown sub-models coupled in the entire dynamics, such as the friction model of a parallel robot, since direct training data for the neural network from the input-output of such sub-models is not measurable. In the dissertation, a dynamics modelling method is developed for dynamic systems containing linked unknown sub-models, in which the analytical modelling method for the dynamics of the entire system is employed based on the well-known knowledge of most parts of the dynamics, while the unknown sub-models are included as variables. A BP neural network is then employed to model the unknown sub-models of the dynamic system and the neural network yields the value for the variable in the constructed system-wide dynamics model. The input-output data of the entire dynamic system, which is utilized to train the BP neural network, is referred to as the indirect training data of the BP neural network. A modified Levenberg-Marquardt algorithm, which inherits both the speed advantage and convergence ability of the original Levenberg-Marquardt algorithm [58], is developed to train the BP neural network based on such indirect training data. The principle behind the approach is to derive a new Jacobian matrix between the errors of outputs of the entire dynamic system and the weights of the neural network. Consequently, a new weights updating rule for neural network training can be constructed that can utilize prior measured input-output data of the entire dynamic system. Once the errors between the outputs of the constructed model for the entire dynamic system and the outputs of the practical target system converge and approach to zero, the dynamics model for the entire system can be deemed to have been successfully constructed and the unknown sub-models in the system dynamics can be deemed as having been identified accurately over the domain of the training data.

CHAPTER 3

STIFFNESS BASED TRAJECTORY PLANNING

This chapter introduces stiffness-maximized trajectory planning for the serial-parallel kinematics redundant robotic machine, IWR. Since 4 redundant DOF exist in the joint space of IWR for a given location (consisting of position and orientation) of end-effector, the robotic machine permits an infinite number of inverse kinematic solutions in the joint space, which can form an infinite number of poses of robot and consequently yield infinite kinds of stiffness performance of the robotic machine. The trajectory planning refers to the trajectories generation in the robot's joint space at each interpolation point of the prescribed continuous trajectory in the Cartesian space of the end-effector. The generated trajectories of joints are constrained by the system-wide maximum stiffness performance of the robot and the inverse kinematics at each interpolation point. The maximum stiffness performance for a prescribed continuous trajectory of the end-effector in the Cartesian space implies that the system-wide stiffness performance of the robotic machine, which is represented by the least eigenvalue of the stiffness matrix, is maximized at every interpolation point of a continuous trajectory.

3.1 Introduction to Matrix Structural Analysis and **a** Variant of Virtual Joint Method

To develop the system-wide stiffness model of IWR, the MSA method [5] is applied to compute the stiffness matrix of the basic components of IWR, and a variant of the virtual joint method is used to compute the system-wide stiffness model, combined with the virtual work principle.

3.1.1 Matrix Structural Analysis

In MSA, a structure is defined as a combination of several basic beam elements and nodes. By applying the superposition principle, the stiffness matrix of the structure is obtained by assembling the stiffness matrices of the basic beam elements at the connected nodes in a specific order. In order to understand this method, the notions of nodal displacement, nodal force and the stiffness matrix of a single beam need to first be introduced.

A. Nodal displacement, nodal force and stiffness matrix of a single beam

In MSA, each basic beam element of a structure is defined by a number enclosed with a circle, while its two end nodes are indentified by two numbers. As shown in Fig.3, an arbitrary beam is represented by a circled number ①, while its two ends are represented by node i and node j, respectively.
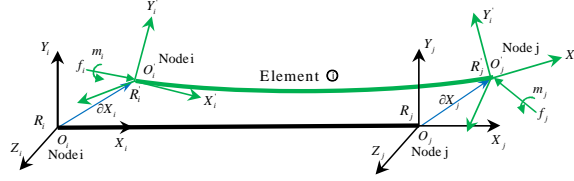
Fig.3 Single beam under external forces at both ends

In Fig 3, let two local reference frames, $R_i(X_i, Y_i, Z_i)$ and $R_j(X_j, Y_j, Z_j)$, be attached to the two nodes of the beam, while the beam is without any external force. Then, two external forces, $F_i = \begin{bmatrix} f_i^T & m_i^T \end{bmatrix}^T$ and $F_j = \begin{bmatrix} f_j^T & m_j^T \end{bmatrix}^T$ expressed in the frame R_i, are exerted on the two nodes respectively, which are defined as nodal forces. Consequently, elastic displacements occur on both nodes of the beam, and the original nodal locations are transferred to new points, which are represented by the new coordinates frames $R_i'(X_i', Y_i', Z_i')$ and $R_j'(X_j', Y_j', Z_j')$. At this point, the locations (consisting of position and orientation) of the new frames R_i' and R_j' with respect to the original frames R_i and R_j are defined as the nodal displacements, which are represented by $\partial X_i = [\Delta_i^T \quad \Theta_i^T]^T$ and $\partial X_j = [\Delta_j^T \quad \Theta_j^T]^T$ respectively, expressed in the frame R_i. Applying the equilibrium equation of mechanics of material yields Eq. (1) as follows:

$$\begin{bmatrix} F_i \\ F_j \end{bmatrix} = K_{ij} \begin{bmatrix} \partial X_i \\ \partial X_j \end{bmatrix}, \tag{1}$$

with

$$K_{ij} = \begin{bmatrix}
\frac{EA}{L} & 0 & 0 & 0 & 0 & 0 & \frac{-EA}{L} & 0 & 0 & 0 & 0 & 0 \\
0 & \frac{12EI_z}{L^3} & 0 & 0 & 0 & \frac{6EI_z}{L^2} & 0 & \frac{-12EI_z}{L^3} & 0 & 0 & 0 & \frac{6EI_z}{L^2} \\
0 & 0 & \frac{12EI_y}{L^3} & 0 & \frac{-6EI_y}{L^2} & 0 & 0 & 0 & \frac{-12EI_y}{L^3} & 0 & \frac{-6EI_y}{L^2} & 0 \\
0 & 0 & 0 & \frac{GI_p}{L} & 0 & 0 & 0 & 0 & 0 & \frac{-GI_p}{L} & 0 & 0 \\
0 & 0 & \frac{-6EI_y}{L^2} & 0 & \frac{4EI_y}{L} & 0 & 0 & 0 & \frac{6EI_y}{L^2} & 0 & \frac{2EI_y}{L} & 0 \\
0 & \frac{6EI_z}{L^2} & 0 & 0 & 0 & \frac{4EI_z}{L} & 0 & \frac{-6EI_z}{L^2} & 0 & 0 & 0 & \frac{2EI_z}{L} \\
\frac{-EA}{L} & 0 & 0 & 0 & 0 & 0 & \frac{EA}{L} & 0 & 0 & 0 & 0 & 0 \\
0 & \frac{-12EI_z}{L^3} & 0 & 0 & 0 & \frac{-6EI_z}{L^2} & 0 & \frac{12EI_z}{L^3} & 0 & 0 & 0 & \frac{-6EI_z}{L^2} \\
0 & 0 & \frac{-12EI_y}{L^3} & 0 & \frac{6EI_y}{L^2} & 0 & 0 & 0 & \frac{12EI_y}{L^3} & 0 & \frac{6EI_y}{L^2} & 0 \\
0 & 0 & 0 & \frac{-GI_p}{L} & 0 & 0 & 0 & 0 & 0 & \frac{GI_p}{L} & 0 & 0 \\
0 & 0 & \frac{-6EI_y}{L^2} & 0 & \frac{2EI_y}{L} & 0 & 0 & 0 & \frac{6EI_y}{L^2} & 0 & \frac{4EI_y}{L} & 0 \\
0 & \frac{6EI_z}{L^2} & 0 & 0 & 0 & \frac{2EI_z}{L} & 0 & \frac{-6EI_z}{L^2} & 0 & 0 & 0 & \frac{4EI_z}{L}
\end{bmatrix}.$$

In Eq. (1), K_{ij} stands for the stiffness matrix of a single beam with two nodes under external forces and is expressed in the reference frame R_i; E and G represent the Young's modulus and the shear modulus of the beam, respectively; I_y, I_z and I_p are the quadratic and polar moments; A is the cross-section area; and L is the length of the beam.

Writing the stiffness matrix in the four sub-matrices yields Eq. (2):

$$K_{ij} = \begin{bmatrix} K_{ii}^i & K_{ij}^i \\ K_{ji}^i & K_{jj}^i \end{bmatrix}_{12x12} ,$$

(2)

where the superscript i denotes the beam number, while the subscript i and j denote the node numbers respectively. The entries of sub-matrices can be generalized in terms of K_{xy}^i. Physically, the stiffness matrix K_{xy}^i in the entry of the sub-matrices stands for the load on the node x (referred to by the leading subscript x) while the node y (referred to by the following subscript y) undergoes a specific unit displacement. Therefore for a separated beam from a structure, the stiffness matrix K_{xy}^i can link the nodal force acting at nodal x to the nodal displacement at nodal y that is caused by the effect of the force from nodal x.

B. Stiffness matrix transformation

The stiffness matrix of a beam such as the K_{ij} in Eq. (2) is often expressed in a local reference frame of the beam, such as the local reference frame $R_i(X_i, Y_i, Z_i)$. However, in application of MSA, all the stiffness matrices for the composing beams of a structure have to be expressed in a global reference frame for the algebraic operation. Thus, the stiffness matrix has to be transformed from the local reference frame to the global reference frame. If the frame R_o is a global reference frame, and the 3x3 rotation matrix ^oR_i stands for the rotation matrix from the global reference frame R_o to the local reference frame R_i, then, the stiffness matrix K_{ij} expressed in the global reference frame R_o can be obtained by Eq. (3) as follows:

$$^oK_{ij} = TK_{ij}T^{-1}$$

(3)

with $T = \begin{bmatrix} ^oR_i & 0_3 & 0_3 & 0_3 \\ 0_3 & ^oR_i & 0_3 & 0_3 \\ 0_3 & 0_3 & ^oR_i & 0_3 \\ 0_3 & 0_3 & 0_3 & ^oR_i \end{bmatrix}$, where 0_3 stands for the 3x3 zero matrix.

C. Stiffness matrix of a structure by MSA

Fig.4 shows a structure fixed in the ground and composed of two beams, ① and ②. Two local reference frames R_o and R_1 are attached to the nodes 0 and 1 respectively.
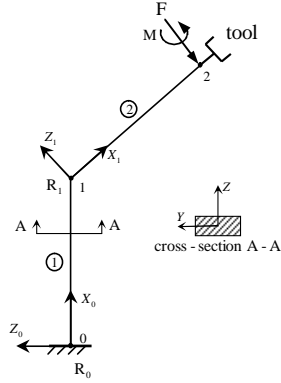
Fig. 4 Structure composed of two beams

The stiffness matrix of this structure can be obtained as Eq. (4) by applying the superposition principle of MSA:

$$^0K = \begin{bmatrix} ^0K_{11}^1 + ^0K_{11}^2 & ^0K_{11}^2 \\ ^0K_{21}^2 & ^0K_{22}^2 \end{bmatrix},$$ (4)

where the leading superscript 0 denotes in which reference frame the stiffness matrix is expressed. The composing entries of ^0K can be generalized in terms of $^0K_{xy}^i$, which is obtained by the stiffness matrix transformation from the local reference frame to the global reference frame as shown in Eq. (5):

$$^0K_{xy}^i = \begin{bmatrix} ^0R_i & 0_3 \\ 0_3 & ^0R_i \end{bmatrix} K_{xy}^i \begin{bmatrix} ^0R_i & 0_3 \\ 0_3 & ^0R_i \end{bmatrix}^{-1},$$ (5)

where K_{xy}^i stands for the nodal stiffness matrix in the local reference frame, which is computed from the corresponding entry of stiffness matrix in Eq. (2).

Based on Eq. (4), a numerical result of the stiffness matrix for this two-beam structure can be computed, shown in Table 2, on the basis of the geometrical and mechanical parameters of the structure, summarized in Table 1.

Table.1 Geometrical and mechanical parameters

Geometrical Parameters		Mechanical Parameters	
Length (mm)	Cross-section Area (mm^2)	Young's Modulus (GPa)	Shear Modulus (GPa)
49	45x18	210	80
41	45x18		

Table.2 Numerical results of the stiffness matrix of the structure illustrated in Fig.4

9.751958551684694e8	0	-3.087681914430521e8	0	1.080121556617323e7	0
0	4.788952285024700e8	0	-1.349618697221210e7	0	-1.528232314069286e7
-3.087681914430518e8	0	1.951195464684377e8	0	5.833636585134454e4	0
0	-1.349618697221211e7	0	4.610798663224975e5	0	4.715075609541764e5
1.080121556617323e7	0	5.833636585134082e4	0	2.949294709930832e5	0
0	-1.528232314069288e7	0	4.715075609541766e5	0	6.659904969667222e5

Stiffness calculation of a simple beam structure by applying MSA is quite accurate with a high calculation efficiency [68]. However, for complicated structures, especially structures with many joints in its kinematics, the VJM method is often used to build up its system-wide stiffness model.

3.1.2 Variant of Virtual Joint Method

A. Gosselin's lumped model

The virtual joint method, which is also called the lumped modelling method, was proposed by Gosselin in 2000 [20] to compute the stiffness of a parallel robot. In the lumped model, the flexibility of the beam is replaced by a virtual spring joint, and the beam is regarded as rigid, given that under the same external load, the virtual spring joint produces the same tip translational deflection via the rigid beam as with the flexible beam.
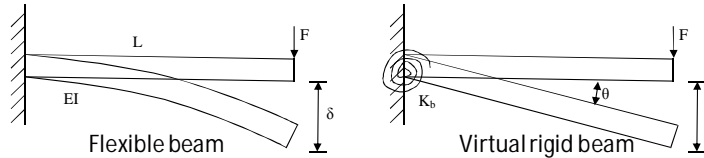
Fig.5 Lumped model of a flexible beam

Fig. 5 shows the lumped model of a flexible beam under external load. With a force applied on the tip of the beam, a resultant translational deformation is obtained by Eq. (6) as follows:

$$\delta = \frac{FL^3}{3EI},$$ (6)

where L stands for the length of the beam; E is the Young's modulus; and I is the moment of inertia of the cross-sectional area. Since the virtual spring joint yields the same tip deflection, the equivalent rotational deflection in the virtual joint is obtained by Eq. (7):

$$\theta = \frac{\delta}{L} = \frac{FL^2}{3EI} . \tag{7}$$

Thus, the stiffness of the virtual spring joint is expressed as in Eq. (8):

$$K_b = \frac{FL}{\theta} = \frac{3EI}{L} . \tag{8}$$

The lumped stiffness of a beam that is under a twist can be obtained analogously.

When using the lumped modelling method, a Denavit-Hartenberg (DH) geometric model is often employed for the kinematics description of the robot, and thus a stiffness model can be obtained by accounting for the links deformations of the robot through integration into the flexibilities of the virtual joints represented by the DH parameters.

However, the lumped model will lead to a different orientation deflection at the tip of the link. Moreover, the lumped model only accounts for the links deformation along the directions of the DH joints, whereas in practice a deformation could occur in any direction of a link. Since the geometric structure of the robot studied in the dissertation is large and complicated, and there is no comparable research result available on how these errors of orientation deflection and the limited deflection directions of the DH model applied by the lumped model affect the accuracy of stiffness modelling, the lumped model is not applied in the dissertation. However, the virtual joint concept is nevertheless valuable and has been adopted for the stiffness modelling of IWR, albeit with modification. As a result, a new stiffness modelling method is developed in the dissertation, which is a variant of the virtual joint method and employs the virtual work principle.

B. Variant of virtual joint method

In the variant of the virtual joint method presented in this work, the virtual joint is attached to the end-tip of the link, rather than the start tip of the link as in the lumped model. Such a virtual joint accounts for deflections of both translation and orientation at the tip of the link. If a flexible link undergoes a deformation in which the end tip of the flexible link travels a translation displacement and an orientation displacement, a virtual joint with '2 DOF' can be applied to the end tip of the link, given that the link is regarded as rigid. The concept of '2 DOF' in this case means the translation and orientation motions, which can cover 6 DOF adaptively for the specific application. Then, the actual deformations taking place at the tip of the link can be considered as being accomplished by the translation and orientation motions of such a '2 DOF' virtual joint. Fig. 6 shows a decomposed deformation process of a two-beam structure with such integrated virtual joints while the structure is under external forces.
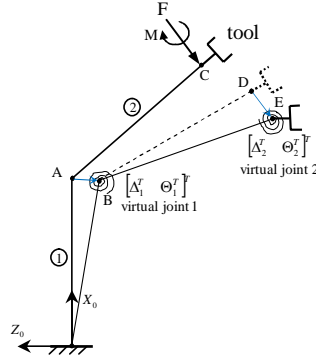
Fig.6 Variant of the virtual joint method

The continuous deformation process of the structure can be regarded as being accomplished by the deformations of the two links sequentially. When the forces $\begin{bmatrix} F^T & M^T \end{bmatrix}^T$ are exerted on point C of the structure, it is assumed that only the deformation of link 1 takes place while the deformation of link 2 is assumed to be zero. Such deformation of link 1 consists of a tip translation from point A to B and a tip rotation at point B. By introducing a 2 DOF virtual joint in the end-tip of link 1, the deformation can be deemed to be accomplished by the translational and rotational motions of this virtual joint, which can be represented as $\begin{bmatrix} \Delta_1^T & \Theta_1^T \end{bmatrix}^T$ if the link is regarded as rigid. At this moment, point C of the structure travels to the D position, as shown in Fig. 6. Then, link 2 can be considered to be undergoing a deformation while link 1 and its virtual joint stay still. By analogy, the deformation that takes place in link 2, which is represented as $\begin{bmatrix} \Delta_2^T & \Theta_2^T \end{bmatrix}^T$, can also be deemed to be accomplished by a virtual joint introduced in the end-tip of link 2. At this moment, the deformation of the whole structure is deemed to have finished, and point C of the structure to have arrived at position E while the tool attached to the tip of the structure undergoes an orientation displacement. The above sequential deformation process can be described by Eq. (9) as follows:

$$\begin{cases} \Delta = \Delta_2 + \Theta_1 \times r_2 + \Delta_1 \\ \quad \Theta = \Theta_2 + \Theta_1 \end{cases}, \tag{9}$$

where Δ and Θ stand for the system-wide translational and orientation displacements taking place at point C of the structure; and r_2 is the length of link 2.

Writing Eq. (9) in matrix form, we obtain:

$$\begin{bmatrix} \Delta \\ \Theta \end{bmatrix} = \begin{bmatrix} I_{3\times 3} & -r_2 \times & I_{3\times 3} & O_{3\times 3} \\ O_{3\times 3} & I_{3\times 3} & O_{3\times 3} & I_{3\times 3} \end{bmatrix} \begin{bmatrix} \Delta_1 \\ \Theta_1 \\ \Delta_2 \\ \Theta_2 \end{bmatrix}, \tag{10}$$

39

or simply:

$$\begin{bmatrix} \Delta \\ \Theta \end{bmatrix} = J \begin{bmatrix} \Delta_1 \\ \Theta_1 \\ \Delta_2 \\ \Theta_2 \end{bmatrix}, \tag{11}$$

where J denotes the Jacobian matrix between the system-wide deformations of the end-tips in the structure and the local deformations in the connecting nodes of the links. In Eq. (10), $r_2 \times$ represents the skew matrix of vector r_2.

Let K_1 denote the stiffness of the virtual joint 1 and K_2 denote the stiffness of the virtual joint 2; $\begin{bmatrix} \delta\Delta_1^T & \delta\Theta_1^T & \delta\Delta_2^T & \delta\Theta_2^T \end{bmatrix}^T$ the virtual displacements at the virtual joints after the links' deformation; and $\begin{bmatrix} \delta\Delta^T & \delta\Theta^T \end{bmatrix}^T$ the virtual system-wide displacements at the end-tip of the structure after the system-wide deformation. Applying the virtual work principle then yields:

$$\begin{bmatrix} \delta\Delta^T & \delta\Theta^T \end{bmatrix} \begin{bmatrix} F \\ M \end{bmatrix} = \begin{bmatrix} \delta\Delta_1 & \delta\Theta_1 & \delta\Delta_2 & \delta\Theta_2 \end{bmatrix} \begin{bmatrix} K_1 & 0_6 \\ 0_6 & K_2 \end{bmatrix} \begin{bmatrix} \Delta_1 \\ \Theta_1 \\ \Delta_2 \\ \Theta_2 \end{bmatrix}, \tag{12}$$

where K_1 and K_2 can be computed according to the entry of K_{ii}^i in Eq. (2) with the stiffness matrix transformation; and 0_6 denotes a 6x6 zero matrix.

Applying Eq. (11) in the vector $\begin{bmatrix} \delta\Delta^T & \delta\Theta^T \end{bmatrix}$ of Eq. (12) yields:

$$\begin{bmatrix} \delta\Delta_1^T & \delta\Theta_1^T & \delta\Delta_2^T & \delta\Theta_2^T \end{bmatrix} J^T \begin{bmatrix} F \\ M \end{bmatrix} = \begin{bmatrix} \delta\Delta_1^T & \delta\Theta_1^T & \delta\Delta_2^T & \delta\Theta_2^T \end{bmatrix} \begin{bmatrix} K_1 & 0_6 \\ 0_6 & K_2 \end{bmatrix} \begin{bmatrix} \Delta_1 \\ \Theta_1 \\ \Delta_2 \\ \Theta_2 \end{bmatrix}. \tag{13}$$

Since the vectors $\delta\Delta_1$, $\delta\Theta_1$, $\delta\Delta_2$ and $\delta\Theta_2$ are linearly independent, Eq. (13) can be simplified as:

$$J^T \begin{bmatrix} F \\ M \end{bmatrix} = \begin{bmatrix} K_1 & 0_6 \\ 0_6 & K_2 \end{bmatrix} \begin{bmatrix} \Delta_1 \\ \Theta_1 \\ \Delta_2 \\ \Theta_2 \end{bmatrix}, \tag{14}$$

or:

$$J \begin{bmatrix} K_1^{-1} & 0_6 \\ 0_6 & K_2^{-1} \end{bmatrix} J^T \begin{bmatrix} F \\ M \end{bmatrix} = \begin{bmatrix} \Delta \\ \Theta \end{bmatrix}. \tag{15}$$

Thus, the system-wide compliance and stiffness matrices of the structure become:

$$C = J \begin{bmatrix} K_1^{-1} & 0_6 \\ 0_6 & K_2^{-1} \end{bmatrix} J^T , \tag{16}$$

$$K = C^{-1} = \left(J \begin{bmatrix} K_1^{-1} & 0_6 \\ 0_6 & K_2^{-1} \end{bmatrix} J^T \right)^{-1} . \tag{17}$$

C. Results comparison between MSA and the variant of the virtual joint method

Applying the variant of the virtual joint method developed above on the structure in Fig.4, the numerical results of the system-wide stiffness matrix given in Table 3 are obtained.

Table.3 Numerical results of the stiffness matrix obtained by the variant of the VJM

9.751958551684697e8	0	-3.087681914430522e8	0	1.080121556617323e7	0
0	4.788952285024690e8	0	-1.349618697221207e7	0	-1.528232314069283e7
-3.087681914430522e8	0	1.951195464684374e8	0	5.833636585133802e4	0
0	-1.349618697221207e7	0	4.610798663224979e5	0	4.715075609541766e5
1.080121556617323e7	0	5.833636585133802e4	0	2.949294709930830e5	0
0	-1.528232314069283e7	0	4.715075609541766e5	0	6.659904969667220e5

A comparison of the results from the MSA method and the variant of the VJM is given in Table 4.

Table.4 Comparison of the numerical results for the stiffness matrix when using MSA and the variant of the VJM on the same structure

1e-7 x					
2.384	0	1.192	0	0.019	0
0	10.133	0	0.279	0	0.279
3.586	0	2.384	0	0.065	0
0	0.354	0	0.004	0	0.002
0	0.038	0	0.002	0	0
0	0.428	0	0	0	0.002

From Table 4, it can be seen that the numerical results computed by the variant of the virtual joint method are almost the same as the results computed by the MSA method, which in some sense provides mutual validation of the two approaches.

The MSA method is especially suitable for stiffness analysis of large truss and beam structures in civil engineering, in which the structural configuration is relatively stable due to the absence of active joints. However, in robotic applications, active joints are inevitably employed, which render the kinematics configuration of the robot variable and complicated. When the MSA method is applied in such situations for system-wide

stiffness evaluation, error of around 9% is found in the stiffness calculation [19]. However, the VJM variant can deal with such kinematics with active joints, since the virtual joint is necessarily assumed to be an active joint that produces the equivalent displacement as the deformation.

The following section will introduce system-wide stiffness modelling of the hybrid robot IWR based on the variant of the virtual joint method when the stiffness matrix of the basic components are computed by the MSA method.

3.2 Stiffness Modelling of **a** Hybrid Robot

Fig 7 shows a 3D model and schematic representation of the IWR. Prior to the stiffness modelling process, the coordinates system needs to be established, as shown in Fig 7 and 8.
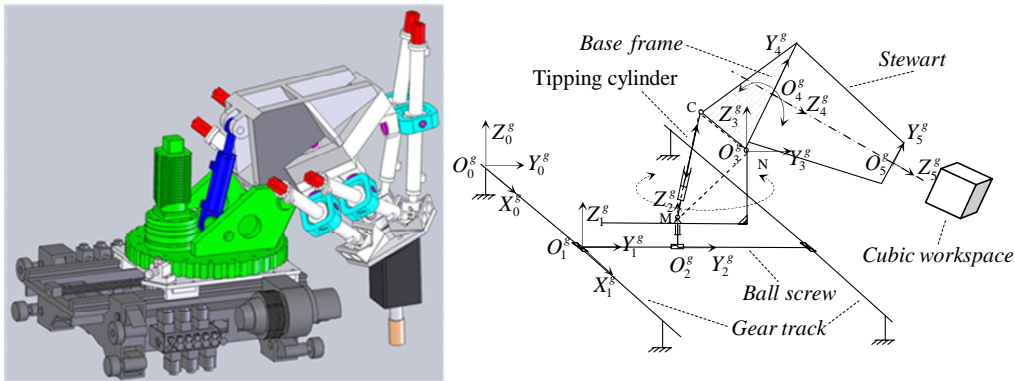
Fig.7 3D model of IWR and its schematic representation
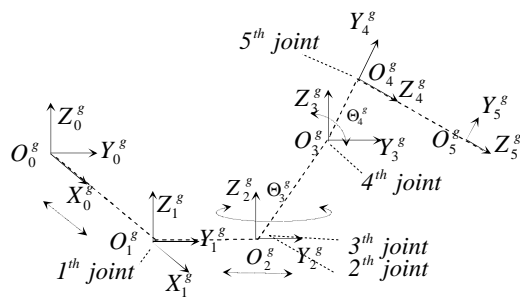
Fig.8 Kinematic chain of IWR

42

The coordinate system $X_0^g Y_0^g Z_0^g$ is attached to the track as the global reference frame with its z-axis vertical to the track plane and x-axis pointing in the track direction. $X_1^g Y_1^g Z_1^g$ is attached to the tip of the ball screw with its x-axis pointing in the track direction and y-axis pointing in the ball screw direction. $X_2^g Y_2^g Z_2^g$ is attached to the nut of the ball screw. $X_3^g Y_3^g Z_3^g$ is attached to the top joint of the rotating table with its origin located at the joint pivot and its x-axis pointing in the pivot axis direction. $X_4^g Y_4^g Z_4^g$ is attached to the base of the Stewart structure with its origin located at the centre of the base. $X_5^g Y_5^g Z_5^g$ is attached to the end-effector as the tool frame.

The stiffness modelling process of IWR can be divided into two steps: first the stiffness model for the Stewart structure is constructed by accounting for the flexibilities of the driving limbs and the feet of the Stewart structure; then the entire Stewart structure is regarded as a virtual flexible link. The robot as a whole entity can thus be considered a serial structure, for which the system-wide stiffness model is obtained by applying the VJM variant and the virtual work principle.

3.2.1 Stiffness modelling of **a** parallel robot

A. Stiffness modelling of the base of a Stewart structure

Fig. 9 shows a 3D model of the base of the Stewart structure.
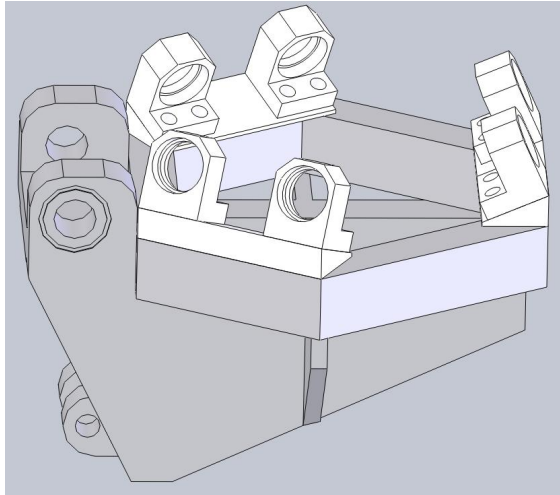
Fig.9 3D model of the base of the Stewart structure (inverted compared with Fig.7)

The base of the Stewart structure consists of a bearing house and a U-shape joint, as shown in Fig.10.

(i) Bearing house   (ii) U-shape joint   (iii) Base of the Stewart structure
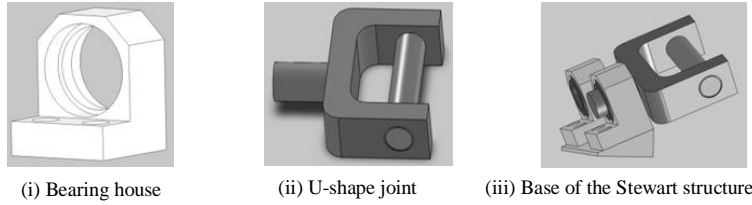
Fig.10 Stewart base structure: (i) bearing house, (ii) U-shape joint (iii) base of the Stewart structure

In order to build up the stiffness model for the base of the Stewart structure, the MSA method needs to be first applied to compute the stiffness matrix of the basic components of the structure – the bearing house and the U-shape joint.

When applying the MSA method, the bearing house, U-shape joint and composite base of the Stewart structure are simplified into frame structures. Fig.11 shows a schematic diagram of the simplified frame structures.

(i) Bearing house   (ii) U shape joint   (iii) Base of Stewart
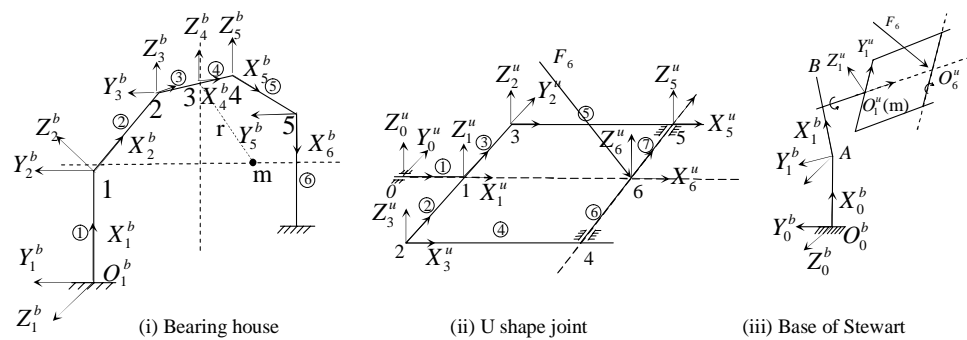
Fig.11 Schematic diagram of frame structures: (i) bearing house, (ii) U-shape joint and (iii) base composed of a bearing house and U-shape joint

- **Stiffness modelling of bearing house**

The bearing house is simplified into an arc structure composed of 6 basic straight elements, which are denoted by the circled numbers and connected by 5 nodes, as shown in Fig.11 (i). $X_i^b Y_i^b Z_i^b$ are the local reference frames with $i = 1, 2, ..., 5$, of which $X_1^b Y_1^b Z_1^b$ is chosen as the global reference frame for the stiffness computation of the bearing house.

Applying the MSA on the bearing house yields Eq. (18) :

$$\begin{bmatrix} {}^{b}F_1 \\ {}^{b}F_2 \\ {}^{b}F_3 \\ {}^{b}F_4 \\ {}^{b}F_5 \end{bmatrix} = \begin{bmatrix} {}^{b}K_{11}^{1}+{}^{b}K_{11}^{2} & {}^{b}K_{12}^{2} & O_{6\times6} & O_{6\times6} & O_{6\times6} \\ {}^{b}K_{21}^{2} & {}^{b}K_{22}^{2}+{}^{b}K_{22}^{3} & {}^{b}K_{23}^{3} & O_{6\times6} & O_{6\times6} \\ O_{6\times6} & K_{32}^{3} & {}^{b}K_{33}^{3}+{}^{b}K_{33}^{4} & {}^{b}K_{34}^{4} & O_{6\times6} \\ O_{6\times6} & O_{6\times6} & {}^{b}K_{43}^{4} & {}^{b}K_{44}^{4}+{}^{b}K_{44}^{5} & {}^{b}K_{45}^{5} \\ O_{6\times6} & O_{6\times6} & O_{6\times6} & K_{54}^{5} & {}^{b}K_{55}^{5}+{}^{b}K_{55}^{6} \end{bmatrix} \begin{bmatrix} {}^{b}\Delta_1 \\ {}^{b}\Delta_2 \\ {}^{b}\Delta_3 \\ {}^{b}\Delta_4 \\ {}^{b}\Delta_5 \end{bmatrix}, \quad (18)$$

and exchanging the positions of line 3 with line 5 obtains:

$$\begin{bmatrix} {}^{b}F_1 \\ {}^{b}F_2 \\ {}^{b}F_5 \\ {}^{b}F_4 \\ {}^{b}F_3 \end{bmatrix} = \begin{bmatrix} {}^{b}K_{11}^{1}+{}^{b}K_{11}^{2} & {}^{b}K_{12}^{2} & O_{6\times6} & O_{6\times6} & O_{6\times6} \\ {}^{b}K_{21}^{2} & {}^{b}K_{22}^{2}+{}^{b}K_{22}^{3} & O_{6\times6} & O_{6\times6} & {}^{b}K_{23}^{3} \\ O_{6\times6} & O_{6\times6} & {}^{b}K_{55}^{5}+{}^{b}K_{55}^{6} & K_{54}^{5} & O_{6\times6} \\ O_{6\times6} & O_{6\times6} & {}^{b}K_{45}^{5} & {}^{b}K_{44}^{4}+{}^{b}K_{44}^{5} & {}^{b}K_{43}^{4} \\ O_{6\times6} & K_{32}^{3} & O_{6\times6} & {}^{b}K_{34}^{4} & {}^{b}K_{33}^{3}+{}^{b}K_{33}^{4} \end{bmatrix} \begin{bmatrix} {}^{b}\Delta_1 \\ {}^{b}\Delta_2 \\ {}^{b}\Delta_5 \\ {}^{b}\Delta_4 \\ {}^{b}\Delta_3 \end{bmatrix}, \quad (19)$$

where the leading superscript b denotes that all the vectors are expressed in the global reference frame $X_1^{b}Y_1^{b}Z_1^{b}$; Vector ${}^{b}F_i$ denotes the postulated external forces acting on the nodes i, and ${}^{b}\Delta_i$ denotes the corresponding resultant deformations of node i, here $i = 1$, 2, ..., 5; The entries of the stiffness matrix in Eq. (19) can be generalized in terms of ${}^{b}K_{xy}^{j}$ with $j = 1, 2, ..., 6$ and $x, y = 1, 2, ..., 5$, which can be computed according to the entries in Eq. (2) and expressed in the global reference frame $X_1^{b}Y_1^{b}Z_1^{b}$ by applying the stiffness matrix transformation technique.

Partitioning Eq. (19) according to the dashed lines gives:

$$\begin{bmatrix} {}^{b}T \\ {}^{b}F_3 \end{bmatrix} = \begin{bmatrix} {}^{b}K_{11} & {}^{b}K_{12} \\ {}^{b}K_{21} & {}^{b}K_{22} \end{bmatrix} \begin{bmatrix} {}^{b}\Delta \\ {}^{b}\Delta_3 \end{bmatrix}, \quad (20)$$

where ${}^{b}T$ stands for $\begin{bmatrix} {}^{b}F_1^{T} & {}^{b}F_2^{T} & {}^{b}F_5^{T} & {}^{b}F_4^{T} \end{bmatrix}^{T}$; ${}^{b}\Delta$ stands for $\begin{bmatrix} {}^{b}\Delta_1^{T} & {}^{b}\Delta_2^{T} & {}^{b}\Delta_5^{T} & {}^{b}\Delta_4^{T} \end{bmatrix}^{T}$; and the entry -- ${}^{b}K_{xy}$ with $x = 1, 2$ and $y = 1, 2$ -- in the stiffness matrix of Eq. (20) stands for the corresponding block partitioned in the stiffness matrix of Eq. (19).

If it is assumed that the forces acting on the bearing house from the shaft of the U-shape joint mainly focus on node 3 and the deformations of the bearing house are mainly contributed by node 3, thus ${}^{b}T$ equals to zero vectors. Utilizing a static condensation technique (Guyan Reduction) on Eq. (20) gives:

$$ {}^{b}F_3 = ({}^{b}K_{22} - {}^{b}K_{21}\,{}^{b}K_{11}^{-1}\,{}^{b}K_{12})\,{}^{b}\Delta_3. \quad (21)$$

Thus, the stiffness matrix of the bearing house in node 3 is obtained as follows:

$$ {}^{b}K_3 = {}^{b}K_{22} - {}^{b}K_{21}\,{}^{b}K_{11}^{-1}\,{}^{b}K_{12}. \quad (22)$$

In practice, the shaft of the U-shape joint is assembled into the bearing house and can be regarded as rigid due to its compact size. If, after the assembly, node 1 of the U-shape joint (Fig.11.(ii)) is made coincident with a virtual position m in the bearing house (Fig.11.(i)), the deformations taking place at node 3 of the bearing house will transfer to position m, which consequently causes a displacement in node 1 of the U-shape joint.

Applying the VJM variant from node 3 of the bearing house to the virtual point m yields:

$$^{b}K_{m} = (J_{m}{}^{b}K_{3}^{-1}J_{m}^{T})^{-1},\qquad(23)$$

where $^{b}K_{m}$ stands for the stiffness matrix of the bearing house at the virtual position m; and J stands for the Jacobian matrix, which can be obtained as Eq. (24):

$$J_{m} = \begin{bmatrix} I_{3x3} & -r\times \\ O_{3x3} & I_{3x3} \end{bmatrix},\qquad(24)$$

where I_{3x3} stands for the 3x3 identity matrix; O_{3x3} is the 3x3 zero matrix; r is the vector from node 3 of the bearing house to the virtual position m; and $r\times$ represents the skew matrix of vector r.

In practice, the load from the U-shape joint acting on the virtual position m only consists of 4 forces, that is, forces f_{y} and f_{z} presented in the Y_{1} and Z_{1} directions of the global reference frame $X_{1}^{b}Y_{1}^{b}Z_{1}^{b}$, and the torques m_{x} and m_{z} presented around the X_{1} and Z_{1} directions. Utilizing the static condensation technique on the deformation equilibrium equation of the virtual position m gives:

$$\begin{bmatrix} ^{b}f_{y} & ^{b}f_{z} & ^{b}m_{x} & ^{b}m_{z} \end{bmatrix}^{T} = {}^{b}k_{m}\begin{bmatrix} ^{b}\delta_{y} & ^{b}\delta_{z} & ^{b}\theta_{x} & ^{b}\theta_{z} \end{bmatrix}^{T},\qquad(25)$$

where $^{b}k_{m}$ stands for the 4x4 stiffness matrix of the virtual position m in the bearing house under the practical load from the U-shape joint; and the leading superscript b denotes the vectors that are expressed in the global reference frame $X_{1}^{b}Y_{1}^{b}Z_{1}^{b}$.

Table. 5 shows the numerical results of the stiffness matrix of the virtual position m in the bearing house expressed in the global reference frame $X_{1}^{b}Y_{1}^{b}Z_{1}^{b}$.

Table.5 Numerical results of the stiffness matrix of the virtual position M of the bearing house

1e5 x			
3718.85	0	0	-66.96
0	2914.30	0	0
0	0	8.37	0
-66.96	0	0	3.28

- **Stiffness modelling of a U-shape joint**

Utilizing the same technique – MSA and the static condensation technique – on the U-shape joint, the deformation equilibrium equation of node 6 in the U-shape can be obtained and expressed in the local reference frame $X_1^u Y_1^u Z_1^u$ as follows:

$$^u F_6 = (^u K_{22} - ^u K_{21}\,^u K_{11}^{-1}\,^u K_{12})\,^u \Delta_6 , \qquad (26)$$

or simply:

$$^u F_6 = ^u K_6\,^u \Delta_6 , \qquad (27)$$

where the leading superscript u denotes that the vectors are expressed in the reference frame $X_1^u Y_1^u Z_1^u$, which is taken as the global reference frame of the U-shape joint; $^u F_6$ stands for the external load acting on node 6 of the U-shape joint; $^u \Delta_6$ stands for the corresponding deformations; and the items -- $^u K_{xy}$ with $x = 1, 2$ and $y = 1, 2$ -- stand for the partitioned blocks of the stiffness matrix, which are obtained by applying the MSA on the U-shape joint as follows:

$$
\begin{bmatrix} ^u F_1 \\ ^u F_2 \\ ^u F_3 \\ ^u F_4 \\ ^u F_5 \\ ^u F_6 \end{bmatrix}
=
\begin{bmatrix}
^u K_{11}^2 + ^u K_{11}^3 & ^u K_{12}^2 & ^u K_{13}^3 & 0_{6x6} & 0_{6x6} & 0_{6x6} \\
^u K_{21}^2 & ^u K_{22}^2 + ^u K_{22}^4 & 0_{6x6} & ^u K_{24}^4 & 0_{6x6} & 0_{6x6} \\
^u K_{31}^3 & 0_{6x6} & ^u K_{33}^3 + ^u K_{33}^5 & 0_{6x6} & ^u K_{35}^5 & 0_{6x6} \\
0_{6x6} & ^u K_{42}^2 & 0_{6x6} & ^u K_{44}^4 + ^u K_{44}^6 & 0_{6x6} & ^u K_{46}^6 \\
0_{6x6} & 0_{6x6} & ^u K_{53}^5 & 0_{6x6} & ^u K_{55}^5 + ^u K_{55}^7 & ^u K_{56}^7 \\
0_{6x6} & 0_{6x6} & 0_{6x6} & ^u K_{64}^6 & ^u K_{65}^7 & ^u K_{66}^6 + ^u K_{66}^7
\end{bmatrix}
\begin{bmatrix} ^u \Delta_1 \\ ^u \Delta_2 \\ ^u \Delta_3 \\ ^u \Delta_4 \\ ^u \Delta_5 \\ ^u \Delta_6 \end{bmatrix} . \qquad (28)
$$

In practice, the forces acting on node 6 of the U-shape joint are constrained along the X_6^u and Z_6^u axes of the local frame $X_6^u Y_6^u Z_6^u$ (Fig. 11(ii)) due to the existence of two rotational DOF in the U-shape joint. Thus, the deformation equilibrium equation on node 6 represented by Eq. (27) can be simplified further, as shown in Eq. (29), by employing the static condensation technique:

$$\begin{bmatrix} ^u f_x & ^u f_z \end{bmatrix}^T = ^u k_6 \begin{bmatrix} ^u \delta_x & ^u \delta_z \end{bmatrix}^T , \qquad (29)$$

where $^u k_6$ stands for the 2x2 stiffness matrix of node 6 in the U-joint expressed in the reference frame $X_1^u Y_1^u Z_1^u$; $\begin{bmatrix} ^u f_x & ^u f_z \end{bmatrix}^T$ stands for the practical force acting on node 6; and $\begin{bmatrix} ^u \delta_x & ^u \delta_z \end{bmatrix}^T$ stands for the corresponding deformations.

Table 6 shows the numerical results of the stiffness matrix of node 6 in the U-shape joint expressed in the reference frame $X_1^u Y_1^u Z_1^u$.

Table.6 Numerical results of the stiffness matrix of node 6 in the U-shape joint

1e8 x	
2.50	0
0	1.39

- **Stiffness modelling of a base structure composed of a bearing house and U-shape joint**

Since the base structure is composed of a bearing house and U-shape joint, a kinematic chain can be formed by introducing the virtual joints into the virtual position m in the bearing house and node 6 of the U-shape joint.

Fig. 12 shows the kinematic chain in the base structure of the Stewart platform, which starts from the origin of Stewart base reference frame $X_4^g Y_4^g Z_4^g$, passes through the origin of reference frame $X_1^b Y_1^b Z_1^b$ and virtual position m in the bearing house, and finally ends at node 6 of the U-shape joint.
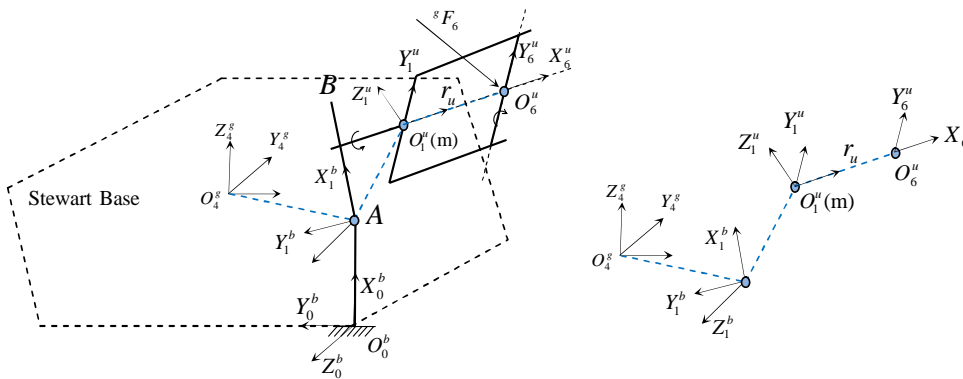
Fig.12 Kinematic chain in the base structure of the Stewart platform

In the kinematic chain, the deformations of the virtual position m in the bearing house and the deformations of node 6 in the U-shape joint can be assumed to be caused by the motions of the corresponding virtual joints, thus the system-wide deformations of the base can be described by Eq. (30) as follows:

$$^{g4}\Delta_{ft} = {}^{g4}\Delta_6 + {}^{g4}\Theta_m \times {}^{g4}r_u + {}^{g4}\Delta_m,$$ (30)

where the leading superscript g4 denotes that the vectors in the equation are expressed in the reference frame $X_4^g Y_4^g Z_4^g$ of the base of the Stewart structure; $^{g4}\Delta_{ft}$ stands for the system-wide translational deformations taking place at node 6 of the U-shape joint; $^{g4}\Delta_6$ stands for the local translational deformations of node 6 of the U-shape joint; $^{g4}\Delta_m$ and $^{g4}\Theta_m$ stand for the local translation and orientation deformations at the virtual position m of the bearing house; and $^{g4}r_u$ stands for the length vector from the virtual position m of the bearing house to node 6 of the U-shape joint.

Writing Eq. (30) in matrix form gives:

$$^{g4}\Delta_{ft} = \begin{bmatrix} I_{3x3} & I_{3x3} & -^{g4}r_u \times \end{bmatrix} \begin{bmatrix} ^{g4}\Delta_6 \\ ^{g4}\Delta_m \\ ^{g4}\Theta_m \end{bmatrix}, \tag{31}$$

or simply:

$$^{g4}\Delta_{ft} = J_{ft} \begin{bmatrix} ^{g4}\Delta_6 \\ ^{g4}\Delta_m \\ ^{g4}\Theta_m \end{bmatrix}, \tag{32}$$

where J_{ft} denotes the Jacobian matrix between the system-wide deformations of node 6 and the motions of the virtual joints. In Eq. (31) $^{g4}r_u \times$ represents the skew matrix of $^{g4}r_u$.

Let $^{g4}K_m$ and $^{g4}K_6$ denote the local stiffness matrices at the virtual position m of the bearing house and node 6 of the U-shape respectively, which are both expressed in the Stewart platform frame $X_4^g Y_4^g Z_4^g$ and obtained by applying the stiffness matrix transformation technique on $^b k_m$ of Eq.(25) and $^u k_6$ of Eq.(29) correspondingly. And let $\delta^{g4}\Delta_{ft}$, $\delta^{g4}\Delta_6$, $\delta^{g4}\Delta_m$ and $\delta^{g4}\Theta_m$ denote the virtual displacement based on the current deformations; then, applying the virtual work principle in the kinematic chain of deformations yields:

$$\begin{bmatrix} \delta^{g4}\Delta_{ft}^{T} \end{bmatrix} \begin{bmatrix} ^{g4}F_6 \end{bmatrix} = \begin{bmatrix} \delta^{g4}\Delta_6^{T} & \delta^{g4}\Delta_m^{T} & \delta^{g4}\Theta_m^{T} \end{bmatrix} \begin{bmatrix} \begin{bmatrix} ^{g4}K_6 \end{bmatrix}_{3\times3} & O_{3x6} \\ O_{6x3} & \begin{bmatrix} ^{g4}K_m \end{bmatrix}_{6\times6} \end{bmatrix} \begin{bmatrix} ^{g4}\Delta_6 \\ ^{g4}\Delta_m \\ ^{g}\Theta_m \end{bmatrix}. \tag{33}$$

By applying Eq. (32) in Eq. (33) the form is obtained:

$$J_{ft} \begin{bmatrix} \begin{bmatrix} {}^{g4}K_6 \end{bmatrix}_{3\times3} & O_{3x6} \\ O_{6x3} & \begin{bmatrix} {}^{g4}K_m \end{bmatrix}_{6\times6} \end{bmatrix}^{-1} J_{ft}^{T} \, {}^{g4}F_6 = {}^{g4}\Delta_{ft} \, , \tag{34}$$

and thus, the system-wide stiffness of the base the Stewart structure, which is expressed in the Stewart platform reference frame $X_4^g Y_4^g Z_4^g$, is obtained as Eq. (35):

$$^{g4}K_{ft} = \left(J_{ft} \begin{bmatrix} \begin{bmatrix} {}^{g4}K_6 \end{bmatrix}_{3\times3} & O_{3x6} \\ O_{6x3} & \begin{bmatrix} {}^{g4}K_m \end{bmatrix}_{6\times6} \end{bmatrix}^{-1} J_{ft}^{T} \right)^{-1} . \tag{35}$$

B. Stiffness modelling of a hydraulic limb

Fig. 13 shows the detailed design of the hydraulic actuator used as the driving limb of the Stewart structure.
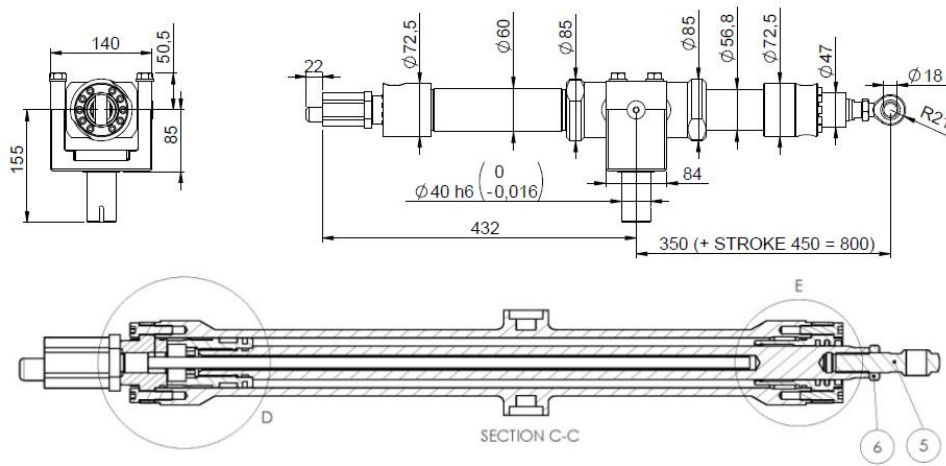
Fig.13 Design of the hydraulics actuator of the Stewart structure

The assembly of components in the hydraulic actuator are deemed to be in a serial form, and the actuator's stiffness depends on the cylinder stroke x:

$$k_{hy} = \frac{A_1^2}{(A_1*x+V_h)/B_w + A_1*x/B_c + V_h/B_h} + \frac{A_2^2}{(A_2*(l-x)+V_h)/B_w + A_2*(l-x)/B_c + V_h/B_h} \, , \tag{36}$$

where A is the area; V the volume; x the cylinder stroke; and l the cylinder length. B_w, B_c and B_h are the bulk modulus of water, the cylinder and the hose respectively. Subscripts 1 and 2 denote the corresponding chambers of the double-acting cylinder.

C. Stiffness modelling of a Stewart structure

Fig.14 shows a 3D model of the Stewart structure and its schematic diagram.
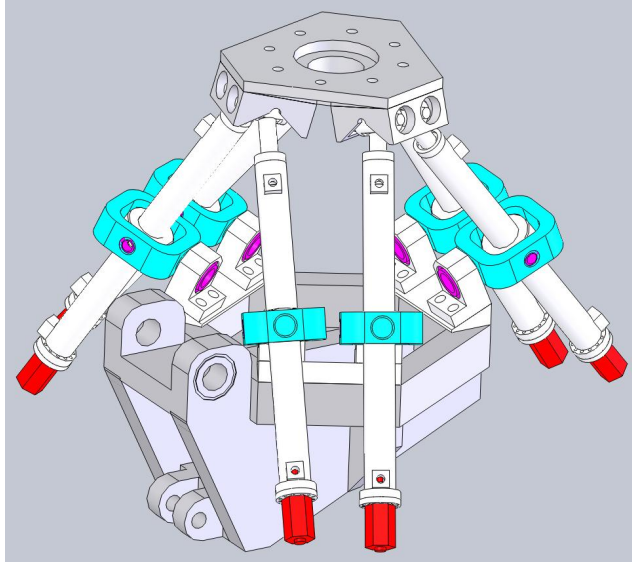
3D model of the Stewart structure
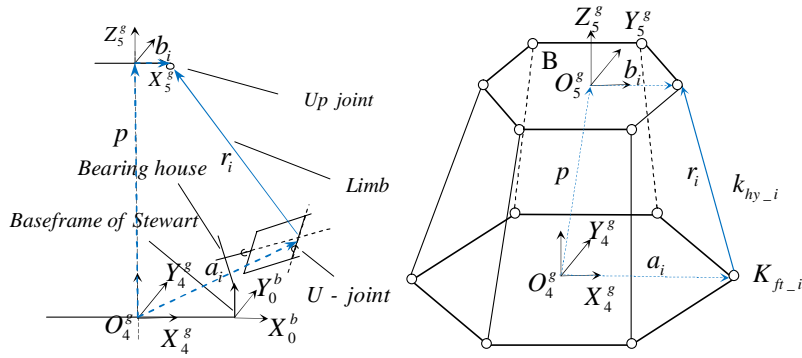
Schematic diagram of the Stewart structure

Fig.14 3D model of the Stewart structure and schematic diagram

Referring to the schematic diagram in Fig.14, a loop-closure equation for the ith limb of the Stewart structure can be written as:

$$p + b_i = a_i + r_i, \tag{37}$$

where the subscript i denotes the ith limb of the Stewart limb; p the vector from the origin of the Stewart platform reference frame $X_4^g Y_4^g Z_4^g$ to the origin of the end-effector reference frame $X_5^g Y_5^g Z_5^g$; b_i the vector from the origin of the end-effector reference frame to the up-joint; a_i the vector from the origin of the platform reference frame to the kinematic end tip (node 6) of the base structure; and r_i the vector from the base structure to the up-joint. Notice that all the vectors in Eq. (37) are expressed in the Stewart platform reference fame.

Differentiating Eq. (37) gives:

$$\Delta_B + \Theta_B \times b_i = \Delta_{fti} + l_i(\Theta_{fti} \times S_i) + \delta l_i * S_i, \tag{38}$$

where Δ_B and Θ_B can be regarded as the system-wide translational and rotational deformations of the end-effector with respect to the platform reference frame; Δ_{fti} and Θ_{fti} denote the translational and rotational deformations of the base structure in the ith limb; l_i denotes the length of the ith limb before the deformation; δl_i denotes its linear deformation; and S_i is the unit vector of the ith limb.

Dot-multiplying both sides of Eq. (38) by S_i and writing the obtained equation in matrix form yields:

$$\begin{bmatrix} S_i^T & -(S_i \times b_i)^T \end{bmatrix} \begin{bmatrix} \Delta_B \\ \Theta_B \end{bmatrix} = \begin{bmatrix} 1 & S_i^T \end{bmatrix} \begin{bmatrix} \delta l_i \\ \Delta_{fti} \end{bmatrix}, \tag{39}$$

or simply:

$$J_{xi} \begin{bmatrix} \Delta_B \\ \Theta_B \end{bmatrix} = J_{qi} \Delta_{Li}, \tag{40}$$

where $J_{xi} = \begin{bmatrix} S_i^T & -(S_i \times b_i)^T \end{bmatrix}$, $J_{qi} = \begin{bmatrix} 1 & S_i^T \end{bmatrix}$, $\Delta_{Li} = \begin{bmatrix} \delta l_i & \Delta_{fti}^T \end{bmatrix}^T$.

Applying Eq. (40) on all 6 limbs of the Stewart structure and assembling the obtained equations into matrix form yields:

$$\begin{bmatrix} \Delta_B \\ \Theta_B \end{bmatrix} = J_{stw} \Delta_L, \tag{41}$$

where:

$$J_{stw} = \begin{bmatrix} J_{x1} \\ J_{x2} \\ J_{x3} \\ J_{x4} \\ J_{x5} \\ J_{x6} \end{bmatrix}^{-1} * diag[J_{qi}] = \begin{bmatrix} S_1^T & -(S_1 \times b_1)^T \\ S_2^T & -(S_2 \times b_2)^T \\ S_3^T & -(S_3 \times b_3)^T \\ S_4^T & -(S_4 \times b_4)^T \\ S_5^T & -(S_5 \times b_5)^T \\ S_6^T & -(S_6 \times b_6)^T \end{bmatrix}^{-1} * diag[J_{qi}], \tag{42}$$

$$\Delta_L = \begin{bmatrix} \Delta_{L1} \\ \Delta_{L2} \\ \Delta_{L3} \\ \Delta_{L4} \\ \Delta_{L5} \\ \Delta_{L6} \end{bmatrix}. \tag{43}$$

If $\delta\Delta_B$, $\delta\Theta_B$ and $\delta\Delta_{Li}$ denote the virtual displacement of the end-effector and the ith limb of the Stewart structure based on the current deformations, then applying the virtual work principle in the kinematic chain of deformations yields:

$$\begin{bmatrix} \delta\Delta_B{}^T & \delta\Theta_B{}^T \end{bmatrix} * \begin{bmatrix} F_B \\ M_B \end{bmatrix} = \sum_{i=1}^{6} \delta\Delta_{Li}^T * \begin{bmatrix} k_{hyi} & O_{1x1} \\ O_{6x6} & K_{fti} \end{bmatrix} * \Delta_{Li}, \tag{44}$$

or simply:

$$\begin{bmatrix} \delta\Delta_B{}^T & \delta\Theta_B{}^T \end{bmatrix} * \begin{bmatrix} F_B \\ M_B \end{bmatrix} = \delta\Delta_L^T * diag[K_{li}] * \delta\Delta_L, \tag{45}$$

where k_{hyi} stands for the stiffness of the ith hydraulic actuator; and K_{fti} the stiffness matrix of the base structure in the ith limb. In Eq. (45), $K_{li} = diag[k_{hyi} \quad K_{fti}]$.

By applying Eq. (41) in Eq. (45), the stiffness matrix of the Stewart structure is obtained as Eq. (46):

$$K_{stw} = (J_{stw} * [diag[K_{li}]]^{-1} * J_{stw}{}^T)^{-1}. \tag{46}$$

3.2.2 Stiffness modelling of a serial-parallel robot

From the overview of the IWR configuration, the entire Stewart structure can be considered as a virtual link, therefore the kinematic configuration of the hybrid serial-parallel robot can be deemed to be in a serial form. By applying the VJM variant on the entire Stewart structure, the flexibility of this virtual link can be obtained by analyzing

the motions of a virtual joint with 6 DOF attached at the centre of the end-effector reference frame while the virtual link is regarded as rigid. Fig.15 shows a deformation kinematics diagram of this serial-parallel robot by introducing the virtual joint variant into all the flexible links.
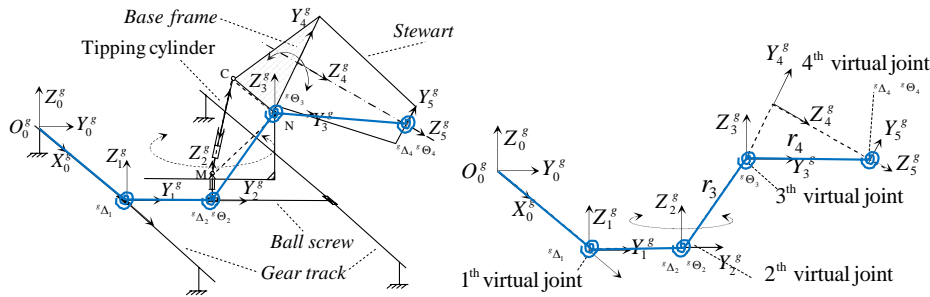
Fig.15 Deformation kinematics of the serial-parallel robot

The deformation occurring in the tipping cylinder will transfer to the passive joint 3 as a rotational flexibility, where the virtual joint 3 is introduced for the equivalence of this flexibility. The translational deformation occurring in the ball screw and the rotational deformation in the rotating table are postulated to be accomplished by the virtual joint 2 with 2 DOF motions. The deformation occurring between the pinion and rack on the track is postulated to be accomplished by the virtual joint 1.

A. Stiffness modelling of the tipping joint

Fig.16 shows a 3D model of the tipping mechanism of the base of the Stewart structure and its schematic representation.
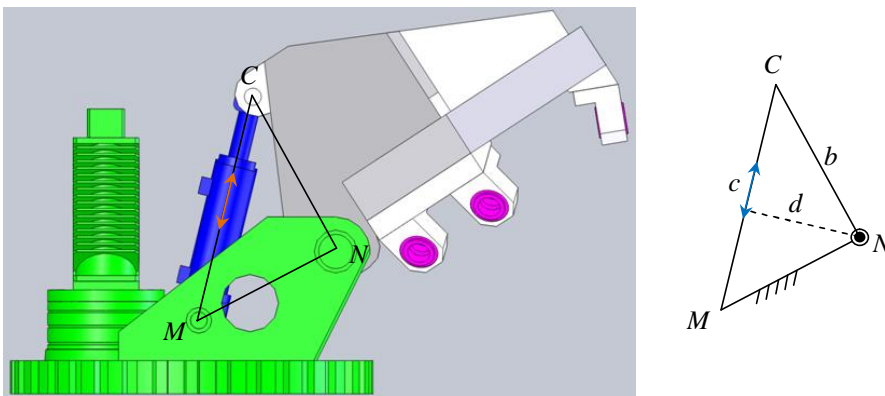
Fig.16 3D model of the tipping mechanism of the base of the Stewart structure and its schematic representation

In Fig.16, M, N and C denote the centers of the corresponding joints. c and b denote the scalar lengths from joint M to C and from joint N to C, while d denotes the scalar vertical distance from joint N to the line MC.

The deformation equilibrium equation of a tipping cylinder can be written as:

$$f = k_t * \delta c , \tag{47}$$

where k_t is the stiffness of the hydraulic actuator; f is the force acting along the cylinder direction; and δc is the deformation of the cylinder.

Let $\delta \theta$ denote the rotational deformation of the rigid link NC, which results from the deformation of the cylinder, then:

$$\delta c = d * \delta \theta . \tag{48}$$

Substituting Eq. (48) into Eq. (47) and multiplying d on both sides of the equation, we obtain:

$$m = d^2 * k_t * \delta \theta , \tag{49}$$

or simply:

$$m = k_3 * \delta \theta , \tag{50}$$

where m denotes the equivalent moment of f acting on the tipping joint; and $k_3 = d^2 * k_t$ denote the rotational stiffness of the tipping joint. Expressing k_3 in the global reference frame yields K_3, which is in the form of a 3x3 matrix.

B. Stiffness modelling of a serial-parallel robot

Let $^g\Delta$ and $^g\Theta$ denote the system-wide translational and rotational deformations of the end-effector with respect to the global reference frame $X_0^g Y_0^g Z_0^g$; $^g\Delta_4$ and $^g\Theta_4$ denote the local translational and rotational deformations of the Stewart structure in the virtual joint 4 with respect to the base reference frame $X_4^g Y_4^g Z_4^g$; $^g\Theta_3$ denote the local rotational deformation of the Stewart base in the virtual joint 3 with respect to the reference frame $X_3^g Y_3^g Z_3^g$; $^g\Theta_2$ and $^g\Delta_2$ denote the local rotational deformation of the rotation table and the translational deformation of the ball screw respectively with respect to the reference frame $X_2^g Y_2^g Z_2^g$, which are lumped into the virtual joint 2; and $^g\Delta_1$ denote the deformation of the robot along the rack with respect to the reference frame $X_0^g Y_0^g Z_0^g$, which is lumped into the virtual joint 1. Referring to the deformation kinematics of the serial-parallel robot in Fig.15, we can obtain:

$$
\begin{bmatrix} {}^g\Delta \\ {}^g\Theta \end{bmatrix} = \begin{bmatrix} I_{3x3} & O_{3x3} & -r_4\times & I_{3x3} & -(r_3+r_4)\times & I_{3x3} \\ O_{3x3} & I_{3x3} & I_{3x3} & O_{3x3} & I_{3x3} & O_{3x3} \end{bmatrix} \begin{bmatrix} {}^g\Delta_4 \\ {}^g\Theta_4 \\ {}^g\Theta_3 \\ {}^g\Delta_2 \\ {}^g\Theta_2 \\ {}^g\Delta_1 \end{bmatrix}, \tag{51}
$$

or simply:

$$
\begin{bmatrix} {}^g\Delta \\ {}^g\Theta \end{bmatrix} = J_{IWR} \begin{bmatrix} {}^g\Delta_4 \\ {}^g\Theta_4 \\ {}^g\Theta_3 \\ {}^g\Delta_2 \\ {}^g\Theta_2 \\ {}^g\Delta_1 \end{bmatrix}, \tag{52}
$$

where:

$$
J_{IWR} = \begin{bmatrix} I_{3x3} & O_{3x3} & -r_4\times & I_{3x3} & -(r_3+r_4)\times & I_{3x3} \\ O_{3x3} & I_{3x3} & I_{3x3} & O_{3x3} & I_{3x3} & O_{3x3} \end{bmatrix} \tag{53}
$$

denotes the Jacobian matrix between the system-wide deformations of the end-effector and the deformations of the virtual joints. In Eq. (51), r_3 and r_4 denote the vectors from virtual joint 2 to virtual joint 3 and from virtual joint 3 to virtual joint 4, respectively; $r_4\times$ and $(r_3+r_4)\times$ denote the skew matrices of vectors r_4 and r_3+r_4 respectively.

Let K_2 and K_1 denote the stiffness of virtual joint 2 and virtual joint 1 expressed in the global reference frame $X_0^g Y_0^g Z_0^g$ respectively (Fig.15); and $\begin{bmatrix} \delta^g\Delta^T & \delta^g\Theta^T \end{bmatrix}^T$ and $\begin{bmatrix} \delta^g\Delta_4^T & \delta^g\Theta_4^T & \delta^g\Theta_3^T & \delta^g\Delta_2^T & \delta^g\Theta_2^T & \delta^g\Delta_1^T \end{bmatrix}^T$ denote the system-wide virtual displacements of the end-effector and the virtual displacements of the virtual joints based on the occurred deformations. Applying the virtual work principle on the entire serial-parallel robot gives:

$$
\begin{bmatrix} \delta^g\Delta^T & \delta^g\Theta^T \end{bmatrix} * \begin{bmatrix} {}^gF \\ {}^gM \end{bmatrix} = \begin{bmatrix} \delta^g\Delta_4^T & \delta^g\Theta_4^T & \delta^g\Theta_3^T & \delta^g\Delta_2^T & \delta^g\Theta_2^T & \delta^g\Delta_1^T \end{bmatrix} * diag\begin{bmatrix} K_{stw} & K_3 & K_2 & K_1 \end{bmatrix} * \begin{bmatrix} {}^g\Delta_4 \\ {}^g\Theta_4 \\ {}^g\Theta_3 \\ {}^g\Delta_2 \\ {}^g\Theta_2 \\ {}^g\Delta_1 \end{bmatrix}. \tag{54}
$$

By applying Eq. (52) in Eq. (54), we obtain:

$$K_{IWR} = \left(J_{IWR} * \left[diag\left[K_{stw} \quad K_3 \quad K_2 \quad K_1 \right] \right]^{-1} * J_{IWR}^T \right)^{-1}, \qquad (55)$$

which represents the analytical stiffness model of the entire serial-parallel robot.

3.2.3 Numerical results

Based on the obtained stiffness model, the stiffness performance of the IWR was investigated along the border lines of a prescribed workspace, shown in Fig17.
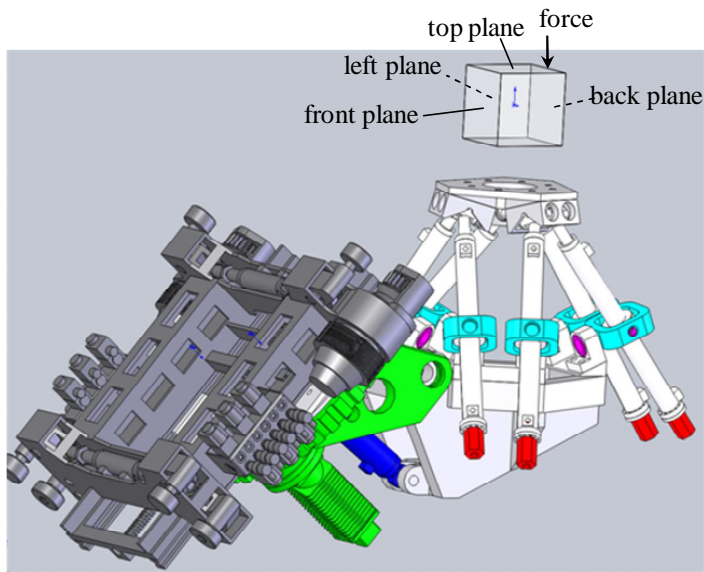
Fig.17 Prescribed cubic volume workspace of IWR

The workspace is 450 mm above the plane of the end-effector, and in the form of a 200x200x200 mm^3 cubic volume. The external load is exerted vertical to the end-effector plane and has a value of 5 kN. In the numerical example, the prescribed workspace is reached by the Stewart structure and the serial part of the robot remains still.

The numerical results of computation of the deformations of the robot are shown in Fig. 18.
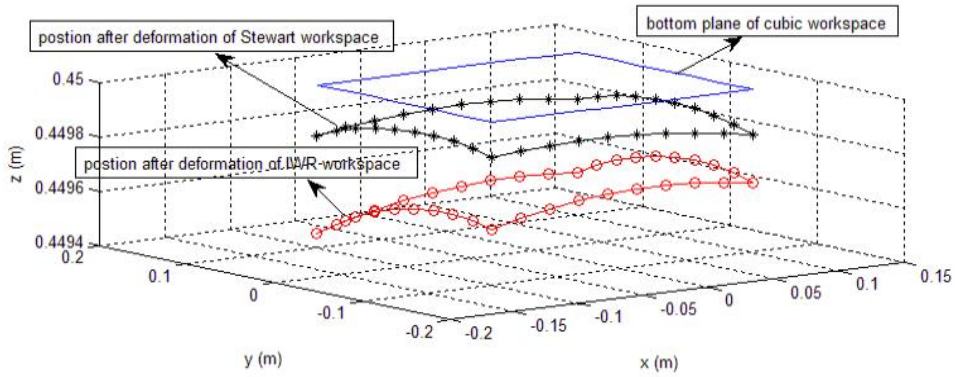
(i). Deformation of the robot on the bottom plane of the workspace
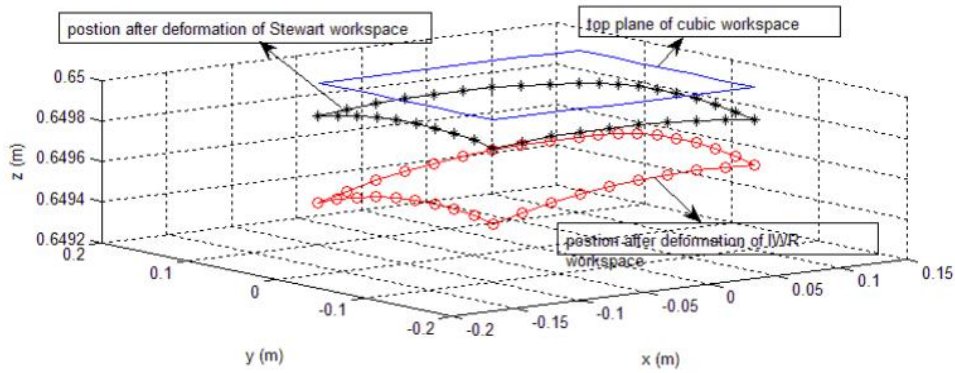
(ii) Deformation of the robot on the top plane of the workspace
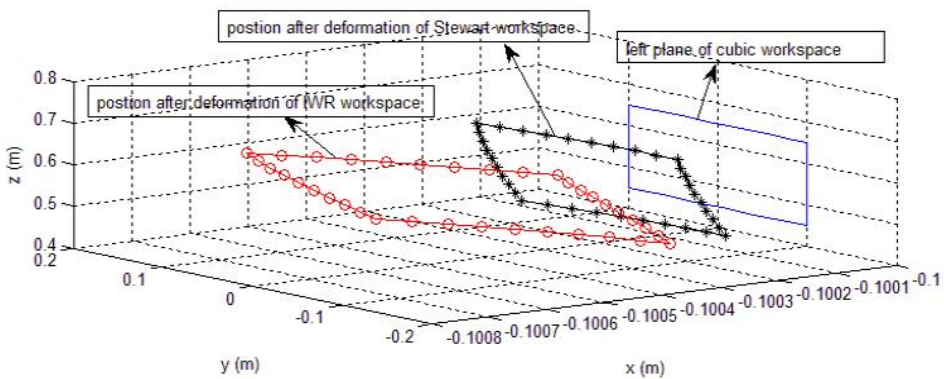
(iii) Deformation of the robot on the left plane of the workspace
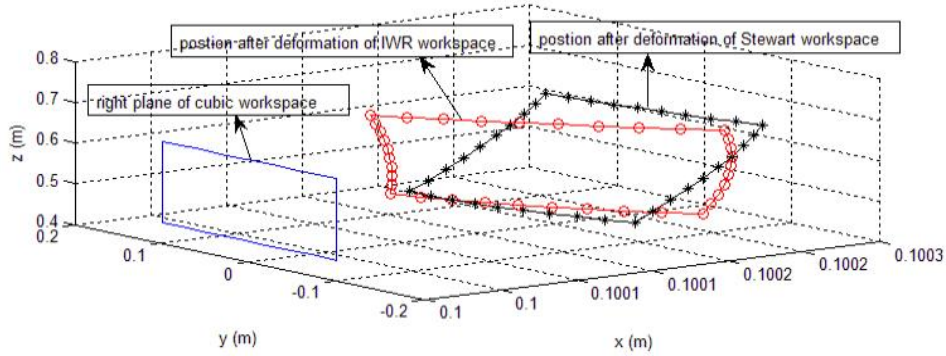
(iv) Deformation of the robot on the right plane of the workspace
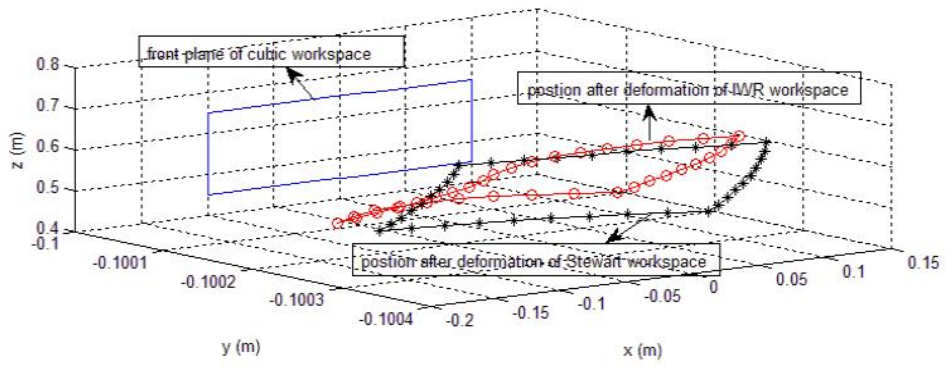
(v). Deformation of the robot on the front plane of the workspace
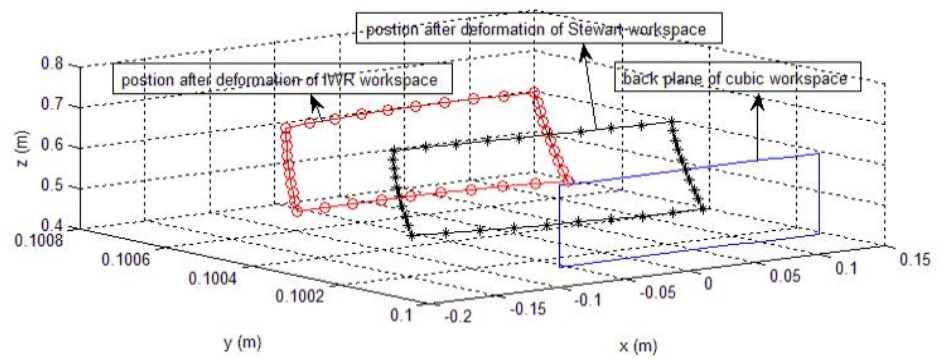
(vi) Deformation of the robot on the back plane of the workspace

Fig.18 Deformation of the robot workspace: (i) on the bottom plane of the workspace; (ii) on the top plane of the workspace; (iii) on the left plane of the workspace; (iv) on the

right plane of the workspace; (v) on the back plane of the workspace; (vi) and on the front plane of the workspace

In Fig.18, the continuous line denotes the borders of the prescribed workspace without external load; the starred-line denotes the new border positions of the workspace following deformation of the Stewart structure due to the external load, given that the serial part in the robot is assumed to be rigid; and the line with circles denotes the new border positions of the workspace due to the deformations of the entire robot, which account for both deformations from the Stewart structure and from the serial parts of the robot.

It should be noted that in some parts of the workspace in Fig.18 (iv) and Fig.18 (v), the deformation of the entire robot under the assumption of a rigid serial part is larger in some directions than the deformation under the assumption of a flexible serial part. The reason for this result is that the redundant flexibility in the serial part of the robot allows the deformation of the robot to occur in other possible directions, which to some extent can mitigate the deformation of the parallel part along one direction. This phenomenon can also be interpreted from the energy point of view, since the flexible serial parts can absorb the external energy in other deformation directions. Moreover, it implies that the system-wide stiffness performance of the robot can be optimized at the prescribed workspace due to the existence of redundant flexible kinematics.

3.3 Stiffness-Maximum Trajectory Planning of **a** Hybrid Robot

In this section, a set of trajectories in the robot joints space are generated for a prescribed trajectory of the end-effector in the Cartesian space. The best stiffness performance along the prescribed trajectory is taken as a constraint for the joints trajectory planning. In the dissertation, the stiffness performance is evaluated by the least eigenvalue of the system-wide stiffness matrix. Taking the maximum stiffness performance as the objective, the differential evolution (DE) algorithm is employed to search for the global optimum in the multi-dimensional joints space under the constraint of inverse kinematics. The numerical results of the generated joints trajectories are presented for a prescribed end-effector trajectory at the end of this section.

3.3.1 Index of stiffness performance

It is well known that the stiffness reflects the relationship between the external force and the corresponding displacement experienced. Numerically, this property can be defined by a 6x6 matrix. However, it is rather difficult to evaluate the stiffness performance in terms of a matrix, since it is not comparable by means of vectors. An instinctive way to evaluate the stiffness performance is the use of elements of interest inside the matrix. However, an individual element only represents the relation between the force and the

deformation in a certain direction without considering the coupling effects of other terms in the matrix.

An applicable approach for stiffness performance evaluation is to investigate the characteristics of the matrix in the form of scalars, i.e., the eigenvalues, the determinant, the diagonal terms and the condition number of the matrix [71]. Of these commonly used indicators, the eigenvalue is adopted here as the most reasonable index for the application considered in this work.

To interpret the eigenvalue of the stiffness matrix geometrically, it is postulated that for a 6x6 stiffness matrix, a set of deformation vectors in arbitrary directions can be found and the deformation vectors form a spherical shape in a 6-dimensional space, given that the magnitude of each deformation vector is equal to unit length. The corresponding set of causative force vectors then form an ellipsoid in the 6-dimensional space, in which the lengths of the principle axes are the eigenvalues of the stiffness matrix and the related eigenvectors represent the directions of the principle axes [29][30]. Based on this point, the minimum eigenvalue represents the minimum stiffness performance in its eigenvector direction.

For a specific stiffness matrix, it can be considered that the minimum stiffness performance is dominated by the least eigenvalue of the matrix. If the least eigenvalue can be as larger as possible, then we think the overall stiffness performance for such specific matrix is maximized. Thus, for a fixed location of end-effector of IWR, the optimum stiffness is defined by the maximum value in all possible least eigenvalues generated based on the different kinematics configurations.

Mathematically, for an arbitrary kinematics configuration of IWR, the set of eigenvalues for the corresponding stiffness matrix can be represented by Eq. (56) as follows:

$$\{\lambda_{ji}\} = eig(K_j), \ i = 1, \ 2, \ ..., \ 6. \tag{56}$$

where the subscript j denotes an arbitrary kinematics configuration of IWR; i denotes the ith eigenvalue; $\{\lambda_{ji}\}$ denotes the set of eigenvalues for such an arbitrary kinematics configuration j; and K_j denotes the corresponding stiffness matrix. Then, the least eigenvalue in the set denoted by $\{\lambda_{ji}\}$ can be described by Eq. (57) as follows:

$$\lambda_{least\_j} = \min\{\lambda_{ji}\}. \tag{57}$$

Let R represent the set of all the possible kinematics configurations of IWR for the given location of the end-effector, then the maximum stiffness performance of IWR in all the possible kinematics configurations R can be described by Eq. (58) as follows:

$$\lambda_{best} = \max_{j \in R}\{\lambda_{least\_j}\}, \tag{58}$$

where $\{\lambda_{least\_j}\}$ represents the set of corresponding least eigenvalues in the kinematics set R.

3.3.2 Stiffness optimization and trajectory generation

A. Differential evolution (DE) algorithm applied in stiffness optimization

For a prescribed location of end-effector, the robot system-wide stiffness performance λ_{least_j} is taken as the objective of the optimization process, and the 4 redundant joint position values in the serial parts of the robot, which actually determine the kinematics configuration of IWR, are taken as the input variables of the DE algorithm. Determination of the kinematics configuration in the redundant robot IWR involves 10 position values in the joints space. However, these 10 parameters are linear dependent for a given location of end-effector and the 4 parameters from the serial parts of IWR can form a linear independent set. This implies that for a given location of end-effector, once the 4 position values of the joints in the serial parts are chosen, the remaining 6 position values in the Stewart structure joints are consequently determined by the inverse kinematics.

Fig.19 shows the abstract steps of the DE algorithm applied in the stiffness optimization of IWR [32].
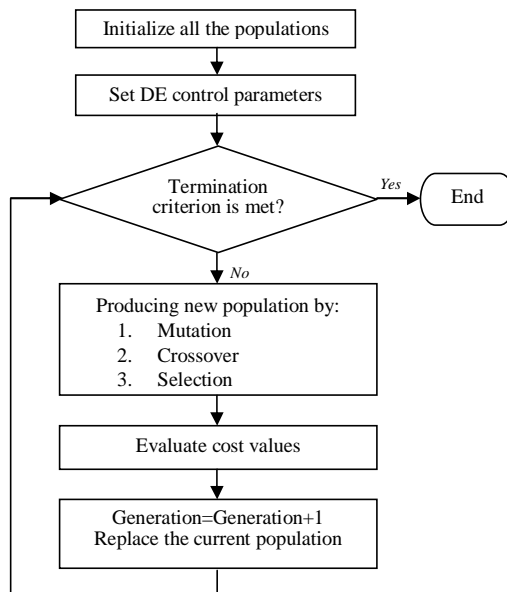
Fig.19 Flow chart of the DE algorithm

First, the populations and the control parameters of the DE algorithm are initialized by some random values. Herein, the population consists of a set of joints position values in the serial parts of IWR. For setting of the control variables of the DE, *CR* is assigned to be 0.7, *F* is equal to 0.8; *NP* is set to be 40; and the standard deviation of the population (1.0E-5) is regarded as the termination criterion. Then the algorithm starts to proceed and check if the termination criterion for the optimization process is satisfied or not (e.g. number of iterations performed, or adequate fitness reached). If the criterion is not met, a new population, which is produced by the algorithm and which consists of mutation, crossover and selection, will be taken to be compared with the old one by calculating the cost values. The new population generation of the algorithm guarantees that all individuals of the next generation are as good as or better than individuals of the current population. The process is repeated until the termination criterion is reached.

B. Trajectory generation in joints space

Fig.20 shows the input variables of the DE algorithm in the kinematics of IWR.
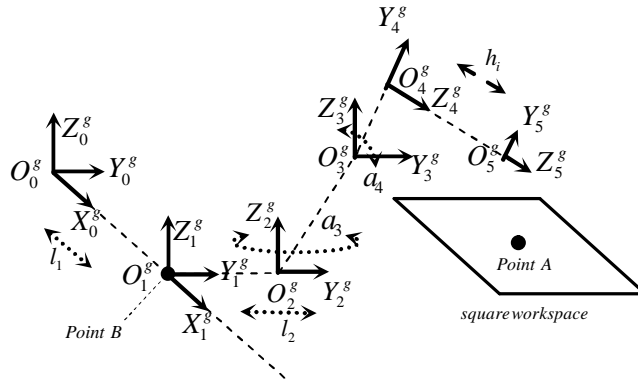
Fig.20 Input variables of the DE algorithm in the kinematics of IWR

Let l_1 represent the linear displacement of frame $X_1^g Y_1^g Z_1^g$ along the rack on the track; l_2 the linear displacement of frame $X_2^g Y_2^g Z_2^g$ along the ball screw; a_3 the rotation angular of frame $X_3^g Y_3^g Z_3^g$ around the Z_2^g axis; a_4 the rotation angular of frame $X_4^g Y_4^g Z_4^g$ around the X_3^g axis; and for the parallel mechanism, let h_i *(i = 1,2...6)* denote the length of the Stewart limb. Eq. (58) can then be written as:

$$\lambda_{best} = f(l_1, l_2, a_3, a_4). \tag{59}$$

For the physical constraints in the robot joints, the values of the input variables in the population (l_1, l_2, a_3, a_4) for the DE are limited to be in the ranges of $[0, 4]$ m, $[0, 0.5]$ m, $[0, 360]$ degree and $[-88, -42]$ degree respectively, and the initial values of the population are assigned by randomly selecting values within the range boundaries.

In practical application of IWR, when the trajectory of the end-effector is prescribed, by applying the DE algorithm, all the 10 joints position values at the beginning point of the path (assuming this is located at point *A* in Fig.20) can be obtained subject to the maximum stiffness performance. We postulate that the frame $X_1^g Y_1^g Z_1^g$ moved to the point *B* on the track according to the joints position values generated from the first optimization results. However, during the rest machining process, the carriage, namely the frame $X_1^g Y_1^g Z_1^g$, will stop at point *B* of the track, and the rest path of the end-effector trajectory will be accomplished by driving the rest 9 joints. The reason behind is that the accuracy of the position control on the rack of the track is not high enough for a good quality of finished surface during the machining process. In this case, the number of redundant freedoms is reduced to three in the serial parts of IWR, and the population of DE is also reduced to a new set, which consists of parameters l_2, a_3 and a_4. Therefore, the objective function of DE for the rest machining trajectory is reconstructed as Eq.(60):

$$\lambda_{best} = f(l_2, a_3, a_4). \tag{60}$$

In other words, for the first work point *A* in the prescribed workspace, the optimum stiffness performance is searched in the joint space of 10 freedoms. Thereafter, the robot will be working under 9 freedoms, the workspace excluding point *A*, which is subject to the best stiffness performance, is then reached by actuating l_2, a_3, a_4 as well as the Stewart limb h_i.

In order to validate the feasibility of applying the DE in the stiffness optimization of IWR, an arbitrary start point *A* in the workspace is first chosen for the evaluation. Let the point *A* be assigned with the coordinates of $[1.5, 1.0, 0, 150, 0, -150]^T$, in which the first three entries specify the position of the end-effector and the remaining three entries specify the orientation by means of Roll-Pitch-Yaw angles in the global frame $X_0^g Y_0^g Z_0^g$. Then, the convergence process for searching for the optimum stiffness is as illustrated in Fig 21.
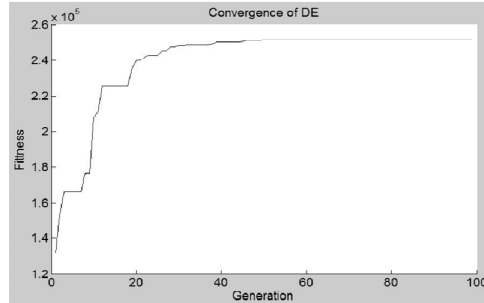
Fig.21 Convergence of the DE for searching for the optimum stiffness at point *A*

It can be observed that the DE reaches convergence after around 50 iterations, and the best input parameters, which are the position values of the joints in the serial parts of IWR, are obtained as $l_1 = 1.8682$ m, $l_2 = 0.3621$ m, $a_3 = 30.0206^0$, and $a_4 = -74.9323^0$ respectively. The lengths of the Stewart limbs can be computed by the inverse kinematics.

In the following step, the workspace is extended from the beginning point *A* to a 200x200mm^2 square, point *A* is located at the geometric centre of this area, and the height of the end-effector and its orientation are maintained as at point *A*. DE to is then applied to search for the best stiffness with the objective function (60) over this specific workspace. The optimum stiffness surface found is shown in Fig 22.
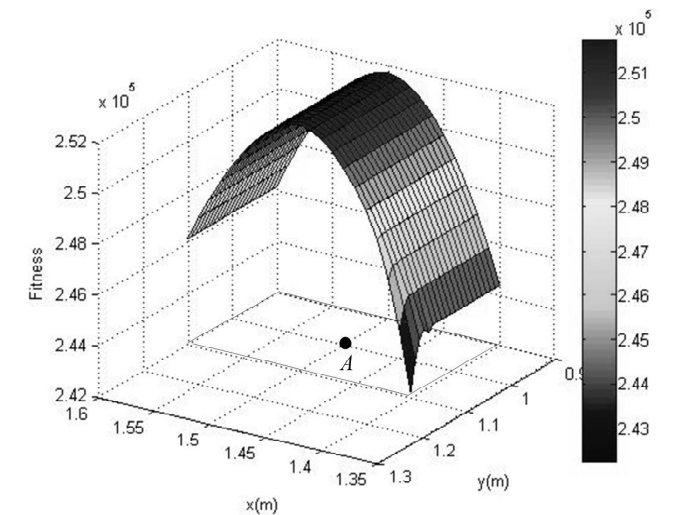
Fig.22 Optimum stiffness surface over the 200x200mm^2 square

In Fig 22, the *x*-axis direction is parallel to the track and the *y*-axis direction is perpendicular to the track. It is found that the stiffness performance of point *A* exhibits

the best results in the 200x200 mm^2 plane workspace, because the best stiffness of point A is searched for in the joint space of 10 degrees of freedom while the other points are searched for in joint spaces of 9 degree of freedom due to the fixed carriage position on the track. The stiffness decreases along both the positive and negative directions of the *x*-axis when the end-effector moves away from point *A*, because the displacement of the end-effector along the track is contributed mainly by the stretching of the Stewart, and the stiffness of the Stewart becomes weaker if the limb stretches longer. The stiffness also decreases along both directions of the *y*-axis, but the change is much smaller compared with that of the *x*-axis, because the displacement along the *y*-axis is implemented mainly by the ball screw, which has much smaller stiffness deviation than the hydraulic limbs in the Stewart.

In the following example, a set of trajectories in the joints space are generated for a prescribed trajectory of end-effector, which is a straight line of 200 mm in length parallel to the track on the *x-y* plane of the global frame $X_0^g Y_0^g Z_0^g$, as shown in Fig.23.
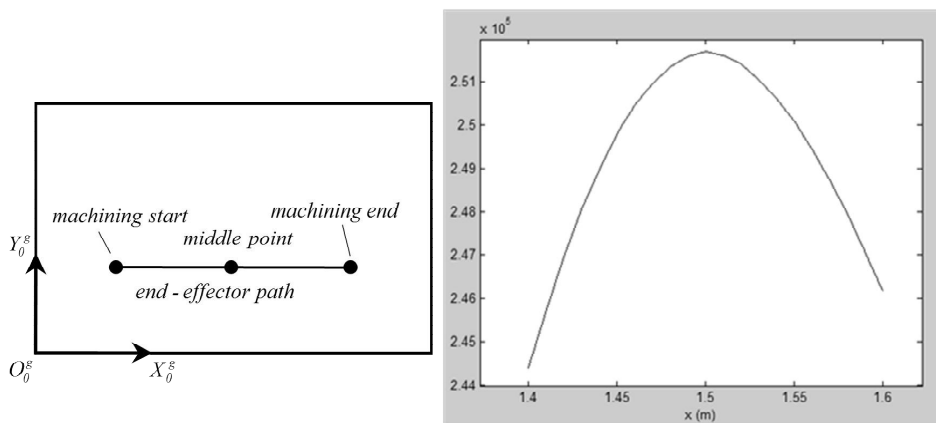
Fig.23 Straight line path and best stiffness along the path

The speed of the end-effector is set to 2mm/s. The middle point of the path in the prescribed trajectory is selected as the initial point of the optimization under 10 joints freedom, and the coordinate of the middle point is set to $[1.5, 1.0, 0, 150, 0, -150]^T$ with respect to the global frame. Notice that although the generation of joints trajectories begins from the middle point of the path, in the practical machining process the robot end-effector starts to work from the tip of the prescribed trajectory. Utilizing the DE algorithm to optimize the stiffness performance along the prescribed straight-line trajectory of end-effector obtained the joints trajectories plotted in Fig 24.
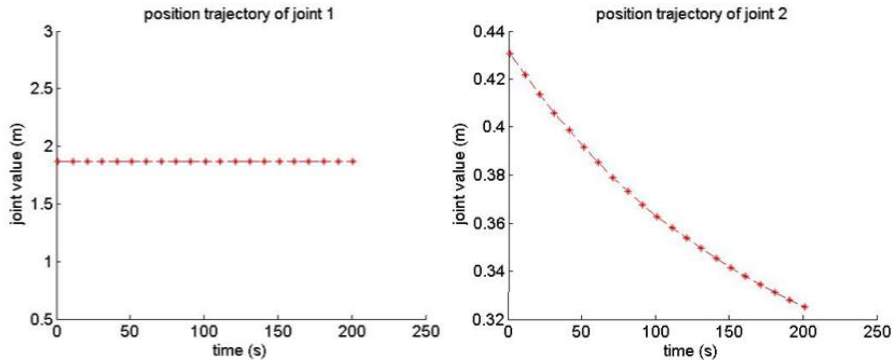
(i). Linear position trajectories of joints parallel to the track and vertical to the track
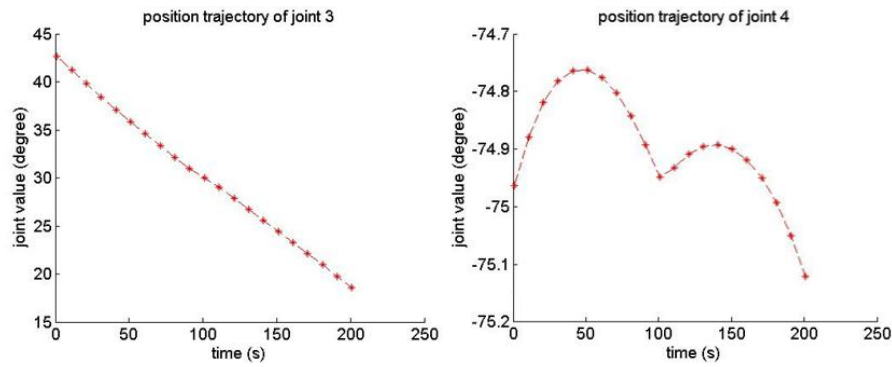
(ii). Rotation trajectories of the rotation table and Stewart base
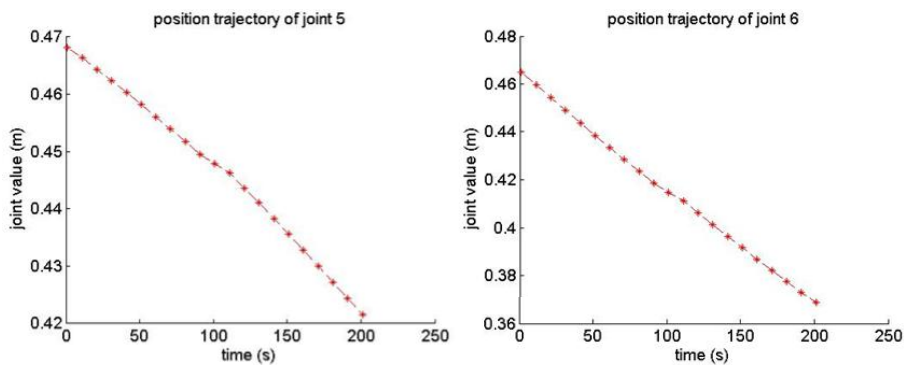
(iii). Linear position trajectories of limb 1 and limb 2 in the Stewart
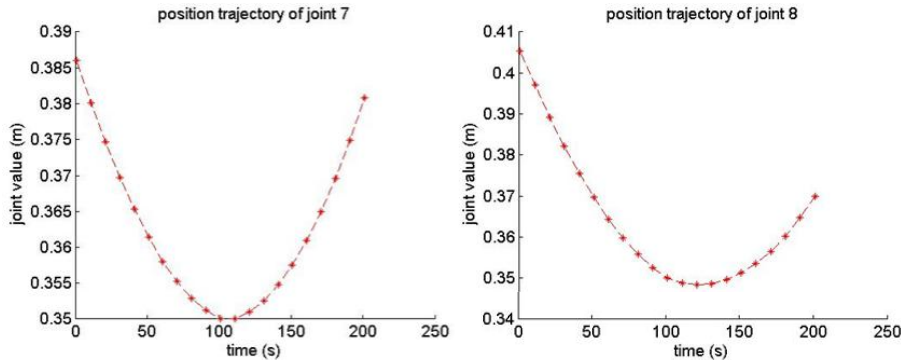
(iv). Linear position trajectories of limb 3 and limb 4 in the Stewart
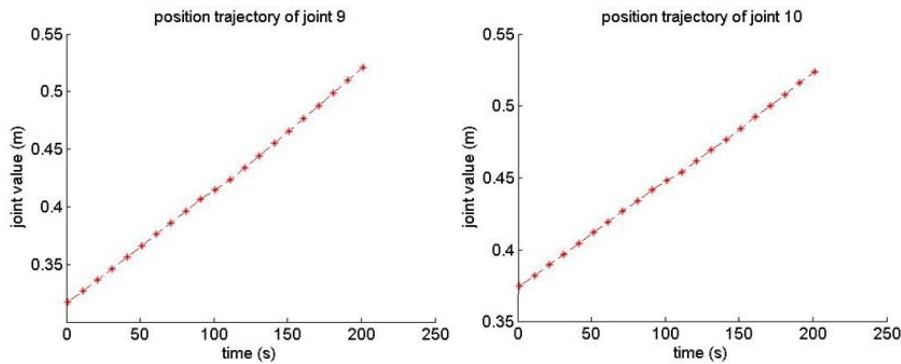
(v). Linear position trajectories of limb 5 and limb 6 in the Stewart

Fig.24 Position trajectories of the driving joints in the hybrid robot

From Fig.24 (i), it can be seen that the trajectory of the first joint is maintained constant, because the carriage of IWR (serial part base) has been fixed on the track after the first optimization. The figures show that all the generated trajectories in the joints space based on the best stiffness performance are acceptably smooth, which indicates the feasibility of their realization in the control system.

3.4 Conclusions

This section described the construction of a system-wide stiffness model of a hybrid serial-parallel robot machine by employing a variant of the virtual joint method and the virtual work principle. In order to apply the variant of the virtual joint method, the MSA method is utilized to compute a stiffness matrix of the elemental consisting flexible link in the robot. In the dissertation, the variant of the virtual joint method is utilized to build up a system-wide stiffness model for the robotic system that accounts for more deformation directions than possible with the lumped modelling method.

To evaluate the overall stiffness performance of the robot, the least eigenvalue of the stiffness matrix, which represents the weakest stiffness performance of the robot, is taken as the performance index. In order to get optimal stiffness performance of the robot in an arbitrary direction, the least eigenvalue of the stiffness matrix has to be optimized to be as large as possible. Thus, the least eigenvalue of the stiffness matrix is taken as the optimization objective to obtain the maximum overall stiffness performance of the hybrid robot machine IWR. A DE algorithm, in which the joints position values of IWR are taken as the searching variables, is utilized in the optimization due to its global optimization ability.

A set of feasible trajectories in the joints space of IWR along which the overall stiffness performance of the robot has been maximized are generated for a prescribed trajectory of end-effector. The numerical results of the generated trajectories indicate that joint trajectories based on overall stiffness optimization of the robot are acceptably smooth for realization in the control system. Furthermore, the results imply that the stiffness performance of a robot machine deviates smoothly with respect to the kinematic configuration in the adjacent domain of its best stiffness performance.

CHAPTER 3

FEEDFORWARD BASED VIBRATION CONTROL

In this chapter, a feedforward based control strategy is introduced for the suppression of vibration in the end-effector of the robot machine, which is caused by the external varying force. An inverse dynamics model is employed in the feedforward path. In order to construct an accurate inverse dynamics model of the target system, a neural network is employed to identify unknown parts in the dynamics modelling process. A modified Levenberg-Marquardt algorithm is utilized to train the neural network using indirect training data for the unknown models.

4.1 Feedforward Control Strategy for Vibration Suppression

Feedforward control is often used together with feedback control for disturbance rejection in practice. Feedback control can provide satisfactory trajectory tracking accuracy for a system without external disturbance and, to some extent, can guarantee system stability when the external disturbance is within the bandwidth of the control system. Although both feedback control and feedforward control are applied in the systems discussed in this work, the dissertation research only considers feedforward control.

In general, feedforward control can be introduced for disturbance rejection when the disturbance signal on the target system is available. An adaptive filter is often adopted in the feedforward control path. Fig.25 shows the basic principle of such feedforward control strategies.
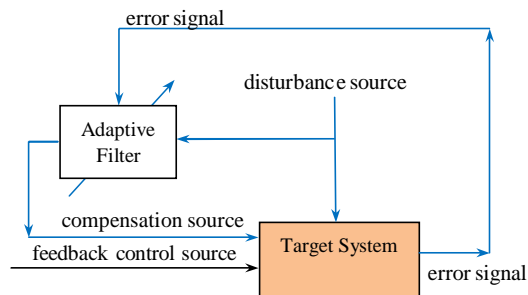
Fig.25 Principle of feedforward control based on an adaptive filter

The disturbance source is fed forward into an adaptive filter, which yields a compensative source as the input signal of the system to cancel out the effect of the disturbance. The filter coefficient is deemed to be well adapted or tuned when the error signal from the target system is minimized at one or several points of interest. One prominent advantage of such feedforward control is that it can work at any frequency; furthermore, feedforward control is less sensitive to phase lag than feedback control. However, the

performance of such adaptive filters is not global, which means that the adaptive filter is only effective on a specific disturbance over well-tuned points. The principle behind this sort of adaptive filter is akin to approximating an 'inverse dynamics model' from the disturbance source to the input source of the system that can produce a result equal to the disturbance but with the opposite sign to cancel out the disturbance.

In the IWR, the disturbance source acting on the robot system mainly stems from the varying cutting force. Consequently, a wide range of disturbance exists, as machining is done on different materials. An adaptive filter approach is thus not suitable for feedforward control of the end-effector path, due to the localized performance of the filters. However, the concept of feedforward control is still attractive for disturbance rejection in the robotic machine, since an inverse dynamics model can be constructed and applied in the feedforward control path instead of the adaptive filter. Fig.26 shows the concept of such an inverse dynamics model based feedforward control strategy.
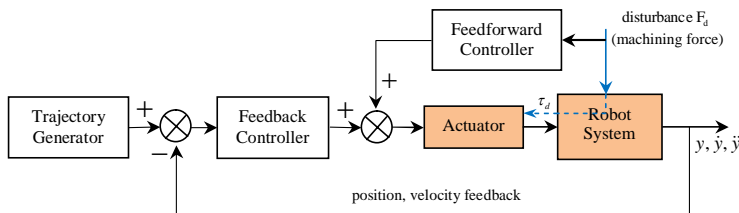
Fig.26 Feedforward control of the robot system

When the robotic machine in Fig.26 is controlled without the machining task, the trajectory tracking accuracy obtained by the feedback controller is quite satisfactory [21]. However, when the machining process is undergoing, chatter vibration occurs. The reason for the chatter vibration is that the frequency of the cutting force is slightly larger than the natural vibration frequency of the robot system and thus surpasses the suppression ability of the feedback controller. From Fig.26, the disturbance force F_d acts as τ_d on the actuators of the robot system through an inner inverse dynamics path. Thus, if an inverse dynamics model is introduced into the feedforward controller path which takes the disturbance F_d as the input signal the resultant extra output force from the actuator can completely cancel out the disturbance force τ_d, since the extra compensation force is also generated from the same inverse dynamic model. As a result, the vibration caused by the machining force should vanish completely.

In order to validate the effectiveness of disturbance rejection by applying an inverse dynamics based feedforward controller, a parallel manipulator is taken as a case study.

4.2 Case Study of **a** Parallel Manipulator

The parallel manipulator under study, a Cassino Parallel Manipulator (CaPaMan), is shown in Fig.27 [69]. The manipulator possesses 3 driven degrees of freedom (DOF) and consists of a mobile platform, a base and three legs. The leg consists of a parallelogram mechanism, which is driven by a servo motor in the left down-joint, and a vertical bar which can only slide perpendicular to the parallelogram plane. The up-joint of the vertical bar is a spherical joint.
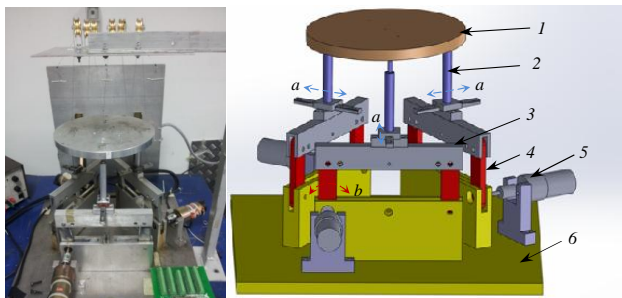
Fig.27 Prototype and 3D model of CaPaMan: 1. mobile platform 2. vertical bar 3. parallelogram mechanism 4. driven crank of parallelogram 5. servo motor 6.base a. passive freedom b. active drive
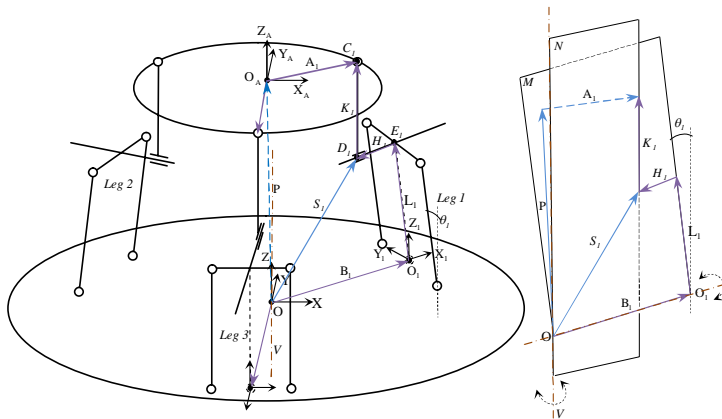
Fig.28 Kinematic scheme of CaPaMan

4.2.1 Inverse dynamic modelling of CaPaMan

In order to build up the inverse dynamics model, the kinematics should first be analyzed. In the manipulator, all the reference frames and kinematic vectors are expressed as shown in Fig.28: the global reference frame *XYZ* is located in the center of the base; the local

frame $X_A Y_A Z_A$ is fixed in the center of the mobile platform; the base joint frame $X_i Y_i Z_i$ is fixed in the middle of the bottom line of a parallelogram with the *x*-axis perpendicular to the parallelogram plane and the *z*-axis vertical to the base; P represents the vector from point O to O_A; B_1 the vector from O to O_1; L_1 the vector from O_1 to E_1 (E_1 is the middle point of the up line of the parallelogram); H_1 the vector from E_1 to D_1; K_1 the vector from D_1 to C_1 (D_1, C_1: two ends of a vertical bar); A_1 the vector from O_A to C_1; and S_1 the vector from O to D_1.

A. Kinematic constraints

Since the configuration of the 3 legs in the CaPaMan is homogenous, analysis of one of them is sufficient to deduce the kinematic constraints. From leg 1 in Fig.28, the close loop kinematic equation is obtained as Eq.61:

$$S_1 = P + A_1 - K_1 . \tag{61}$$

As the vertical bar K_1 is always vertical to the base plane (*X-Y* plane), we assume there is a virtual axis V through the point O vertically, and a plane N (in the right part of Fig.28) is formed by this virtual axis V and K_1, which can only rotate around V. As the vector H_1 is always parallel to the vector B_1, the plane M is formed, which can only rotate around B_1. The vector S_1 is the intersection of plane M and plane N.

Regardless of the rotation of plane M, the projections of vector S_1 on the Y_1 and Z_1 axes of frame $X_1 Y_1 Z_1$ are always equal to the those of vector L_1 individually. The following constraint equations are thus obtained:

$$^{R_1}S_1(2) - {}^{R_1}L_1(2) = 0 , \tag{62}$$

$$^{R_1}S_1(3) - {}^{R_1}L_1(3) = 0 , \tag{63}$$

where the leading superscript R_1 denotes that the vector is expressed in the reference frame $X_1 Y_1 Z_1$; the '2' in parentheses denotes the projection on the Y_1 axis; and the '3' the projection on the Z_1 axis.

By analogy, the following equations are obtained from leg 2 and leg 3:

$$^{R_2}S_2(2) - {}^{R_2}L_2(2) = 0 , \tag{64}$$

$$^{R_2}S_2(3) - {}^{R_2}L_2(3) = 0 , \tag{65}$$

$$^{R_3}S_3(2) - {}^{R_3}L_3(2) = 0 , \tag{66}$$

$$^{R_3}S_3(3) - {}^{R_3}L_3(3) = 0. \tag{67}$$

Let the left parts of Eq. (62) to Eq. (67) be represented by C_1 to C_6 individually. Since they are functions of the mobile platform coordinates (P_x, P_y, P_z, a, b, c) and the rotation angles of the parallelogram $\theta_1, \theta_2, \theta_3$, taking the partial derivatives of these constraint functions C_i with respect to the 9 generalized coordinates yields:

$$
\begin{bmatrix}
\frac{\partial C_1}{\partial P_x} & \frac{\partial C_1}{\partial P_y} & \frac{\partial C_1}{\partial P_z} & \frac{\partial C_1}{\partial a} & \frac{\partial C_1}{\partial b} & \frac{\partial C_1}{\partial c} & \vdots & \frac{\partial C_1}{\partial \theta_1} & \frac{\partial C_1}{\partial \theta_2} & \frac{\partial C_1}{\partial \theta_3} \\
\frac{\partial C_2}{\partial P_x} & \frac{\partial C_2}{\partial P_y} & \frac{\partial C_2}{\partial P_z} & \frac{\partial C_2}{\partial a} & \frac{\partial C_2}{\partial b} & \frac{\partial C_2}{\partial c} & \vdots & \frac{\partial C_2}{\partial \theta_1} & \frac{\partial C_2}{\partial \theta_2} & \frac{\partial C_2}{\partial \theta_3} \\
\frac{\partial C_3}{\partial P_x} & \frac{\partial C_3}{\partial P_y} & \frac{\partial C_3}{\partial P_z} & \frac{\partial C_3}{\partial a} & \frac{\partial C_3}{\partial b} & \frac{\partial C_3}{\partial c} & \vdots & \frac{\partial C_3}{\partial \theta_1} & \frac{\partial C_3}{\partial \theta_2} & \frac{\partial C_3}{\partial \theta_3} \\
\frac{\partial C_4}{\partial P_x} & \frac{\partial C_4}{\partial P_y} & \frac{\partial C_4}{\partial P_z} & \frac{\partial C_4}{\partial a} & \frac{\partial C_4}{\partial b} & \frac{\partial C_4}{\partial c} & \vdots & \frac{\partial C_4}{\partial \theta_1} & \frac{\partial C_4}{\partial \theta_2} & \frac{\partial C_4}{\partial \theta_3} \\
\frac{\partial C_5}{\partial P_x} & \frac{\partial C_5}{\partial P_y} & \frac{\partial C_5}{\partial P_z} & \frac{\partial C_5}{\partial a} & \frac{\partial C_5}{\partial b} & \frac{\partial C_5}{\partial c} & \vdots & \frac{\partial C_5}{\partial \theta_1} & \frac{\partial C_5}{\partial \theta_2} & \frac{\partial C_5}{\partial \theta_3} \\
\frac{\partial C_6}{\partial P_x} & \frac{\partial C_6}{\partial P_y} & \frac{\partial C_6}{\partial P_z} & \frac{\partial C_6}{\partial a} & \frac{\partial C_6}{\partial b} & \frac{\partial C_6}{\partial c} & \vdots & \frac{\partial C_6}{\partial \theta_1} & \frac{\partial C_6}{\partial \theta_2} & \frac{\partial C_6}{\partial \theta_3}
\end{bmatrix}
\begin{bmatrix}
\partial P_x \\ \partial P_y \\ \partial P_z \\ \partial a \\ \partial b \\ \partial c \\ \hdashline \partial \theta_1 \\ \partial \theta_2 \\ \partial \theta_3
\end{bmatrix}
=
\begin{bmatrix}
0 \\ 0 \\ 0 \\ 0 \\ 0 \\ 0 \\ 0
\end{bmatrix}
\tag{68}
$$

By matrix partition, Eq. (68) can be simplified to Eq. (69):

$$
\begin{bmatrix} C_{q_d} & C_{q_i} \end{bmatrix}
\begin{bmatrix} \partial q_d \\ \partial q_i \end{bmatrix}
= \begin{bmatrix} 0 & 0 & 0 & 0 & 0 & 0 \end{bmatrix}^T. \tag{69}
$$

B. Lagrangian formulation

By taking account of the kinetic and potential energy of the mobile platform, vertical bar and the parallelogram mechanism, a Lagrange function is obtained as in Eq. (70):

$$L = K_P + K_V + K_C - U_P - U_V - U_C, \tag{70}$$

where K_p and U_p represent the kinetic and potential energy of the mobile platform; K_v and U_v the kinetic and potential energy of the vertical bar (the slider of passive freedom included); and K_c and U_c the kinetic and potential energy of the parallelogram (slider base included).

Let the coordinates of the mobile platform be the redundant Lagrangian coordinates and the rotations of the parallelogram be the independent coordinates, then 6 Lagrangian multipliers are introduced as expressed in Eq. (71):

$$\lambda = \begin{bmatrix} \lambda_1 & \lambda_2 & \lambda_3 & \lambda_4 & \lambda_5 & \lambda_6 \end{bmatrix}^T. \tag{71}$$

If the first 6 Lagrangian equations of the first type are associated with the mobile platform coordinates, then a set of system dynamic equations can be written in the form:

$$C_{q_d}{}^T \lambda = \frac{d}{dt}\left(\frac{\partial L}{\partial \dot{Q}_d}\right) - \frac{\partial L}{\partial Q_d} - F_d, \tag{72}$$

where

$$\frac{d}{dt}\left(\frac{\partial L}{\partial \dot{Q}_d}\right) = \left[\frac{d}{dt}\left(\frac{\partial L}{\partial \dot{P}_x}\right) \quad \frac{d}{dt}\left(\frac{\partial L}{\partial \dot{P}_y}\right) \quad \frac{d}{dt}\left(\frac{\partial L}{\partial \dot{P}_z}\right) \quad \frac{d}{dt}\left(\frac{\partial L}{\partial \dot{a}}\right) \quad \frac{d}{dt}\left(\frac{\partial L}{\partial \dot{b}}\right) \quad \frac{d}{dt}\left(\frac{\partial L}{\partial \dot{c}}\right)\right]^T,$$

$$\frac{\partial L}{\partial Q_d} = \left[\frac{\partial L}{\partial P_x} \quad \frac{\partial L}{\partial P_y} \quad \frac{\partial L}{\partial P_z} \quad \frac{\partial L}{\partial a} \quad \frac{\partial L}{\partial b} \quad \frac{\partial L}{\partial c}\right]^T, \text{ and } F_d = \begin{bmatrix} f_x & f_y & f_z & \tau_x & \tau_y & \tau_z \end{bmatrix}^T, \text{ which}$$

represents the external force acting on the mobile platform. When the position, velocity and acceleration of the mobile platform and the external forces are given, the values of the Lagrangian multipliers can be computed by solving the linear equations described by Eq. (72).

Once the Lagrangian multipliers are found, the actuator torques in the driving joints of the legs can be determined directly from the remaining Lagrangian equations. Specifically, the second set of 3 Lagrangian equations for the system dynamics can be written in the form:

$$F_i = \frac{d}{dt}\left(\frac{\partial L}{\partial \dot{Q}_i}\right) - \frac{\partial L}{\partial Q_i} - C_{q_i}{}^T \lambda, \tag{73}$$

where $\dfrac{d}{dt}\left(\dfrac{\partial L}{\partial \dot{Q}_i}\right) = \left[\dfrac{d}{dt}\left(\dfrac{\partial L}{\partial \dot{\theta}_1}\right) \quad \dfrac{d}{dt}\left(\dfrac{\partial L}{\partial \dot{\theta}_2}\right) \quad \dfrac{d}{dt}\left(\dfrac{\partial L}{\partial \dot{\theta}_3}\right)\right]^T$, $\dfrac{\partial L}{\partial Q_i} = \left[\dfrac{\partial L}{\partial \theta_1} \quad \dfrac{\partial L}{\partial \theta_2} \quad \dfrac{\partial L}{\partial \theta_3}\right]^T$, and

$F_i = \begin{bmatrix} \tau_1 & \tau_2 & \tau_3 \end{bmatrix}^T$, which are the actuator torques needed from the servo motor.

4.2.2 Vibration control of CaPaMan

Fig.29 shows the control scheme applied in CaPaMan. The entire control strategy of CaPaMan, as well as the forward dynamics behavior, are simulated in a software environment, in which the control algorithms are implemented in MATLAB Simulink and the forward dynamics behavior is computed and presented by ADAMS solver/viewer.
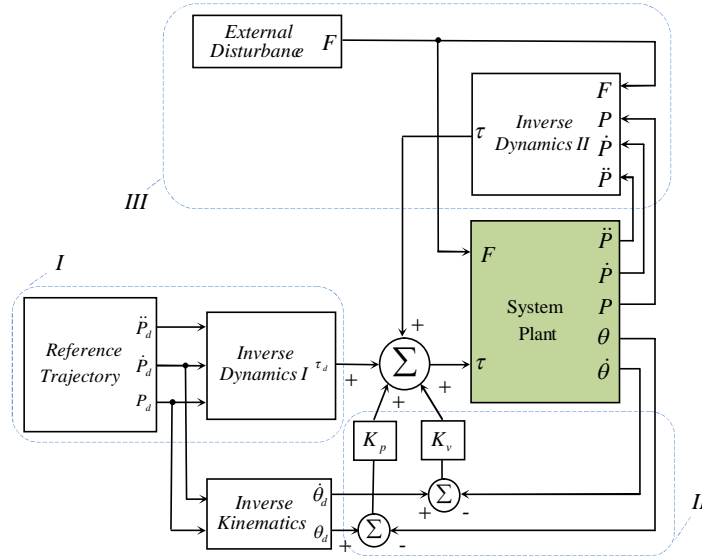
Fig.29 Control scheme: I. Feedforward model-based nonlinear control, II. Feedback PV control, III. Feedforward disturbance depressing control

The control scheme for this parallel manipulator consists of three parts, as shown in Fig.29: I. Feedforward model-based nonlinear control, II. Feedback PV control, and III. Feedforward external disturbance rejection control.

Due to the highly non-linear behavior of the dynamics in the parallel manipulator, it is difficult to get satisfactory tracking performance, even without external disturbance, using only a conventional PID controller with constant gains. Therefore, the model-based feedforward and the feedback PV control are combined to relatively simplify the nonlinearity of the control system so as to get a satisfactory tracking error, and the feedforward disturbance rejection control is used to depress the effect from the external disturbance force.

A. Model-based feedforward nonlinear control

For general rigid body dynamics, a universal form can be given as Eq. (74):

$$\tau = M(\Theta)\ddot{\Theta} + V(\Theta,\dot{\Theta}) + G(\Theta) + F(\Theta,\dot{\Theta}), \tag{74}$$

where M is the $n \times n$ inertial matrix of the manipulator; V an $n \times 1$ vector of the centrifugal and Coriolis terms; G an $n \times 1$ vector of gravity; and F the friction of the joints and external load.

77

By utilizing the linearizing and decoupling control law, the non-linear control term $V(\Theta,\dot{\Theta}) + G(\Theta) + F(\Theta,\dot{\Theta})$ can be taken into the control system to cancel out the nonlinearity in the dynamics model, which yields a linear second order system, $f = M(\Theta)\ddot{\Theta}$, and an error model of the control system, $\ddot{E} + K_v\dot{E} + K_pE = 0$.

However for a parallel mechanism, due to nonlinear kinematics coupling of actuated joints, it is impossible to separate the term M from its dynamics model, and therefore the above-mentioned linearizing law is not valid. To address this issue, a revised model-based control is employed for CaPaMan control, which consists of two parts, I. Feedforward and II. Feedback, as shown in Fig.29. If only part I and part II of the control scheme are taken into consideration, the system equation can be written in the form:

$$M(\Theta_d)\ddot{\Theta}_d + V(\Theta_d,\dot{\Theta}_d) + G(\Theta_d) + F(\Theta_d,\dot{\Theta}_d) + K_v\dot{E} + K_pE$$
$$= M(\Theta)\ddot{\Theta} + V(\Theta,\dot{\Theta}) + G(\Theta) + F(\Theta,\dot{\Theta}) \tag{75}$$

where $E = \Theta_d - \Theta$. By simplifying Eq. (75) under the assumptions, $M(\Theta_d) \cong M(\Theta)$, $V(\Theta_d,\dot{\Theta}_d) \cong V(\Theta,\dot{\Theta})$, $G(\Theta_d) \cong G(\Theta)$ and $F(\Theta_d,\dot{\Theta}_d) \cong F(\Theta,\dot{\Theta})$, the error equations of the system are found as:

$$\ddot{E} + M^{-1}(\Theta)K_v\dot{E} + M^{-1}(\Theta)K_pE = 0. \tag{76}$$

Clearly, the feedforward control does not provide complete nonlinearity decoupling, and the effective feedback gain changes as the configuration of the parallel manipulator changes. However a good set of constant gains can still be found to guarantee a reasonable damping performance [21].

B. Disturbance suppression by feedforward control

When the parallel manipulator is used in a machining task, the cutting force F_c is deemed to be a varying disturbance. By applying the feedforward control loop (control part III in Fig.29), compensation torque, which is used to cancel out the effect of F_c through the manipulator, is computed based on the constructed inverse dynamics model. The complete function diagram of the control scheme applied in CaPaMan is presented in Fig. 30.
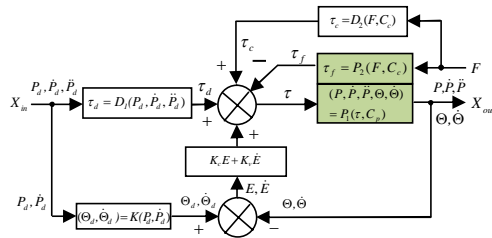
Fig.30 Implementation of the control system for CaPaMan

The control system consists of two parts: (1) in the part of P_1, the torques acting on the driving joints are taken as the input parameters of the system function, while the position, velocity, and acceleration of the mobile platform as well as the driving joints are regarded as outputs. The part of P_1 can be expressed by Eq. (77):

$$(P,\dot{P},\ddot{P},\Theta,\dot{\Theta}) = P_1(\tau,C_p), \tag{77}$$

where C_p is the configuration of the manipulator from the previous computation step, P and Θ represent the position vectors of mobile platform and joints; (2) in the part of P_2, the external load F is taken as the input parameter, while the resultant effective torque τ_f in the driving joints is taken as the output of the system, which is expressed by Eq. (78):

$$\tau_f = P_2(F,C_c), \tag{78}$$

where C_c is the current manipulator configuration.

The actual acting torque on the driving joints are formed by Eq. (79) as follows:

$$\tau = \tau_d + K_c E + K_v \dot{E} + (\tau_c - \tau_f), \tag{79}$$

where $\tau_d = D_1(P_d,\dot{P}_d,\ddot{P}_d)$ is the torque computed from the reference trajectory, $K_c E + K_v \dot{E}$ is the torque computed from the trajectory control error, and $\tau_c = D_2(F,C_c)$ is the torque used for compensation of the external force. Substituting Eq. (79) into Eq. (77) yields:

$$(P,\dot{P},\ddot{P},\Theta,\dot{\Theta}) = P_1((D_1 + K_c E + K_v \dot{E} + (D_2 - P_2)),C_p). \tag{80}$$

From Eq. (80), when the established inverse dynamics model D_2 of the parallel manipulator in the control system approximates to P_2 in the real system, the difference between the compensation torque and the disturbing torque in the driving joints approaches zero. Consequently, the effect of the external load is eliminated significantly, or even completely, and the whole plant system is reduced to plant P_1, which is described by Eq. (77) and can be easily controlled by the combination of the model-based nonlinear control strategy and the feedback PV controller.

C. Results based on feedforward disturbance rejection control

Results for disturbance suppression based on the proposed control strategy are presented in this section for a reference trajectory of the mobile platform, which is shown in Fig.31.
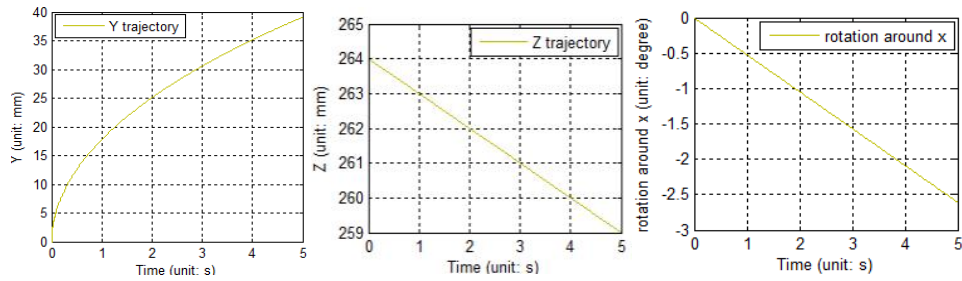
Fig.31 Reference trajectory of mobile platform

In the given reference trajectory, the freedoms of the mobile platform consist of translations along the y- and z-axes, and rotation around the x-axis.

The external disturbance force is a 10 Hz triangle wave with an amplitude of 20 N, as shown in Fig.32.
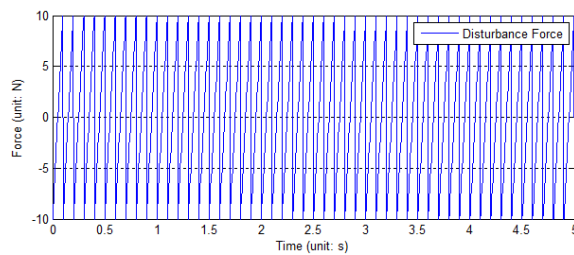
Fig.32 External disturbance force of 10 Hz

When the feedforward model-based control is applied, with/without the feedforward control path for disturbance depression (FDD) in the control system, the outputs of the obtained trajectories are as shown in Fig.33.
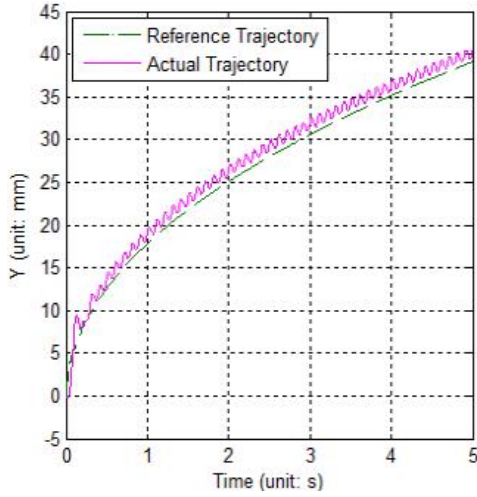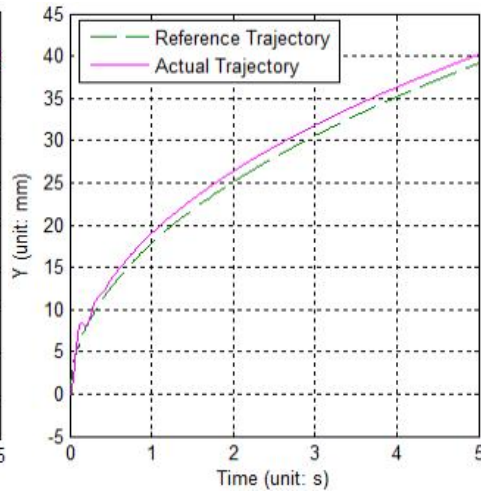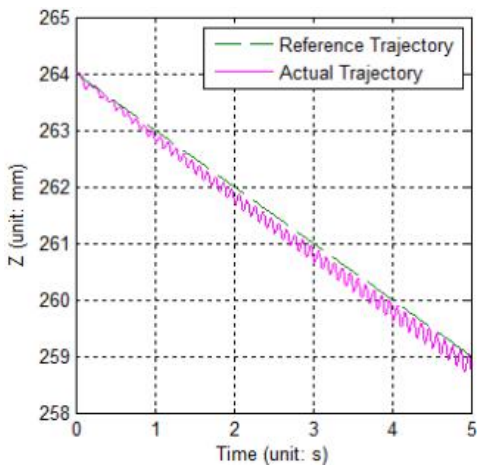
(a) Y-trajectory without FDD   (b) Y-trajectory with FDD

(c) Z-trajectory without FDD (b) Z-trajectory with FDD
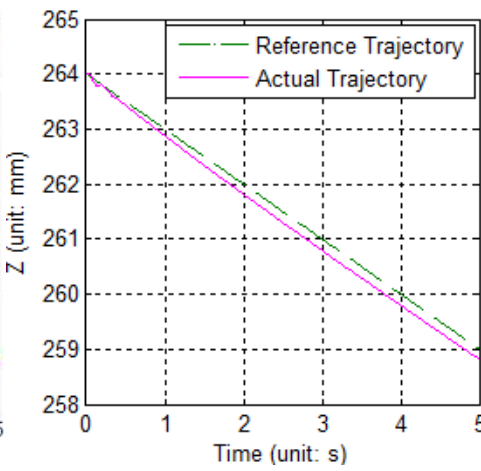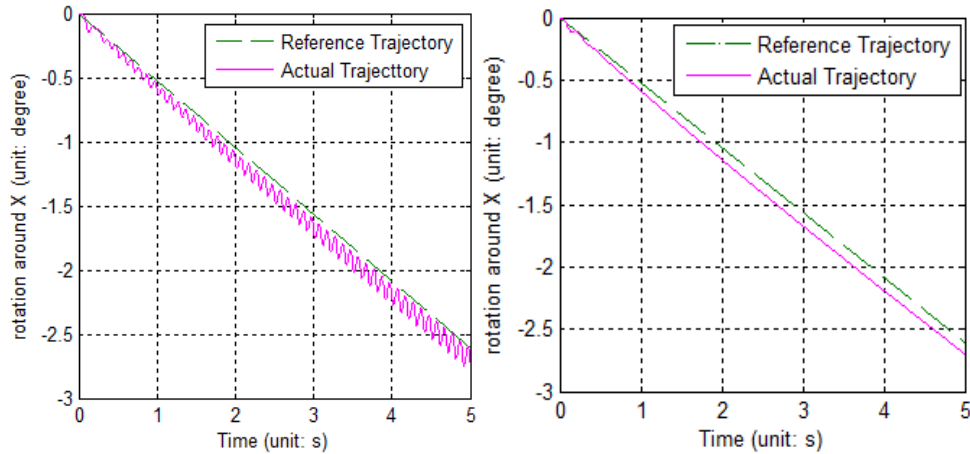
(e) AX-rotation without FDD (f) AX-rotation with FDD

Fig.33 Comparison of trajectory outputs with and without the feedforward control path for external disturbance supression under feedforward model-based control

In the figures, the dashed blue line represents the reference trajectory and the continuous red line represents the actual obtained trajectory. From Fig. 33 (a), (c) and (e), it is clearly seen that the chatter vibrations occurred in the same frequency as the external disturbance. However, the results shown in Fig.33 (b), (d) and (f), suggest two outcomes: (1) the feedforward control for external disturbance suppression applied based on the constructed inverse dynamics model of the target manipulator is validated to be very effective; (2) using the feedforward model-based control enables a stable trajectory tracking error to be obtained for the highly nonlinear dynamic system.

Although software simulation of CaPaMan gives a good result, several difficulties still remain as regards practical application of this method of vibration suppression. In the example above, the friction force in the joints of CaPaMan are ignored in both the ADAMS model and the constructed inverse dynamics model. However, in practice, the friction model has to be taken into account due to the slow motion and the heavy payload when the robotic machine is carrying out the machining task. In addition, dynamic parameters of CaPaMan such as the inertial matrix are assumed to be ideal in the simulation process, but in practice, these parameters have to be identified.

For a parallel robot, the kinematics chains are coupled with one another, which renders direct measurement of the friction models in the joints, as well as measurement of the dynamics parameters difficult, and thus, an indirect identification method has to be developed to identify these unknown dynamics.

4.3 Dynamics Model Identification

In mechanical engineering applications, an accurate dynamic model for the target system can be very beneficial to the control system design [59]-[62]. In some control systems demanding high performance, such as systems with a requirement for high precision position control under varying payload, industrial robots requiring accurate force control or robotic systems requiring dynamic predictive control, the accurate dynamic model of the system is incorporated into the system controller design to satisfy the performance requirement [63]-[65]. For vibration suppression of a robotic machine, incorporating an accurate inverse dynamic model into a feedforward controller has been shown to be a very efficient way to eliminate end-effector chatter [66][67].

In practice, especially in a parallel structure based mechanism, due to the complexity of the multi-body dynamics and the difficulty in modeling certain components of the dynamic system, it is either unrealistic or inaccurate to construct an analytical dynamic model that can exactly match the actual dynamic behavior of the target system. Sometimes the theory itself required for modelling some components of the system dynamics from physical insight is either still under development or inapplicable for a specific application. For instance, in mechanical systems, various friction theories and modeling methods exist for different working conditions; in parallel robot joints, the friction forces are coupled with each other and have highly nonlinear, highly correlated and time-variant characteristics, which render it even more difficult to build up the individual theoretical model; and in a hydraulic system, accurately modelling the dynamics between a cylinder and a valve also presents some difficulties, such as internal valve leakage modeling, and friction and damping parameter identification. In some cases, a constructed dynamic model of the mechanical system becomes inaccurate, because the system parameters change – a variance which occurs in terms of perturbation of the inertial matrix, changing of the friction coefficient etc, due to wear and deformation in the mechanism assembly. Under such circumstances, direct measurement of these dynamic parameters is not feasible.

However, abundant input-output data can be obtained by carrying out experiments on the target dynamic system, and the acquired data set may cover various deterministic trajectories and working domains of the dynamic system. Therefore, discussion of dynamics modelling will focus on how to identify an approximate dynamic model based on experimental data. During the past decades, artificial neural networks (ANN) have been widely studied and employed for dynamic model identification of linear and nonlinear systems.

To date, artificial neural networks have proven to be a very efficient tool for parameter identification and model approximation, given that a prior measured input-output data set of the target dynamic system is available. Several ANN types such as the multilayer

perceptron (MLP) neural network [55], radial basis function neural network (RBFNN) [56] and functional link artificial neural network (ALANN) [57] have been subject to intensive research and have been applied successfully in dynamic model identification. All these ANN methods are primarily designed for approximating the target system as a whole entity, and with all the methods the prior input-output data set of the target dynamical system must be measurable and have been obtained in advance. However, in most practical cases, only some small amount of the unknown components of the whole dynamic system need to be identified, and direct measurement of the required input-output data of such unknown components is not feasible. Consequently, the above-mentioned ANNs are not suitable for indentifying these unknown components of the dynamic system.

This dissertation proposes a method for indentifying unknown components or subsystems of the whole dynamic system via a BP neural network using a prior measured data set from the whole system. In order to utilize such measured input-output data to train the ANN models for the unknown components, a modified Levenberg-Marquardt (LM) algorithm is proposed and developed in the dissertation. Although the original LM algorithm is regarded as a most efficient training algorithm for BP neural networks, it is effective only when a prior measured training data set of the system under modelling is available [58]. In the dissertation, it is assumed that some components or a subsystem of the whole dynamic system need to be identified, and that only the input-output data set of the whole dynamic system is measurable and available, which thereby is regarded as an indirect training data set for the unknown components or subsystem of the entire dynamics. Thus, the original LM algorithm needs to be modified to fit into such indirect data. In the modified LM algorithm, the derivatives of the output data set of the whole system with respect to the outputs of the neural network are deduced, and thereafter such derivative information is incorporated into the Jacobian matrix of the neural network, and a new Jacobian matrix is formed by chain rule that can represent the relationship between the errors of the whole system output and the weights of the neural network. The prior measured input-output data of the whole dynamic system is thus used to train the neural network for the unknown components of the dynamic system.

4.3.1 Dynamics identification by neural network using indirect error

For model identification of a dynamic system by a BP neural network, the most common approach is to use the neural network to approximate the outputs of the entire target system over the domain of interest based on prior obtained input-output data sets, as shown in Fig.34.
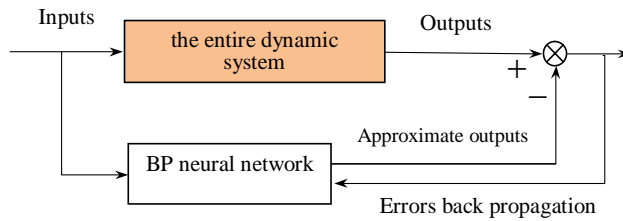
Fig.34 Neural network as a dynamic model approximator

However, when the domain of interest of the target dynamic system spans a large area and the dynamic system contains many parameters and is highly nonlinear and time variant, the approximation of the neural network is neither efficient, nor its accuracy satisfactory.

Nevertheless, for any dynamic system, some knowledge of most components of the dynamics should be available, and only small components or subsystems of the dynamics of the system exist as a 'black box' or an incomplete function. In such cases, the neural network should be used to approximate these unknown components rather than the entire dynamics. The well trained neural network for these unknown dynamical components can then be incorporated into the entire dynamic system to substitute the unknown components. The scheme of this concept is shown in Fig 35.
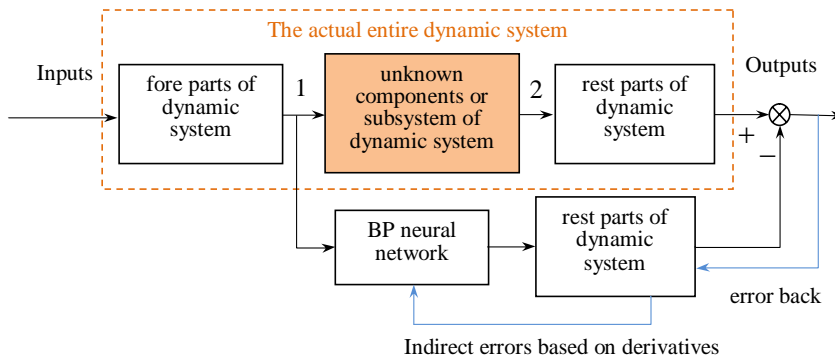
a) Identification/training process for unknown components: 1. Inputs of the unknown components of the dynamics; 2. The outputs of the unknown components
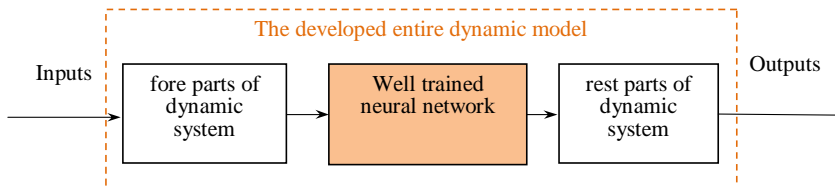
b) Identified model and the entire developed dynamics

Fig.35 Neural network as an approximator for part of a dynamic system

Practically, the unknown components of the dynamics shown in Fig. 35 (a) are embedded into the entire system and coupled with the systems fore and aft. It is difficult to obtain the prior input-output data set for such an unknown system. However, the inputs can be obtained from the inputs of the entire system via its fore part system. The outputs of such an unknown system are regarded as immeasurable and cannot be computed from the outputs of the entire system due to the difficulty of implementing the inverse computation of the other components of the dynamics as in Fig. 35 (a).

From the entire system dynamics point of view, if the BP neural network for the unknown components in Fig. 35 (a) are well trained, the errors between the outputs of the constructed entire dynamic model (Fig. 35 (b)) and the practical entire dynamic system (Fig. 35 (a)) should approach zero. Since outputs measurement of the entire dynamic system is feasible, it can be used to train the neural network for the unknown components of the dynamics based on a modified LM algorithm that utilizes a chain rule to propagate the errors from the entire system output to the weights of the neural network. The Jacobian matrix in the chain rule in the modified LM, which consists of derivatives of the outputs of the entire system with respect to the weights of the neural network, can be easily computed discretely using data recording from both the outputs of the neural network and the practical entire system along with the intrinsic mathematics of the neural network. Thus, a rule for updating the weights of the neural network can be deduced by using the outputs data set of the entire system. In the dissertation, such measurable data from the practical entire system is therefore named indirect training data for the unknown components of the dynamics, and the training process is named indirect error propagation.

4.3.2 Modified Levenberg-Marquardt algorithm for neural network training

Since the modified LM algorithm is deduced based on the original LM algorithm, it is necessary to introduce briefly the original algorithm.

A. Levenberg-Marquardt training algorithm

The original LM algorithm for training neutral networks evolved from the Gauss-Newton algorithm. The LM algorithm inherits the speed advantage of the Gauss-Newton algorithm, while also gaining advantage from adoption of convergence from the steepest descent whenever the error in the training process tends to divergence [58][72].

The training process for a neural network can be represented by Eq. (81):

$$W_{k+1} = W_k - H_k^{-1} J_k^{T} E_k , \qquad (81)$$

where, the subscripts k and $k+1$ indicate the current iteration and next iteration; W_k and W_{k+1} represent the weight vectors consisting of all the individual weights of the neural network; H_k is the Hessian matrix, which is a square matrix of second order partial derivatives of the neural network output errors with respect to the weights; J_k is the Jacobian matrix of the errors of the neural network outputs with respect to the weights of the neural network; and E_k is the error vector consisting of errors of outputs between the target system and neural network.

The Jacobian matrix J_k and the error vector E_k are represented by Eq. (82) and Eq. (83) respectively:

$$J_k = \begin{bmatrix} \dfrac{\partial e_1}{\partial w_1} & \dfrac{\partial e_1}{\partial w_2} & \cdots & \dfrac{\partial e_1}{\partial w_i} \\ \dfrac{\partial e_2}{\partial w_1} & \dfrac{\partial e_2}{\partial w_2} & \cdots & \dfrac{\partial e_2}{\partial w_i} \\ \vdots & \vdots & & \vdots \\ \dfrac{\partial e_n}{\partial w_1} & \dfrac{\partial e_n}{\partial w_2} & \cdots & \dfrac{\partial e_n}{\partial w_i} \end{bmatrix}_{n \times i} , \tag{82}$$

$$E_k = Y_k^t - Y_k = \begin{bmatrix} e_1 & e_2 & \cdots & e_n \end{bmatrix}_k^T , \tag{83}$$

where, e_i represents the error between the ith output of the target system and neural network; w_i is the ith weight of the neural network; Y_k^t is the output vector of the target system; and Y_k is the output vector of the neural network.

In order to avoid computation of second order partial derivatives, the Hessian matrix is approximated in the Levenberg-Marquardt algorithm by Eq. (84):

$$H_k = J_k^T J_k + \mu I , \tag{84}$$

where μ is always positive and called the combination coefficient; and I is the identity matrix and introduced to guarantee that the approximated Hessian matrix is always invertible.

Substituting Eq. (84) into Eq. (81) yields:

$$W_{k+1} = W_k - (J_k^T J_k + \mu I)^{-1} J_k^T E_k , \tag{85}$$

which represents the weights updating rule in each training iteration of the LM algorithm. When the combination coefficient μ is very small, the Gauss-Newton algorithm dominates Eq. (85), which gives the advantage of speed; when the updating error

increases, then the combination coefficient μ increases, and the steepest descent method starts to dominate Eq. (85), which can guarantee the correct convergence direction of the training.

B. Modified training algorithm

In Eq. (85), the error is computed from the difference between the outputs of the target system and the neural network. However, when the target system is a part of a larger system, and the outputs of the target system are not measurable directly, as shown in Fig. 36, and the direct error of the neural network training cannot be obtained, the Jacobian matrix in Eq.(85) cannot be computed and the LM algorithm is not applicable.
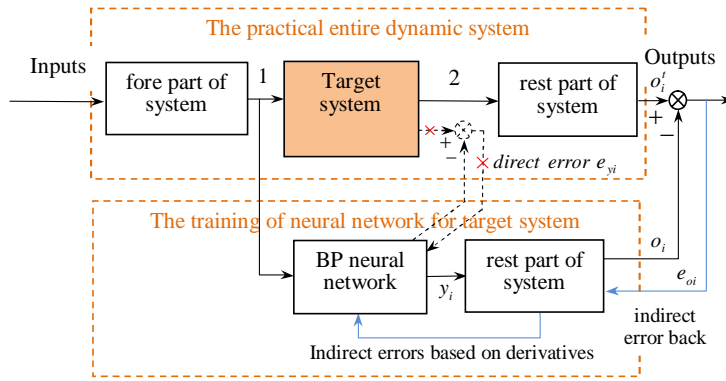
Fig.36 Neural network training by indirect error propagation: 1. Input of the target system; 2. Output of the target system (immeasurable)

However, the output data from the entire dynamic system are still useful to train the neural network by a modified LM algorithm. In order to utilize the modified LM algorithm on the output data of the entire system, a new Jacobian matrix and a new Hessian matrix need to be deduced that can present the partial derivatives of the entire system output errors with respect to the weights of the neural network. The following notions are used throughout this section:

o_i^t : the ith output of the practical entire dynamic system;

o_i : the ith output of the constructed dynamic model;

e_{oi} : the ith error between the practical entire dynamic system and the constructed dynamic model, $e_{oi} = o_i^t - o_i$;

E_{o_k} : the error vector consisting of all the errors e_{oi} in the kth iteration;

y_i : the ith output of the neural network;

w_i : the ith weight of the neural network;

M_k : the partial derivatives of the entire dynamics system output errors with respect to the outputs of the neural network in the kth iteration, which is represented by Eq. (86):

$$M_k = \begin{bmatrix} \dfrac{\partial(o_1^t - o_1)}{\partial y_1} & \dfrac{\partial(o_1^t - o_1)}{\partial y_2} & \cdots & \dfrac{\partial(o_1^t - o_1)}{\partial y_n} \\ \dfrac{\partial(o_2^t - o_2)}{\partial y_1} & \dfrac{\partial(o_2^t - o_2)}{\partial y_2} & \cdots & \dfrac{\partial(o_2^t - o_2)}{\partial y_n} \\ \vdots & \vdots & & \vdots \\ \dfrac{\partial(o_m^t - o_m)}{\partial y_1} & \dfrac{\partial(o_m^t - o_m)}{\partial y_2} & \cdots & \dfrac{\partial(o_m^t - o_m)}{\partial y_n} \end{bmatrix}_{m \times n} = - \begin{bmatrix} \dfrac{\partial o_1}{\partial y_1} & \dfrac{\partial o_1}{\partial y_2} & \cdots & \dfrac{\partial o_1}{\partial y_n} \\ \dfrac{\partial o_2}{\partial y_1} & \dfrac{\partial o_2}{\partial y_2} & \cdots & \dfrac{\partial o_2}{\partial y_n} \\ \vdots & \vdots & & \vdots \\ \dfrac{\partial o_m}{\partial y_1} & \dfrac{o_m}{\partial y_2} & \cdots & \dfrac{\partial o_m}{\partial y_n} \end{bmatrix}_{m \times n} \quad ;(86)$$

J_{Y_k} : the Jacobian matrix between the outputs of the neural network and the weights in the kth iteration, which is represented by Eq. (87):

$$J_{Y_k} = \begin{bmatrix} \dfrac{\partial y_1}{\partial w_1} & \dfrac{\partial y_1}{\partial w_2} & \cdots & \dfrac{\partial y_1}{\partial w_i} \\ \dfrac{\partial y_2}{\partial w_1} & \dfrac{\partial y_2}{\partial w_2} & \cdots & \dfrac{\partial y_2}{\partial w_i} \\ \vdots & \vdots & & \vdots \\ \dfrac{\partial y_n}{\partial w_1} & \dfrac{\partial y_n}{\partial w_2} & \cdots & \dfrac{\partial y_n}{\partial w_i} \end{bmatrix}_{n \times i} \quad ; \tag{87}$$

The updating rule for the weights of the neural network based on the modified LM algorithm can therefore be represented by Eq. (88):

$$W_{k+1} = W_k - (J_{o_k}^{\ T} J_{o_k} + \mu I)^{-1} J_{o_k}^{\ T} E_{o_k} , \tag{88}$$

where J_{o_k} is the new Jacobian matrix of the errors of the entire system outputs with respect to the weights of the neural network, which is deduced by applying the chain rule on Eq. (86) and Eq. (87), and represented by Eq.(89):

$$J_{o_k} = -\begin{bmatrix} \dfrac{\partial o_1}{\partial w_1} & \dfrac{\partial o_1}{\partial w_2} & \cdots & \dfrac{\partial o_1}{\partial w_i} \\ \dfrac{\partial o_2}{\partial w_1} & \dfrac{\partial o_2}{\partial w_2} & \cdots & \dfrac{\partial o_2}{\partial w_i} \\ \vdots & \vdots & & \vdots \\ \dfrac{\partial o_m}{\partial w_1} & \dfrac{\partial o_m}{\partial w_2} & \cdots & \dfrac{\partial o_m}{\partial w_i} \end{bmatrix}_{m \times i} = M_k J_{Y_k}. \tag{89}$$

The partial derivative matrix M_k is computed discretely from the data recording of both the outputs of the neural network and the entire dynamic system, when the analytical derivatives of the outputs of the other parts of the system (Fig. 35) with respect to its inputs are not applicable. Notice that the Jacobian matrix J_{Y_k} herein differs from the Jacobian matrix J_k in the original LM algorithm, in that J_{Y_k} is the derivatives of outputs of the neural network with respect to the weights, but J_k in the original LM algorithm is the derivatives of the errors of the outputs of the neural network with respect to the weights.

For batch training of the modified LM algorithm, an updating rule for the weights can be obtained by augmenting the error vector E_{o_k} and Jacobian matrix J_{o_k} in Eq. (88) in the column direction respectively, as in Eq. (90):

$$W_{k+1} = W_k - (J_{B_k}{}^T J_{B_k} + \mu I)^{-1} J_{B_k}{}^T E_{B_k}, \tag{90}$$

where E_{B_k} and J_{B_k} represent the corresponding augmented error vector and Jacobian matrix for the batch training;

$$E_{B_k} = \begin{bmatrix} {}^1 E_{o_k}^T & {}^2 E_{o_k}^T & \cdots & {}^p E_{o_k}^T \end{bmatrix}^T; \tag{91}$$

$$J_{B_k} = \begin{bmatrix} {}^1 J_{o_k}^T & {}^2 J_{o_k}^T & \cdots & {}^p J_{o_k}^T \end{bmatrix}^T, \tag{92}$$

and the superscript p indicates the index of patterns or data samples in the batch data.

4.3.3 Case study

Validation of the method proposed in the dissertation is performed by a sinusoidal output approximation, a second order system parameters estimation and a friction model estimation of a parallel structure based manipulator, which respectively represent three different applications of this method.

A. Sinusoidal function approximation

For a general validation of the proposed method from the perspective of system approximation, a system with an unknown part is employed and regarded as an entire system for the approximation by incorporation of the neural network, as shown in Fig.37.
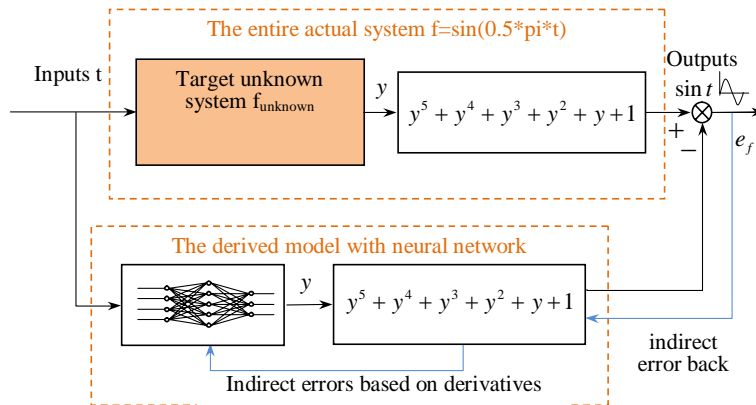
Fig.37 Sinusoidal function approximation of a partially known system

It is assumed that the entire system takes a continuous time sequence as the input and yields a sinusoidal signal $f=sin(0.5*pi*t)$ as the output. The known part of the entire system is a 5th order polynomial function, which makes the inverse computation from the output of entire system to the output of neural network have multiple solutions. Thus, obtaining direct training data for the target unknown system is not practical.

By applying the modified LM algorithm on the entire system input-output data set, a neural network model for the unknown part can be identified and incorporated into the derived model for the entire system approximation. The input and output signals of the entire actual system, which are used for the neural network training, are shown in Fig.38.
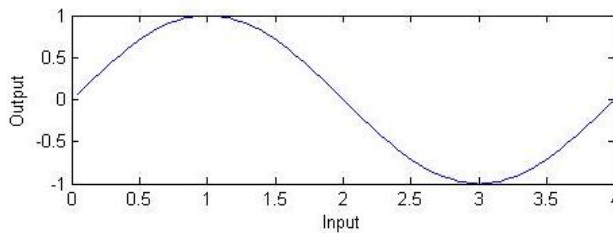
Fig.38 Input and output signal for the entire real system

The input signal is a continuous time sequence from 0 to 4, and the output is a sinusoidal function $f=sin(0.5*pi*t)$, whose amplitude equals 1 and period equals 4.

A single hidden layer neural network with 10 neurons is adopted for the unknown part system identification, and 100 input-output data samples are utilized for neural network batch training in each iteration. The identification results are shown in Fig. 39 and Fig. 40.
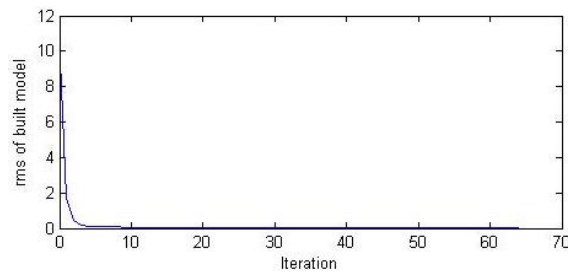
Fig.39 Root mean square (RMS) of errors between the actual and derived system during the neural network training process
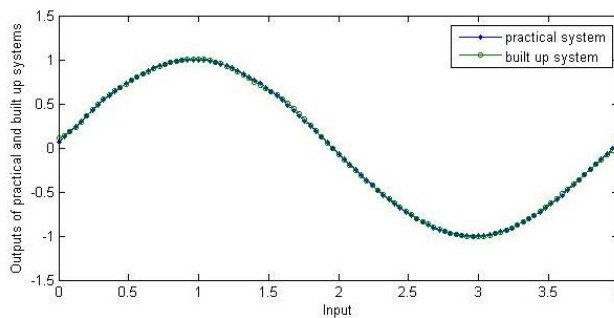
Fig.40 Comparison between the actual and derived system at the 100th iteration of the training process

Since the neural network is trained based on a batch of samples in every iteration, the root mean square of errors in Fig. 39 is also computed based on the data set of the batch outputs in every iteration. In Fig. 39, the training process of the neural network converges very fast at the beginning of the training, after which the error between the real system and constructed model starts to become stable after around 10 training iterations. The stable root mean square error of the batch training data is around 1.0e-3 after 100 iterations.

For validation of the constructed model, 200 random data samples spanning from 0-4 were inputted into the real system, which yielded the outputs as the sinusoidal function $f= sin(0.5*pi*t)$ of the input. At the same time, the same random samples were inputted into the constructed model. A comparison between the results for the two systems is shown in Fig. 41.
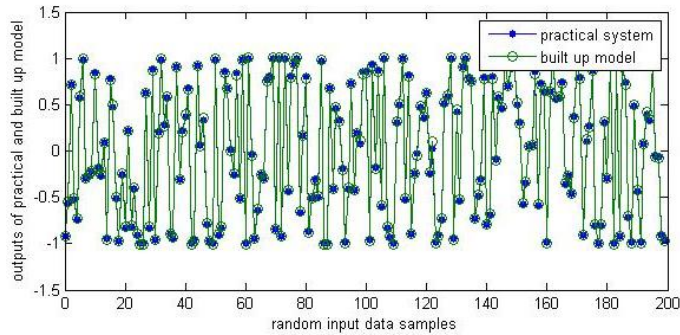
a) Outputs comparison between the actual system and the model derived based on random inputs
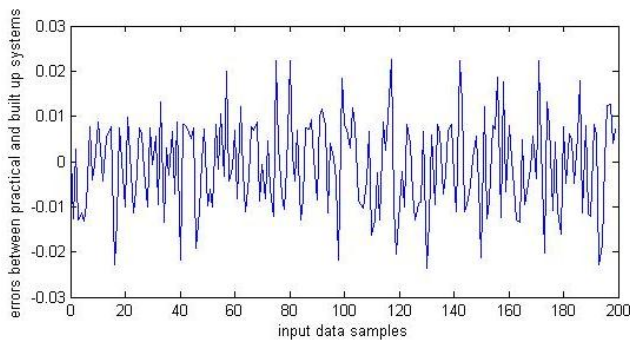
b) Errors between the actual system and the model derived based on random inputs

Fig.41 Comparison of the actual system and the model based on random inputs

The root mean square error between the practical system and the model based on random inputs is under 0.01, which shows that the model constructed by the neural network for the entire system can be deemed as accurate. The modelling accuracy can be improved further if the training iteration continues.

B. Second order system estimation

In order to validate the proposed method in mechanical dynamic system identification, a second order system is investigated in this section. The identification concept is shown in Fig.42.
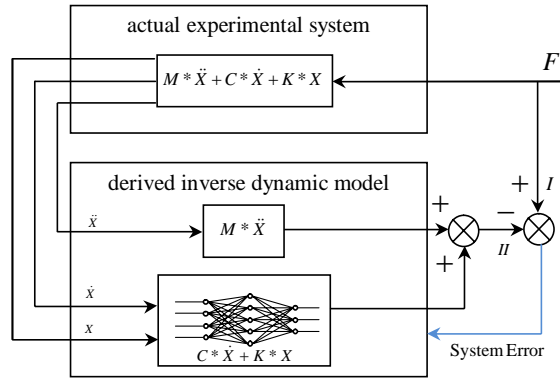
Fig.42 Dynamic model identification of a second order system: I. Target output; II. Constructed model output

It is assumed that in such a second order system the mass parameter M is known; and the damping coefficient C and elastic coefficient K are unknown. The aim of dynamic model identification in this example is to construct an accurate inverse dynamics model for the second order system, which implies that given the acceleration $\ddot{X}$, velocity $\dot{X}$ and the position X information, the driven force F required by the system can consequently be computed. To achieve such an aim, the unknown damping and elastic terms of the dynamics need to be identified.

In practice, an experiment can be carried out on the forward dynamics of this second order system in which a specific driven force is exerted on the system and system response results consisting of acceleration, velocity and position can hence be obtained. For the inverse dynamic modelling process, such experimental data from the forward dynamics can be utilized to train the neural network for the unknown terms of the inverse dynamics, herein $C * \dot{X} + K * X$, by applying the modified LM algorithm. In the neural network training process, the outputs of the forward dynamics, namely, acceleration, velocity and position, are taken as the input data of the inverse dynamic model and the driving force F is taken as the target output data. The errors between the target output and model output will converge towards zero if the neural network is well trained by the modified LM algorithm. Thus, the unknown terms of the inverse dynamics and the whole inverse dynamic model can be deemed to be identified correctly and constructed successfully for the particular experiment data.

For detailed illustration, a sinusoidal input force was adopted as the input signal of the forward dynamics of the system as a numerical example, which is shown in Fig. 43.
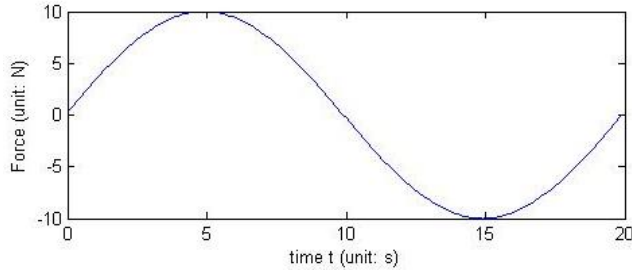
Fig. 43 Input excitation force of the forward dynamics

The amplitude of the input force was 10 N and the period was 20 seconds. In the forward dynamic system, the mass M equaled 1 kg; damping coefficient C equaled 5; and elastic coefficient K equaled 10.

Along with the input signal, the output data of the forward dynamics were also collected as training data and used to train the neural network so as to build up an inverse dynamic model based on this particular excitation. A single hidden layer neural network, which consisted of 10 neurons, with two inputs and one output was utilized. The training process the neural network underwent was based on batch data in each iteration. The training process as well as the results of the constructed model are presented in Fig. 44.
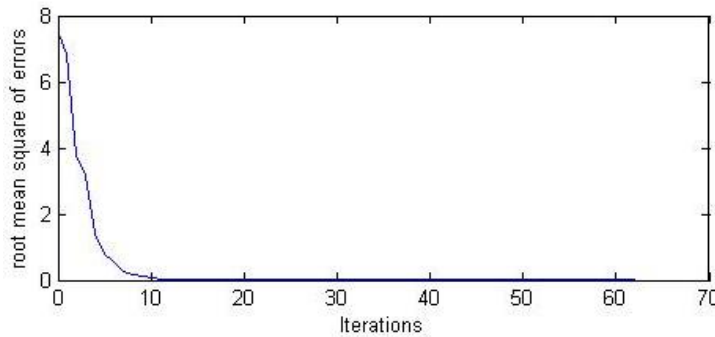
a) RMS of errors between the target output and the constructed model output during neural network training
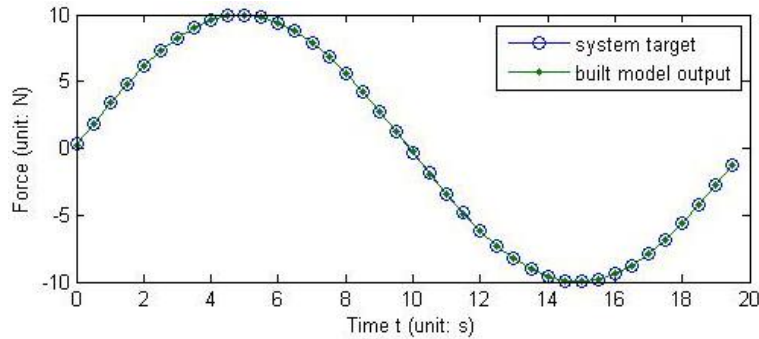
b) Comparison between target output data (F) and trained model output at the 60th iteration
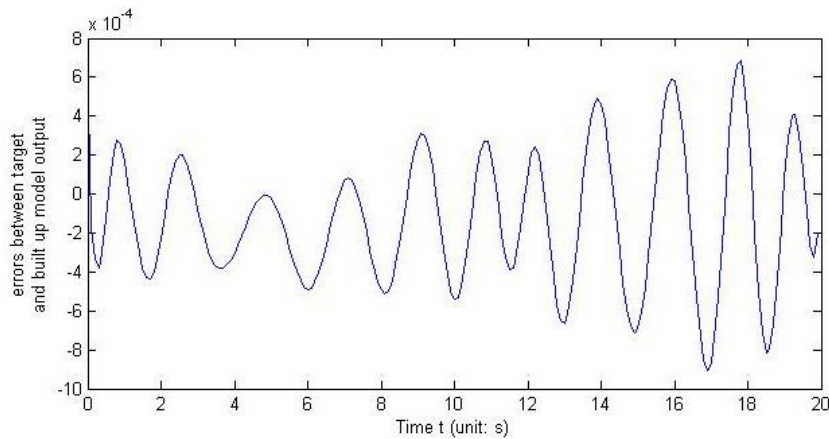
c) Errors between target output data (F) and trained model output at the 60th iteration

Fig.44 Neural network training process and results of trained model

In Fig.44.(a), the model converges fast at the beginning of the neural network training, and after 10 iterations the error between the target output and model output reaches 1.0e-3 and starts to converge slowly. Fig. 44 (b) and Fig.44 (c) present a comparison of the results for the target output and the model output.

For validation of the built-up model, two different input signals, a sinusoidal signal with a period of 40 seconds and a cosine signal with a period of 20 seconds, were exerted on the system individually as the target output reference of the inverse dynamics model. The corresponding outputs from the forward dynamics were input into the model with the well trained neural network. A comparison of the results for the reference target and the outputs of the model is shown in Fig. 45.
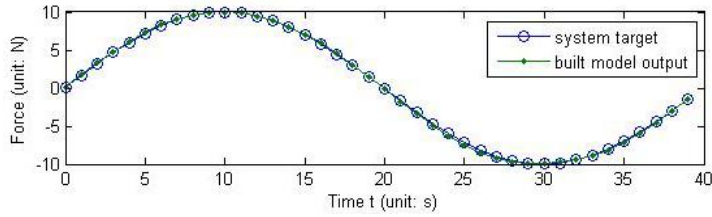
a) Comparison between the target data and output data of the constructed model based on sinusoidal signal
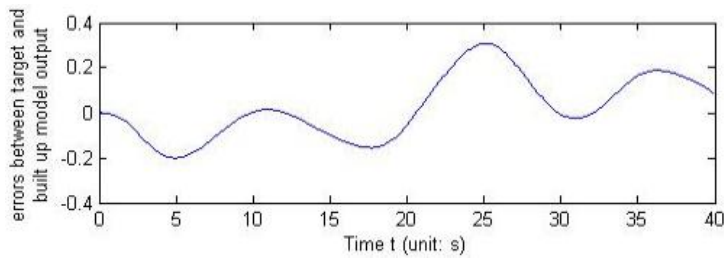
b) Error between the target data and output data of the constructed model based on the sinusoidal signal
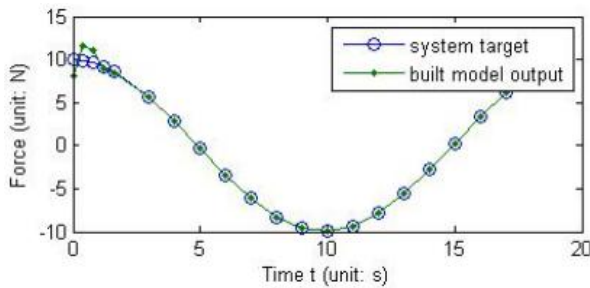
c) Comparison between the target data and output data of the constructed model based on the cosine signal
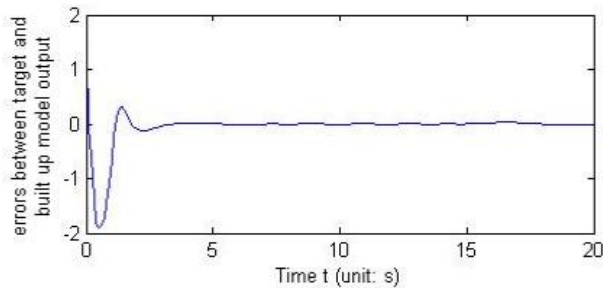
d) Error between the target data and output data of the constructed model based on the cosine signal

Fig.45 Comparison of the results for the target data and the constructed model output based on different excitation signals

In Fig.45 (b) and (d), the error results imply that the built-up model has less accuracy based on the different excitation signals from the training signal. The reason for the reduced accuracy is that the input data of the neural network yielded by the different signals were outside the domain of the training. However, the yielded outputs from the constructed model can still match the accuracy requirements for some applications, such as a controller design based on inverse dynamics. Furthermore, in practice this accuracy weakness can be overcome by augmenting the experimental data for the neural network training to cover the whole possible domain of the application under study.

C. Friction model estimation of a parallel robot

In this section, an example of dynamic model identification by the modified LM training algorithm is illustrated on a more complicated system – a parallel structure based manipulator.

For inverse dynamics modelling of parallel robot/manipulators, Newton-Euler formulation and Lagrangian formulation are widely employed in the literature [12]. In both methods, the friction forces in the joints of the robot are ignored. However, in practical cases, when the lubrication of robot joints is not well maintained and the robot is under heavy duty payload or the pose of the robot is close to the singularity condition, the friction forces play a significant role in the robot dynamics.

In this section, an inverse dynamics model is derived for a parallel manipulator, CaPaMan, in which the friction model is approximated by the neural network using the modified LM algorithm. The manipulator, as shown in Fig.46, possesses 3 driven degrees of freedom (DOF) and consists of a movable end-effector, a base and three legs. The leg consists of a parallelogram mechanism, which is driven by a servo motor, and a vertical bar, which can only slide perpendicular to the parallelogram plane. The spherical joint is used for the up-joint of the vertical bar.
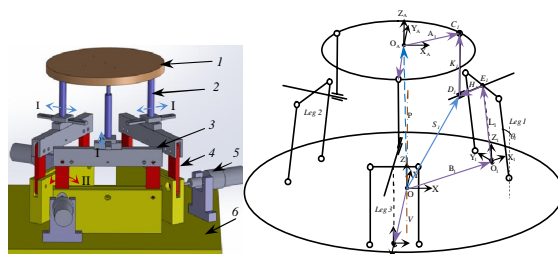
Fig.46 3D model and kinematic scheme of CaPaMan: 1. End-effector 2. Vertical bar 3. Parallelogram mechanism 4. Driven crank of parallelogram 5. Servo motor 6. Base. I. Passive freedom sliding joint II. Active drive

Since the sliding direction of the vertical bar (Fig. 46 I) is perpendicular to the driving direction of the parallelogram, the friction force in this sort of joint is significantly large compared with the friction force of other joints being revolute or ball joints, thus only such friction forces are taken into account in the inverse dynamics modelling of the robot. The forward dynamics of the parallel manipulator is simulated in MSC.ADAMS software, and the control strategy is implemented in MATLAB Simulink.

The inverse dynamics modelling process of this parallel robot, which incorporates the neural network modelling for the friction model, is shown in Fig.47.
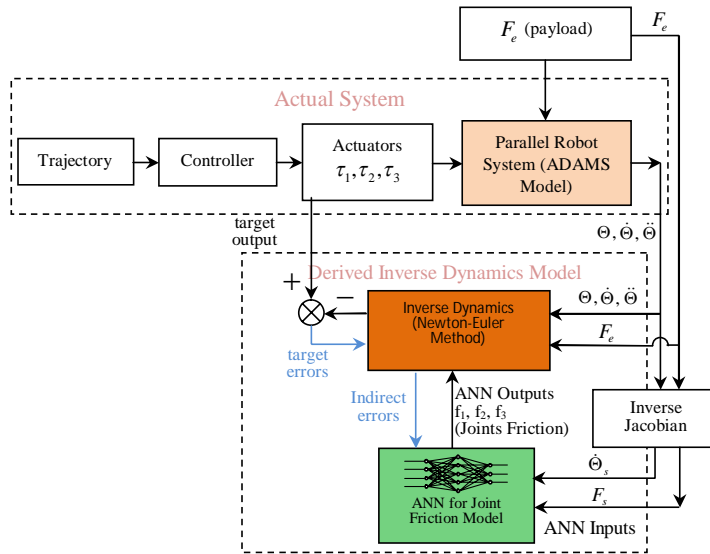
Fig.47 Inverse dynamics modelling process

An experiment can be carried out on the target practical robot system over an interested trajectory or a cluster of several interested trajectories. The corresponding driving torques in the actuators, τ_1, τ_2 and τ_3, the end-effector's acceleration $\ddot{\Theta}$, velocity $\dot{\Theta}$, position Θ and payload F_e can thus be measured. Based on the Newton-Euler formulation, an inverse dynamics model can be derived, in which the unknown friction forces in the sliding joints are included as variables and deemed as a 'black box'. The neural network is then utilized to identify and substitute such a 'black box'. The training process of the neural network is implemented based on the prior measured data from the whole forward dynamics, namely τ_1, τ_2, τ_3, F_e, $\ddot{\Theta}$, $\dot{\Theta}$ and Θ. The inputs of the neural network are the

forces F_s acting on the sliding joints and the relative velocity $\dot{\Theta}_s$ of the sliding joint, which are computed inversely from the end-effector's payload F_e and velocity $\dot{\Theta}$. The modified LM training algorithm is utilized herein for the neural network training. If the neural network is well trained, the errors between the driving torques of the actuator and the outputs of the constructed inverse dynamics model should converge towards zero. If such convergence to zero occurs, the friction model and the inverse dynamic model can be deemed to have been successfully identified and constructed for the specific trajectories of interest.

For detailed demonstration, an example is illustrated based on the trajectory given in Fig. 48.
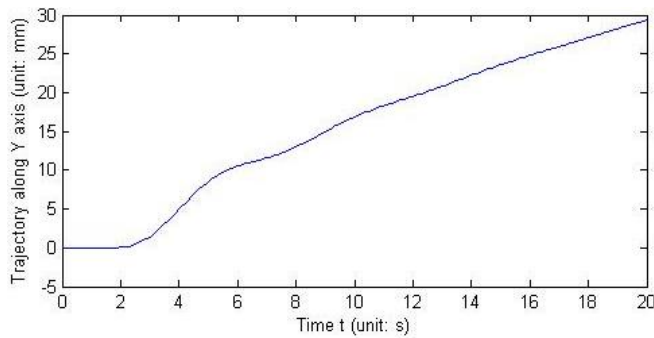
Fig.48 Experimental trajectory

The end-effector of the parallel manipulator was controlled to implement the trajectory in Fig 48 along the Y-direction in the global reference frame of the manipulator base (in the kinematic scheme of Fig. 46). To realize this trajectory, leg1 and leg2 are driven while leg3 stays still.

In order to identify the friction models in the sliding joints of leg1 and leg2, a multi-inputs-outputs neural network with a single hidden layer structure was employed, in which the velocity of the sliding joints and the force acting on the sliding joints comprise the 4 inputs of the neural network, the joints' friction forces comprise the 2 outputs, and 10 neurons are utilized in the hidden layer. 200 data set samples of the actuators' torques and the corresponding end-effector outputs -- acceleration, velocity, position -- as well as the payload were utilized to constitute the batch training data of the neural network, which were generated from the implementation of the given trajectory.

Results for the training process and the constructed inverse dynamics model are shown in Fig.49.
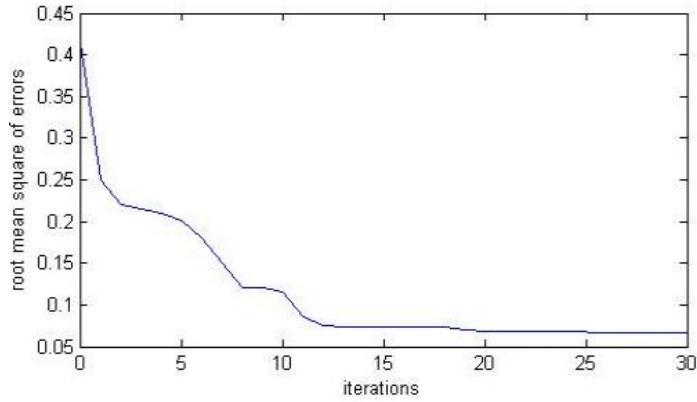
a). RMS of errors between the actuator torques and the constructed inverse dynamics output during the neural network training
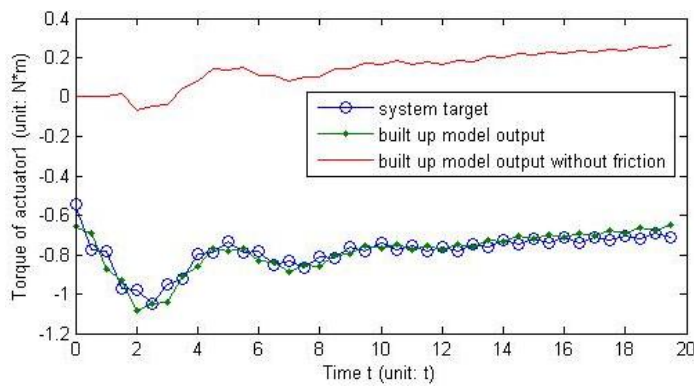
b) Comparison between the torque of actuator1 (leg1) and the corresponding output of the inverse dynamic model
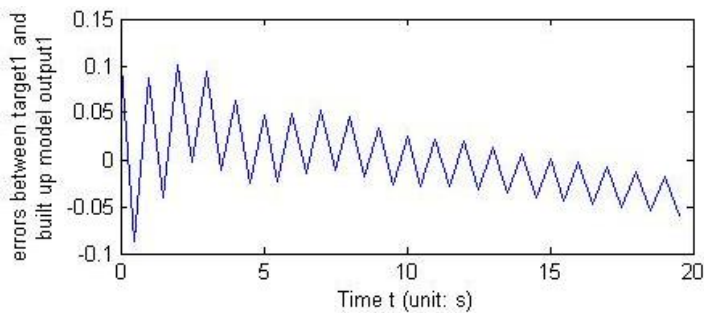
c) Errors between the torque of actuator1 (leg1) and the corresponding output of the inverse dynamic model

101
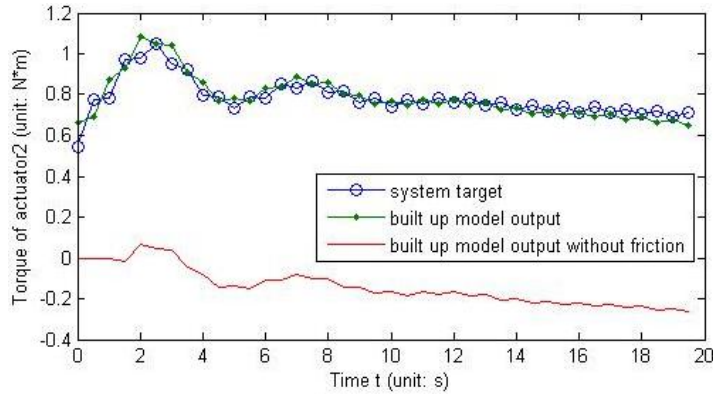
d) Comparison between the torque of actuator2 (leg2) and the corresponding output of the inverse dynamic model
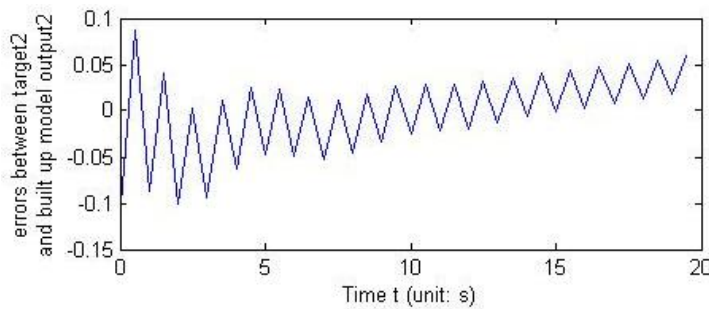
e) Errors between torque of actuatot2 (leg2) and the corresponding output of inverse dynamic model

Fig.49 Results for the constructed inverse dynamic model by incorporating the neural network for a friction model

In Fig. 49 (a), the training process of the neural network and the process of the inverse dynamic model converge fast at the beginning of the training, but start to converge more slowly after around 12 iterations. The training process finishes at around the 30th iteration since the parameter μ in the updating rule of Eq. (90) reaches the maximum value 1.0e15. By this point of the training, the RMS of the errors between the torques of the actuators and the outputs of the inverse dynamic models equals 0.065. The RMS is computed by comparing the two outputs of the inverse dynamics model and the actual input torques of the two actuators over the whole batch training data in each iteration.

Fig. 49 (b) to (e) show the output results of the constructed inverse dynamics model of the parallel manipulator over the given specific trajectory at the 30th training iteration, at which point the neural network and the derived inverse dynamics are considered well

trained and identified. A comparison between the actual input torques of the actuators, the outputs of the constructed inverse dynamics model with the friction model of the neural network, and the outputs of the inverse dynamics model without the friction model is given in Fig. 49 (b) to (e). It can be seen that the friction model for this manipulator along the particular trajectory of the end-effector can be well approximated by the neural network using the modified LM algorithm, and a satisfactory inverse dynamics model can be constructed.

In practice, the number of trajectories of a robot is limited according to its in-situ applications. Thus, an applicable inverse dynamics model could be derived with the method above by augmenting the neural network training to cover the complete possible domain of the trajectories of interest.

4.4 Conclusion

This chapter proposed a feedforward control strategy for suppression of vibration caused by external disturbances acting on the end-effector of a parallel robot. An inverse dynamics model was employed in the feedforward control path, which generates a compensation signal on the actuators of the robot to cancel out the effect from the external disturbance. Validation of the proposed method was performed on a parallel manipulator in a software environment. Problems associated with applying such an approach in practice were discussed. Complications arise from the difficulty of accurately modelling the dynamics of the target system because of unknown parts of the dynamics in the system.

As a solution, a BP neural network was proposed for identification of such unknown parts of the system dynamics. A modified Levenberg-Marquardt algorithm was developed that can utilize the experimental input-output data set of the entire dynamics system to train the BP neural network for the unknown parts. Validation of an approach utilizing such a BP neural network and modified Levenberg-Marquardt algorithm was performed with three application examples. It was noticed that the accuracy of the constructed dynamic model incorporating the BP neural network started to degenerate when the testing data were outside the range of the experimental training. This finding illustrates one of the intrinsic weaknesses of neural networks, namely that neural networks are only effective within the training domain and cannot accurately extrapolate behavior of a target system beyond the training domain [73].

CHAPTER 4

CHAPTER 5

CONCLUSIONS

5.1 Summary of the Dissertation

In order to obtain satisfactory machining performance for a kinematic redundant serial-parallel robot machine, the dissertation proposes two control strategies including the trajectory planning and vibration suppression.

For a given prescribed trajectory of the robot's end-effector in the Cartesian space, a set of trajectories in the robot's joints space are generated based on the best stiffness performance of the robot along the prescribed trajectory.

In order to construct the system-wide analytical stiffness model for the serial-parallel robot machine, a variant of the virtual joint method (VJM) is proposed that is an evolution of Gosselin's lumped model and can account for the deformations of a flexible link in more directions. The prominent advantage of the VJM variant method compared with the MSA method is that it can be applied in a flexible structure system with complicated kinematics formed in terms of flexible serial links and joints. Moreover, by combining the VJM variant method and the virtual work principle, a system-wide analytical stiffness model can be easily obtained for mechanisms with both serial kinematics and parallel kinematics. In the dissertation, a system-wide stiffness model of a kinematic redundant serial-parallel robot machine is developed based on combining the VJM variant and the virtual work principle. Numerical results on the stiffness performance of the model are presented.

In order to generate a set of feasible joints' trajectories for a prescribed trajectory of the end-effector of a kinematic redundant robot, the system-wide stiffness performance of the robot is taken as the constraint in the joints trajectory planning. For a prescribed location of end-effector, the robot permits an infinite number of inverse solutions, which consequently yields infinite sorts of stiffness performance. Therefore, a differential evolution (DE) algorithm is employed to search for the best stiffness performance of the robot, in which the positions of redundant joints in the kinematics are taken as the input variables. Numerical results of the generated joint trajectories are given for the kinematic redundant serial-parallel robot machine, IWR, when a particular trajectory of its end-effector has been prescribed.

For the suppression of vibration occurring in the robot machine during the machining process – a result of the varying cutting force – a feedforward control strategy is proposed that is constructed based on an inverse dynamics model of the target system. The effectiveness of applying such feedforward control in vibration suppression is validated in a software environment for a parallel manipulator. Problems associated with utilizing the feedforward control in practical environments are discussed in the

dissertation. Complications arise from difficulties in modelling the practical system due to unknown components in its dynamics. As a solution, a BP neural network is proposed for identification of the unknown components of the dynamics of the target system. A modified Levenberg-Marquardt algorithm is proposed for training such a BP neural network for the unknown components of the system dynamics that can utilize an experimental input-output data set of the entire dynamic system. Validation of the BP neural network and the modified Levenberg-Marquardt algorithm is performed by a sinusoidal output approximation, a second order system parameters estimation and a friction model estimation of a parallel manipulator, which represent three different applications of this method.

5.2 Conclusions of the Dissertation

The validation of the novel VJM variant is done by comparing the computed stiffness results of a flexible link with the those of matrix structural analysis. The comparison shows that the numerical results from both methods on an individual flexible beam are almost identical, which in some sense validates the two methods. The stiffness modelling process of IWR shows that the VJM variant combined with the virtual work principle can efficiently deal with the modelling case in which the complicated parallel and serial structures are included, and the final obtained stiffness model is completely analytical and computational-efficient.

The numerical results obtained from the stiffness model of IWR show that the stiffness performance of entire robot under the assumption of a rigid serial part is possibly weaker in some interested directions than the those under the assumption of a flexible serial part. The reason behind is that the redundant flexibility in the serial part of the robot allows the deformation of the robot to occur in other possible directions, which to some extent can mitigate the deformation of the parallel part along one direction. This phenomenon can also be interpreted from the energy point of view, since the flexible serial parts can absorb the external energy in other deformation directions. Moreover, it implies that the system-wide stiffness performance of the robot can be optimized at the prescribed trajectory due to the existence of redundant flexible kinematics.

The numerical results of the joints trajectories which are generated based on the stiffness optimization shows that they are feasible for realization in the control system, since they are acceptably smooth. This finding also implies that the stiffness performance of the robot machine deviates smoothly with respect to the kinematic configuration in the adjacent domain of its best stiffness performance.

The results of applying the feedforward control approach to suppress the chatter vibration on a parallel manipulator indicate that it is an effective method to reject the vibrations of robot, which are caused by the varying external payload force. The premise of applying

such an approach regarding the practical application is to construct an accurate inverse dynamics model for the target robotic system.

The results of applying the BP neural network for the identification of the unknown components of the dynamics of a target system show that the modified Levenberg-Marquardt algorithm is effective for the training of such BP neural network based on the experimental input-output data set of the entire dynamic system. It should be noticed that the accuracy of the constructed dynamic model incorporation the BP neural network started to degenerate when the testing data were outside the range of the experimental training. In order to get a stable accuracy of such BP neural network for the target system, more training data which covers more interested domains of the target system should be utilized.

5.3 Future Work

Although numerical results on the stiffness performance of IWR are given in the dissertation for the proposed VJM variant method and the virtual principle work, experimental measurement on the robot still needs to be carried out to validate the accuracy of the proposed method. For a given prescribed trajectory of end-effector of IWR, the corresponding joints' trajectories were generated in the dissertation based on the maximized stiffness performance. However, the practical machining performance needs to be compared with other kinematics configurations by experimental measurement that is not obtained under the constraint of maximized stiffness.

In the third example of dynamics model identification using the BP neural network and the modified Levenberg-Marquardt algorithm, the friction model of the joints in the parallel manipulator is deemed to have been identified, but the identified model is locally limited, since it is obtained only based on one prescribed trajectory of the parallel manipulator. In order to cover all the trajectories of interest in the target system, more training over a larger domain of interest needs to be carried out. In the BP neural network training process in the dissertation, it is found that the identification results for the unknown components in the dynamics can be even better if extra weights are adopted between the outputs layer of the neural network and the following parts of the dynamics system; online adjustment of the size of the neural network can also contribute greatly to the training efficiency of the neural network, since selection of the proper size of neural network has a big influence on the accuracy of the constructed model. A well trained neural network can also present some extrapolation character for the constructed dynamics model. Future research work could focus on these incomplete findings.

CHAPTER 5

REFERENCES

REFERENCES

[1]. https://www.iter.org/industry. (Retrieved on Aug.14.2014).

[2]. https://www.iter.org/mach/vacuumvessel. (Retrieved on Aug.14.2014).

[3]. H. Wu, P. Pessi, H. Handroos. Assembly and repairing for ITER vacuum vessel with mobile parallel robot. *2007 IEEE 22nd Symposium on Fusion Engineering. 2007.*

[4]. P. Pessi, H. Wu, H. Handroos and L. Jones. A mobile robot with parallel kinematics to meet the requirements for assembling and machining the ITER vacuum vessel. *Fusion Engineering and Design*, 2007, pp. 2047-2054.

[5]. A. Ghali, A.M. Neville, T.G. Brown. Structural analysis: a unified classical and matrix approach. Spon Press, NY, 2003.

[6]. Y.W. Li, J.S. Wang, and L.P. Wang. Stiffness analysis of a Stewart platform-based parallel kinematic machine. *Proc. of IEEE Int. Conf. On Robotics and Automation (ICRA)*, Washington, US, May 11-15 2002, vol. 4, pp. 3672-3677.

[7]. T. Huang, X. Zhao, and D.J. Whitehouse. Stiffness estimation of a tripod-based parallel kinematic machine. *IEEE Trans. on Robotics and Automation*, 18(1) (2002), pp. 50-58.

[8]. C.M. Gosselin. Stiffness mapping for parallel manipulators. *IEEE Transactions on Robotics and Automation*, Vol. 6, No. 3, pp. 377-382.

[9]. D.R. Kerr. Analysis, property, and design of a Stewart-platform transducer. *ASME Journal of Mechanisms*, Transmissions and Automation in Design, Vol. 111, pp.25-28.

[10]. B.S. EI-Khasawneh and P.M. Ferreira. Computation of stiffness and stiffness bounds for parallel link manipulators. *International Journal of Machine Tools and Manufacture*, 39(2) (1999), pp. 321-342.

[11]. D. Zhang. Kinetostatic analysis and optimization of parallel and hybrid architectures for machine tools. Ph.D. thesis, Laval University, Quebec, Canada, 2000.

[12]. L Tsai. Robot analysis: the mechanics of serial and parallel manipulators. Wiley-Interscience Publication, 2009.

[13]. D. Deblaise, X. Hernot and P. Maurine. Systematic analytical method for PKM stiffness matrix calculation. *IEEE International Conference on Robotics and Automation (ICRA)*, Orlando, Florida, May 2007. pp. 4213-4219.

[14]. G. Piras, W.L. Cleghorn and J.K. Mills. Dynamic finite-element analysis of a planar high-speed, high-precision parallel manipulator with flexible links. *Mechanism and Machine Theory*, 40(7) (2005), pp. 849-862.

[15]. C.S. Long, J.A. Snyman, A.A. Groenwold. Optimal structural design of planar parallel platform for machining. *Applied Mathematical Modelling*, 27(8) (2003), pp. 581-609.

[16]. R. Rizk, J.C. Fauroux, M. Mumteanu, G. Gogu. A comparative stiffness analysis of a reconfigurable parallel machine with three or four degrees of mobility. *Journal of machine engineering*, 6(2) (2006), pp. 45-55.

REFERENCES

[17]. H.C. Martin. Introduction to matrix methods of structural analysis. McGraw-Hill Book Company, 1966.

[18]. C.K. Wang. Matrix methods of structural analysis. International Textbook Company, 1966.

[19]. C.M Clinton, G. Zhang, and A.J. Wavering. Stiffness modelling of a Stewart-platform-based milling machine. *Trans. of the North America Manufacturing Research Institution of SME*, Vol. XXV, 1997, pp. 225-240.

[20]. C.M. Gosselin, D. Zhang. Stiffness analysis of parallel mechanisms using a lumped model. *Int. J. of Robotics and Automation*, 17(1) (2002), pp 17-27.

[21]. J.J. Craig. Introduction to robotics: mechanics & control. ADDISON-WESLEY PUBLICATION COMPANY.

[22]. R.P. Paul and H. Zong. Robot motion trajectory specification and generation. *2nd International Symposium on Robotics Research*, Kyoto, Japan, August 1984.

[23]. A. Gasparetto, P. Boscariol, A. Lanzutti, R. Vidoni. Trajectory Planning in Robotics. *Mathematics in Computer Science*. (2012) 6, pp. 269-279.

[24]. S. Yue, D. Henrich, W.L. Xu and S.K. Tso. Point-to-point trajectory planning of flexible redundant robot manipulators using genetic algorithms. *Robotica*, Volume 20, Issue 03, May 2002, pp 269-280.

[25]. C Chen, T Liao. A hybrid strategy for the time- and energy-efficient trajectory planning of parallel platform manipulators. *Robotics and Computer-Integrated Manufacturing* 27 (2011), pp. 72-81.

[26]. Z. Shiller, S. Dubowsky. Robot path planning with obstacles, actuator, gripper, and payload constraints. *Int. J. Robot Res*,1989, 8(6), pp. 3-18.

[27]. S. Pugazhenthi, T. Nagarajan, M. Singaperumal. Optimal trajectory planning for a hexapod machine tool during contour machining. *Proceedings of the institution of mechanical engineers, Part C: Journal of Mechanical Engineering Science*, pp 1247-1257.

[28]. S. Muruganandam, S. Pugazhenthi. Stiffness-based workspace atlas of hexapod machine tool for optimal work piece location. *Int. J. Adv Manuf Technol* (2009) 42:202-210.

[29]. H.P. Gavin. Mathematical properties of stiffness matrices. *Lecture materials*. Duke university. http://people.duke.edu/~hpgavin/cee421/matrix.pdf.

[30]. D.J. Kidger. Eigenvalues of element stiffness matrices, part I: 2-D plane elements. *Engineering Computations*, Vol.9, Iss: 3, pp. 307-316.

[31]. F. Tahmasebi. Kinematic synthesis and analysis of a novel class of six-DOF parallel mini-manipulators. PhD dissertation, University of Maryland.

[32]. R. Storn and K. Price. Differential evolution -- a simple and efficient heuristic for global optimization over continuous spaces. *Journal of Global Optimization*. (1997) 11, pp. 241-259.

REFERENCES

[33]. M.O. Tokhi and A. K. M. Azad. Control of flexible manipulator systems. *Proceedings of IMechE-I: Journal of Systems and Control Engineering 210*, 283-292 (1996).

[34]. A. Preumont. Vibration control of active structures: an introduction. Kluwer Academic Publishers, 2002.

[35]. R.L. Clark and W.R. Saunders. Adaptive structure: dynamics and control, John Wiley &Sons, 1998.

[36]. S.K. Tso, T.W. Yang, W.L. Xu, Z.Q. Sun. Vibration control for a flexible-link robot arm with defection feedback, *Int. J. of Non-Linear Mechanics*, 38 (2003) 51–62.

[37]. X. Zhang, J. K. Mills, and W. L. Cleghorn. Flexible linkage structural vibration control on a 3-PRR planar parallel manipulator: experimental results. *Proc. IMechE*, Vol. 223 Part I: J. Systems and Control Engineering, 2009.

[38]. A. Sharon, N. Hogan, D. E. Hardt. The micro manipulator: an improved architecture for robot control. *Robotics Comput. Integrated Manufact*, 10 (3) (1993), 209–222.

[39]. K. Nagaok and T. Sato. Feedforward controller for continuous path control of CNC machine tools. *Int. J. of simulation*, Vol.7.No.8.

[40]. J. Sjöberg, Q. Zhang, L. Ljung, A. Benveniste etc. Nonlinear black-box modeling in system identification: a unified overview. *Automatica*, Vol. 31, No. 12, pp. 1691-1724, 1995.

[41]. L. Ljung and T. Sodersrom. Theory and Practice of recursive identification. Cambridge, MA: MiT Press, 1983.

[42]. A. A. Geogriev. Nonparametric system identification by kernel methods. *IEEE Trans. Automat. Contr*, Vol. 29. pp. 356-358, 1984.

[43]. J. Wu, J. Wang, Z. You. An overview of dynamic parameter identification of robots. *Robotics and Computer-Integrated Manufacturing (2010)*, pp. 414-419.

[44]. J. Wu, J. Wang, L. Wang, T. Li. Dynamic formulation of redundant and nonredundant parallel manipulators for dynamic parameter identification. *Mechatronics 2009*, 19(4), pp 586-590.

[45]. J. Swevers, W. Verdonck, J.D. Schutter. Dynamic model identification for industrial robots. *IEEE Control Systems Magazine 2007*, 27(5). pp 58-71.

[46]. M. Grotjahn, B. Heimann, J. Kuehn, H. Grendel. Dynamics of robots with parallel kinematic structure. *Proceedings of the 11th world congress on theory of machines and mechanisms*, Tianjin, China, 2004. pp 1689-1693.

[47]. C. Atkeson, J. Hollerbach. Estimation of inertial parameters of manipulator loads and links. *International Journal of Robotics Research 1987*, 5(3), pp. 101-119.

[48]. N.D. Vuong, H.J. Marcelo. Dynamic model identification for industrial robots. *Acta Polytechnica Hungarica*, Vol. 6, No. 5, 2009.

REFERENCES

[49]. D.W. Marquardt. An algorithm for least-squares estimation of nonlinear parameters. *Journal of the society for industrial and applied mathematics 1963*, Vol. 11, No. 2, pp.431-441.

[50]. W. Khalil, S.D. Guegan. Inverse and direct dynamics modeling of Gough-Stewart robots. *IEEE Transactions on Robotics 2004*, 20(4). pp 754-762.

[51]. S. Kumpati, K. Parthasarathy. Neural networks and dynamics system, Part II: Identification. *Tech. Rep. 8902*, Center Syst. Sci., Dept. Elect. Eng., Yale Univ., New Haven, CT. Feb. 1989.

[52]. Z. Jiang, T. Ishida, M. Sunawada. Neural network aided dynamic parameter identification of robot manipulators. *Proceedings of the IEEE international conference on systems, man and cybernetics*, Taipei, Taiwan, 2007. pp. 3298-3303.

[53]. S. Chen, S.A. Billings and P.M. Grant. Nonlinear system identification using neural networks. *Int. J. Contr*, Vol. 51, No. 7, pp. 1191-1214.

[54]. N. V. Bhat etc.. Modeling chemical process systems via neural computation. *IEEE Contr. Syst. Mag.*, pp. 24 -29, Apr. 1990.

[55]. S. Bhama and H. Singh. Single layer neural networks for linear system identification using gradient descent technique. *IEEE Trans. Neural Networks*, Vol. 4, pp. 884 - 888, Sept, 1993.

[56]. Sunil Elanayar V.T, Yung C. Shin. Radial basis function neural network for approximation and estimation of nonlinear stochastic dynamic systems. *IEEE Transactions on neural networks*, Vol. 5, 1994.

[57]. J.C. Patra, R.N. Pal, B.N. Chatterji, G. Panda. Identification of nonlinear dynamic systems using functional link artificial neural networks. *IEEE Transactions on system, man and cybernetics - part B: cybernetics*, Vol. 29, No. 2, April 1999.

[58]. H. Yu, M.W. Bogdam. Levenberg-Marquardt Training. *The Industrial Electronics Handbook*, Vol. 5 − Intelligent Systems, 2nd ed. ,CRC Press, Boca Raton, 2011.

[59]. Sun. X.D., Clarke. T.. Advanced aircraft flight control using nonlinear inverse dynamics. *Control Theory and Applications*, Volume 141, Issue 6, Pages 418 - 426, Nov 1994.

[60]. J. Nakanishi, M. Mistry, S. Schaal. Inverse dynamics control with floating base and constraints. *2007 IEEE International Conference on Robotics and Automation*, pp 1942 - 1947.

[61]. M. Mistry, J. Buchli, and S. Schaal. Inverse Dynamics Control of Floating Base Systems Using Orthogonal Decomposition. *Proceedings of the 2010 IEEE International Conference on Robotics & Automation*, pp. 3406 – 3412.

[62]. Jankowski. K. P., Van Brussel, H.. An approach to discrete inverse dynamics control of flexible-joint robots. *IEEE Transactions on Robotics and Automation*, Vol. 8, No.5, October 1992.

REFERENCES

[63].   S. Lee, J. Song, W. Choi, D. Hong. Position control of a Stewart platform using inverse dynamics control with approximate dynamics. *Mechatronics*, Volume 13, Issue 6, July 2003, Pages 605 - 619.

[64].   D. Croft, G. Shedd, S. Devasia. Creep, hysteresis, and vibration compensation for piezoactuators: atomic force microscopy application. *ASME J Dyn Syst Meas Ctrl*, 123 (2001), pp 35 - 43.

[65].   C. Løvaas, M.M. Seron, G.C. Goodwin. Inverse minimax optimality of model predictive control policies. *System & Control Letters*, Volume 58, Issue 1, January 2008, Pages 31 - 38.

[66].   H. Wu, Y. Wang, M. Li, M. Al-Saedi, H. Handroos. Chatter suppression methods of a robot machine for ITER vacuum vessel assembly and maintenance. *Fusion Engineering and Design*, March 2014.

[67].   M. Li, H. Wu, H. Handroos, M. Ceccarelli, G. Carbone. Vibration control for parallel manipulator based on the feed forward control strategy. *ASME 2013 International Mechanical Engineering Congress and Exposition*, Volume 4B: Dynamics, Vibration and Control, San Diego, California, USA, November, 2013.

[68].   J.J. Azar. Matrix Structural Analysis. PERGAMON PRESS INC, 1972.

[69].   M. Ceccarelli. A new 3 D.O.F spatial parallel mechanism. *Mech.Mach.Theory*, Vol. 32, No.8, pp895-902,1997.

[70].   G. Carbone. Stiffness analysis for an optimal design of multibody robotic systems. *Chapter 11, Robot Manipulators New Achievements*, InTech, 2010.

[71].   G. Carbone, M. Ceccarelli. Comparison of indices for stiffness performance evaluation, *Frontiers of Mechanical Engineering in China*, September 2010, Volume 5, Issue 3, pp 270-278.

[72].   M.T.Hagan, M. Menhaj. Training feed-forward networks with the Marquardt algorithm. *IEEE Transactions on Neural Networks*, Vol. 5, No. 6, 1999, pp. 989–993, 1994.

[73].   M.T. Hagan, B.D. Howard. Neural networks for control. *American Control Conference, 1999*. Proceedings of the 1999. Vol. 3. IEEE, 1999.

REFERENCES

PART II

PART II: PUBLICATIONS

PART II

Publication I

Ming Li, Huapeng Wu, Heikki Handroos, Marco Ceccarelli, Giuseppe Carbone

Vibration control for parallel manipulator based on the feedforward control strategy

Reprinted from
ASME Conference Proceedings, Volume 4B: Dynamics, Vibration and Control, ASME 2013
International Mechanical Engineering Congress and Exposition, San Diego, California, USA, November 15–
21, 2013, with permission from ASME Digital Collection

IMECE2013-64496

VIBRATION CONTROL FOR PARALLEL MANIPULATOR BASED ON THE FEED FORWARD CONTROL STRATEGY

Ming Li
Laboratory of Intelligent Machines,
Lappeenranta University of Technology
Lappeenranta, Finland

Huapeng Wu
Laboratory of Intelligent Machines,
Lappeenranta University of Technology
Lappeenranta, Finland

Heikki Handroos
Laboratory of Intelligent Machines,
Lappeenranta University of Technology
Lappeenranta, Finland

Marco Ceccarelli
Laboratory of Robotics and
Mechatronics, University of Cassino
and South Latium, Cassino (FR), Italy

Giuseppe Carbone
Laboratory of Robotics and
Mechatronics, University of Cassino
and South Latium, Cassino (FR), Italy

ABSTRACT

Due to the high stiffness, high dynamic performance, the parallel manipulator presents great advantages in the industrial manufacture. However in the machining process, the external low frequency disturbance, e.g. the varying cutting force, has a significant effect on the control system of parallel manipulator, which presents a chatter phenomenon on the end-effector of manipulator.

In this paper, a feed forward control strategy is proposed to eliminate the effect of the random external disturbance on the control system of parallel manipulator. By applying the external disturbance force on the inverse dynamic model, the compensation torque is calculated and fed forward into the manipulator driving joints to cancel out the effect of the disturbance acting on the manipulator end-effector. The key issue herein is to be able to establish the accurate dynamic model for the parallel manipulator.

Furthermore, in order to guarantee the position precision of the manipulator, a feed forward model-based control strategy combined with the feedback loop PV (position and velocity) control has been developed based on the reference trajectory, which could relatively simplify the highly nonlinear control system of the parallel manipulator and obtain a stable tracking error model.

The whole research has been carried out on a parallel manipulator named CaPaMan which has been built in the laboratory of robotics and mechatronics in university of Cassino and South Latium. The results show that the chatter phenomenon could be utterly depressed by the force compensation from the feed forward path of the external disturbance; meanwhile the model-based controller can guarantee the trajectory tracking accuracy within a stable error by choosing the suitable PV gains.

1. INTRODUCTION

Due to the high dynamics performance, improved stiffness and light moving mass as well as the relatively more degrees of freedom in the end-effector, the parallel kinematic robot machine has been considered as the most potential replacement of the conventional machine tools. However, after many researchers have dedicated to the industrial application of parallel mechanism for many years, only few parallel robot concept has survived in the practical applications, such as the Gough/Stewart structure, delta robot. Even fewer parallel robot has succeeded in the machining application.

Theoretically the parallel robot can achieve great kinematic accuracy based on the established error model by taking into account the manufacturing and assembly errors [1][2], however in practice the obtained accuracy is not satisfying due to its highly nonlinear dynamics which would bring the difficulties in the robust controller design. Although the corresponding nonlinear controllers could been developed and also studied by many researchers either when the robot is unloaded or under the stable load [3][4][5][6]. Nevertheless when the random external varying load is exerted on the end-effector, the developed nonlinear controller becomes incompetent in such situation, and the accuracy of the end-effector will deteriorate seriously due to the chatter vibration of the robot machine. In the machining

process, due to the different cutting speed, depth of cut as well as the feed speed, the varying cutting force is inevitable and the chatter phenomenon occurs consequently, which does not only jeopardize the machining surface quality and the tracking precision, but also cause the sever damage to the robot joints, the functional life of the cutting tool as well as the under-machining product material.

In order to solve the problem of chatter vibration of parallel mechanism, abundant research has been carried on during the past decades, and the methodologies could be generally divided into two categories: (a) optimizing the parallel robot structure in the design stage and (b) employing the active robust control strategy.

By optimizing the parallel kinematic structure, the static and dynamic performance of robot machine could be relatively improved, some researchers have already proposed several approaches [7][8][9]. Meanwhile some other researchers also have proposed another way, by which the online optimization of robot configuration is executed to get the best robot static stiffness along the reference machining trajectory while the redundant freedoms exist in the parallel robot machine [10]. However, these approaches can only alleviate the vibration, but not eliminate the causative mechanism.

Regarding the active control strategy, most of the current research has concentrated on the vibration depression which has been yielded only by the robot system itself. Some researchers have proposed the method of dynamics compensation which is used in the control loop to cancel out the nonlinear characteristic [11]. Some other researchers have proposed the method of optimizing the reference model by various digital filters such as notch filter, Bessel filter etc. [12][13], the essence of which is still trying to attenuate the external varying load caused by the spiky acceleration in the trajectory.

In the machining process, when a robot machine is designed for an extensive cutting parameters and for various material machining [14][15][16], even as the trajectory of end-effector is quite smooth (without any spiky acceleration), the considerable varying cutting force still exists which can't be dealt with by the digital filters mentioned above.

In this paper, a feed forward control strategy is proposed to eliminate the chatter vibration caused by the random external disturbance/force on the end-effector of parallel manipulator. The external varying load is measured and input into the inverse dynamic model of the parallel manipulator as a part of control system. Consequently, the compensation torque could be calculated and fed forward into the manipulator driving joints to cancel out the disturbing effect of the external force acting on manipulator end-effector. Furthermore, in order to guarantee the position precision of the manipulator, a model-based feed forward control strategy has been developed based on the reference trajectory, which could simplify the highly nonlinear control system of the parallel manipulator into a relatively linear close loop control. The research has been simulated and validated on a parallel manipulator named CaPaMan (Cassino Parallel Manipulator) [17], which has been built in the laboratory of robotics and mechatronics in university of Cassino and South Latium. The rest parts of this paper are organized as following: the second section describes the dynamics model of parallel manipulator CaPaMan; the third part elaborates the control strategy; the fourth part gives the chatter depressed results and the future open work; the last parts are acknowledgments and reference.

2. DYNAMICS OF THE PARALLEL MANIPULATOR

The parallel manipulator under research is shown in Fig.1, which possesses 3 driven degrees of freedom (DOF) and consists of a movable end-effector, a basement and three legs. The leg consists of a parallelogram mechanism, which is driven by a servo motor in the left down joint, and a vertical bar which can only slide perpendicular to the parallelogram plane. The up joint of the vertical bar is a spherical joint.
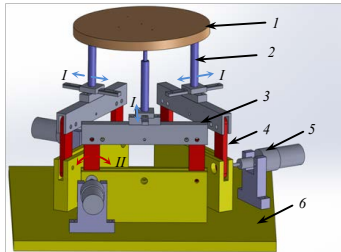
Figure 1. 3D model of CaPaMan: 1. end-effector 2. vertical bar 3. parallelogram mechanism 4. driven crank of parallelogram 5. servo motor 6.basement I. passive freedom II. active drive
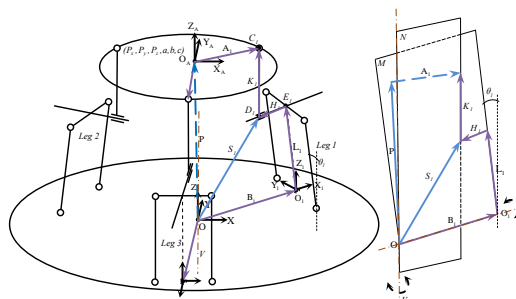
Figure 2. Kinematic scheme of CaPaMan

In the most of current parallel robots, if the end-effector was declaimed to posses certain number of DOF, e.g. 3 DOF --- translations along the x, y axes and rotation around z axis, it is believed that in the workspace the value of coordinates of end-effector only changes in these 3 DOF. However in the parallel manipulator of this paper, even there are only 3 driven DOF in the CaPaMan, its end-effector can still cover 6 DOF in the workspace because of the varying of DOF presentation in some specific points. It means that in a specific trajectory, the end-

effector presents 3 certain freedoms, e.g. translations along x, y axes and rotation around z axis; however in another specific trajectory, the end-effector may present another 3 different freedoms, e.g. translations along y, z axes and rotation around x axis. This phenomenon is hereafter named heterogeneity of workspace in this paper.

Due to the heterogeneity, the available freedom of end-effector of CaPaMan varies in some different workspace point. Consequently, the general fixed-term Jacobin matrix of covering the full 6 DOF does not exist in the workspace. The conventional methods of dynamics analysis, e.g. the principle of virtual work, cannot be employed. Herein the method of adopting the Lagrangian equations of the first type has been taken for the dynamics analysis.

In order to build up the dynamics model, the kinematics should be analyzed first. In this paper, all the reference frames and the kinematic vectors are expressed as shown in Fig.2: the global reference frame OXYZ is located in the center of basement; the local frame $O_A X_A Y_A Z_A$ is fixed in the center of end-effector; the base joint frame $O_1 X_1 Y_1 Z_i$ is fixed in the middle of the bottom line of parallelogram with the x axis perpendicular to the parallelogram plane and z axis vertical of basement; P represents the vector from point O to O_A; B_1 the vector from O to O_1; L_1 the vector from O_1 to E_1 (E_1 is the middle point of up line of parallelogram); H_1 the vector from E_1 to D_1; K_1 the vector from D_1 to C_1 (D_1, C_1: two ends of vertical bar); A_1 the vector from O_A to C_1; S_1 the vector from O to D_1; Let the end-effector coordinates be represented by the vector (P_x, P_y, P_z, a, b, c), in which the (P_x, P_y, P_z) represents the position of end-effector while (a, b, c) represents Euler angles.

a. Kinematic Constraints

Since the configuration of 3 legs in the CaPaMan is homogenous, the analysis on one of them is sufficient to deduce the kinematic constraints. From leg 1 in Fig.2, the close loop kinematic equation is obtained as Eq.1.

$$S_1 = P + A_1 - K_1 \tag{1}$$

As the vertical bar K_1 is always vertical to the basement plane (XY plane), we assume there is a virtual axis V through the point O vertically, and a plane N (in the right part of Fig.2) is formed by this virtual axis V and K_1, which can only rotate around V. As the vector H_1 is always parallel to the vector B_1, the plane M is formed, which can only rotate around B_1. The vector S_1 is the intersection of plane M and N.

Regardless the rotating of plane M, the projections of vector S_1 on the Y_1 and Z_1 axes of frame $O_1 X_1 Y_1 Z_1$ are always equal to the ones of vector L_1 individually. The following constraint equations are obtained:

$$^{R_1}S_1(2) - {}^{R_1}L_1(2) = 0 \tag{2}$$

$$^{R_1}S_1(3) - {}^{R_1}L_1(3) = 0 \tag{3}$$

where the leading superscript R_1 denotes that the vector is expressed in the reference frame $O_1 X_1 Y_1 Z_1$; the '2' in parenthesis denotes the projection on Y_1 axis and the '3' the projection on Z_1 axis.

By analogy the following equations are obtained from leg 2 and leg 3.

$$^{R_2}S_2(2) - {}^{R_2}L_2(2) = 0 \tag{4}$$

$$^{R_2}S_2(3) - {}^{R_2}L_2(3) = 0 \tag{5}$$

$$^{R_3}S_3(2) - {}^{R_3}L_3(2) = 0 \tag{6}$$

$$^{R_3}S_3(3) - {}^{R_3}L_3(3) = 0 \tag{7}$$

Let the left part of Eq.(2) to (7) be represented by the Ct_1 to Ct_6 individually. Since they are the functions of end-effector coordinates (P_x, P_y, P_z, a, b, c) and the rotation angles of parallelogram $\theta_1, \theta_2, \theta_3$, taking the partial derivatives of these constraint functions Ct_i with respect to the 9 generalized coordinates yields

$$\begin{bmatrix} \frac{\partial C_1}{\partial P_x} & \frac{\partial C_1}{\partial P_y} & \frac{\partial C_1}{\partial P_z} & \frac{\partial C_1}{\partial a} & \frac{\partial C_1}{\partial b} & \frac{\partial C_1}{\partial c} & \frac{\partial C_1}{\partial \theta_1} & \frac{\partial C_1}{\partial \theta_2} & \frac{\partial C_1}{\partial \theta_3} \\ \frac{\partial C_2}{\partial P_x} & \frac{\partial C_2}{\partial P_y} & \frac{\partial C_2}{\partial P_z} & \frac{\partial C_2}{\partial a} & \frac{\partial C_2}{\partial b} & \frac{\partial C_2}{\partial c} & \frac{\partial C_2}{\partial \theta_1} & \frac{\partial C_2}{\partial \theta_2} & \frac{\partial C_2}{\partial \theta_3} \\ \frac{\partial C_3}{\partial P_x} & \frac{\partial C_3}{\partial P_y} & \frac{\partial C_3}{\partial P_z} & \frac{\partial C_3}{\partial a} & \frac{\partial C_3}{\partial b} & \frac{\partial C_3}{\partial c} & \frac{\partial C_3}{\partial \theta_1} & \frac{\partial C_3}{\partial \theta_2} & \frac{\partial C_3}{\partial \theta_3} \\ \frac{\partial C_4}{\partial P_x} & \frac{\partial C_4}{\partial P_y} & \frac{\partial C_4}{\partial P_z} & \frac{\partial C_4}{\partial a} & \frac{\partial C_4}{\partial b} & \frac{\partial C_4}{\partial c} & \frac{\partial C_4}{\partial \theta_1} & \frac{\partial C_4}{\partial \theta_2} & \frac{\partial C_4}{\partial \theta_3} \\ \frac{\partial C_5}{\partial P_x} & \frac{\partial C_5}{\partial P_y} & \frac{\partial C_5}{\partial P_z} & \frac{\partial C_5}{\partial a} & \frac{\partial C_5}{\partial b} & \frac{\partial C_5}{\partial c} & \frac{\partial C_5}{\partial \theta_1} & \frac{\partial C_5}{\partial \theta_2} & \frac{\partial C_5}{\partial \theta_3} \\ \frac{\partial C_6}{\partial P_x} & \frac{\partial C_6}{\partial P_y} & \frac{\partial C_6}{\partial P_z} & \frac{\partial C_6}{\partial a} & \frac{\partial C_6}{\partial b} & \frac{\partial C_6}{\partial c} & \frac{\partial C_6}{\partial \theta_1} & \frac{\partial C_6}{\partial \theta_2} & \frac{\partial C_6}{\partial \theta_3} \end{bmatrix} \begin{bmatrix} \partial P_x \\ \partial P_y \\ \partial P_z \\ \partial a \\ \partial b \\ \partial c \\ \partial \theta_1 \\ \partial \theta_2 \\ \partial \theta_3 \end{bmatrix} = \begin{bmatrix} 0 \\ 0 \\ 0 \\ 0 \\ 0 \\ 0 \end{bmatrix} \tag{8}$$

By the matrix partition, the Eq.(8) could be simplified as Eq.(9)

$$\begin{bmatrix} C_{q_d} & C_{q_i} \end{bmatrix} \begin{bmatrix} \partial q_d \\ \partial q_i \end{bmatrix} = \begin{bmatrix} 0 & 0 & 0 & 0 & 0 & 0 \end{bmatrix}^T \tag{9}$$

b. Lagrangian Formulation

By taking account of the kinetic and potential energy of end-effector, vertical bar and the parallelogram mechanism, the Lagrange function is obtained in Eq.(10):

$$L = K_P + K_V + K_C - U_P - U_V - U_C \tag{10}$$

where K_p and U_p represent the kinetic and potential energy of end-effector, K_v and U_v the kinetic and potential energy of vertical bar (slider of passive freedom included), K_c and U_c the kinetic and potential energy of parallelogram (slider base included).

Let the coordinates of end-effector be the redundant Lagrangian coordinates, the rotations of parallelogram be the independent coordinates, then the 6 Lagrangian multipliers are introduced as expressed in Eq.(11).

$$\lambda = \begin{bmatrix} \lambda_1 & \lambda_2 & \lambda_3 & \lambda_4 & \lambda_5 & \lambda_6 \end{bmatrix}^T \tag{11}$$

Let the first 6 Lagrangian equations of first type be associated with the end-effector coordinates, then a set of system dynamic equations can be written in the form:

$$C_{q_d}{}^T \lambda = \frac{d}{dt}\left(\frac{\partial L}{\partial \dot{Q}_d}\right) - \frac{\partial L}{\partial Q_d} - F_d \tag{12}$$

where

$$\frac{d}{dt}\left(\frac{\partial L}{\partial \dot{Q}_d}\right) = \begin{bmatrix} \frac{d}{dt}\left(\frac{\partial L}{\partial \dot{P}_x}\right) & \frac{d}{dt}\left(\frac{\partial L}{\partial \dot{P}_y}\right) & \frac{d}{dt}\left(\frac{\partial L}{\partial \dot{P}_z}\right) & \frac{d}{dt}\left(\frac{\partial L}{\partial \dot{a}}\right) & \frac{d}{dt}\left(\frac{\partial L}{\partial \dot{b}}\right) & \frac{d}{dt}\left(\frac{\partial L}{\partial \dot{c}}\right) \end{bmatrix}^T$$

, $\frac{\partial L}{\partial Q_d} = \begin{bmatrix} \frac{\partial L}{\partial P_x} & \frac{\partial L}{\partial P_y} & \frac{\partial L}{\partial P_z} & \frac{\partial L}{\partial a} & \frac{\partial L}{\partial b} & \frac{\partial L}{\partial c} \end{bmatrix}^T$, and $F_d = \begin{bmatrix} f_x & f_y & f_z & \tau_x & \tau_y & \tau_z \end{bmatrix}^T$

which presents the external force acting on the end-effector. When the position, velocity and acceleration of end-effector as well as the external forces are given, the values of Lagrangian

3

multipliers could be calculated by solving the linear equations described by Eq.(12).

Once the Lagrangian multipliers are found, the actuator torques in the driving joints of legs can be determined directly from the remaining Lagrangian equations. Specifically the second set of 3 Lagrangian equations for system dynamics could be written as the form:

$$F_i = \frac{d}{dt}\left(\frac{\partial L}{\partial \dot{Q}_i}\right) - \frac{\partial L}{\partial Q_i} - C_{q_i}{}^T \lambda \tag{13}$$

where $\frac{d}{dt}\left(\frac{\partial L}{\partial \dot{Q}_i}\right) = \left[\frac{d}{dt}\left(\frac{\partial L}{\partial \dot{\theta}_1}\right) \quad \frac{d}{dt}\left(\frac{\partial L}{\partial \dot{\theta}_2}\right) \quad \frac{d}{dt}\left(\frac{\partial L}{\partial \dot{\theta}_3}\right)\right]^T$, $\frac{\partial L}{\partial Q_i} = \left[\frac{\partial L}{\partial \theta_1} \quad \frac{\partial L}{\partial \theta_2} \quad \frac{\partial L}{\partial \theta_3}\right]^T$,

and $F_i = \begin{bmatrix} \tau_1 & \tau_2 & \tau_3 \end{bmatrix}^T$ which are the actuator torques needed from the servo motor.

3. CONTROL STRATEGY

After the dynamic model has been built up, the whole control simulation for CaPaMan is implemented by combining the Matlab SIMULINK and MSC_ADAMS environment, in which the control strategy is developed and running in the SIMULINK while the forward dynamics of parallel manipulator is calculated and presented by the ADAMS solver/viewer. The whole simulation architecture is presented by the Fig.3.
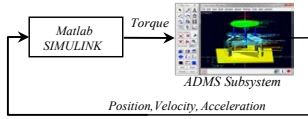

Figure 3. Simulation architecture

The 3D model of the parallel manipulator is developed in ADAMS, then the state variables, which are used for the interaction between SIMULINK and ADAMS/solver, of the model are exported to the SIMULINK as a module called ADAMS subsystem plant. By this way, both the advantages of mechanical dynamics behavior simulation in ADAMS and controller design in SIMULINK are utilized.

In order to obtain the good machining performance of parallel manipulator, the chatter vibration suppression is not the only objective for the control system design, but the trajectory precision is also an important factor. The control scheme for parallel manipulator in this paper consists of three parts as shown in Fig.4: I. feed forward model-based nonlinear control, II. feedback PV control and III. feed forward external disturbance depressing control.

Due to the highly nonlinear characteristic of dynamics in CaPaMan, it is difficult to get the satisfied tracking performance even without the external disturbance only by using the conventional PID controller with constant gains. In the paper, the model-based feed forward and the feedback PV control are combined to relatively simplify the nonlinearity of control system so as to get the stable tracking error.

Since the machining process in the end-effector would incur the severe disturbance load which would result in the serious chatter phenomenon in the manipulator, the inverse

dynamics based feed forward control is taken to cancel out any random extra load in the driving joints caused by the end-effector disturbance.
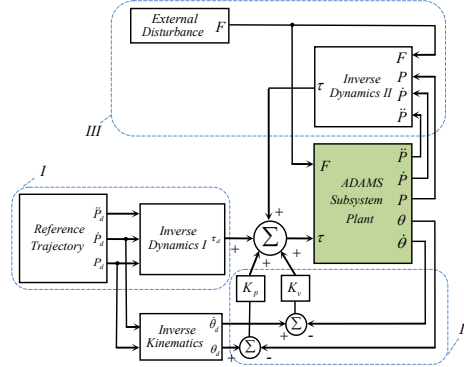

Figure 4. Control scheme: I. Feedforward model-based non-linear control, II. Feedback PV control, III. Feedforward disturbance depressing control

a. Model-based Nonlinear Control

For a general rigid body dynamics, an universal form could be given as the Eq.14.

$$\tau = M(\Theta)\ddot{\Theta} + V(\Theta,\dot{\Theta}) + G(\Theta) + F(\Theta,\dot{\Theta}) \tag{14}$$

where M is the nxn inertial matrix of manipulator, V an nx1 vector of centrifugal and Coriolis terms, and G an nx1 vector of gravity, F the friction of joints and external load.

By utilizing the linearizing and decoupling control law, the nonlinear control term $V(\Theta,\dot{\Theta}) + G(\Theta) + F(\Theta,\dot{\Theta})$ could be taken into control system to cancel out the nonlinearity in the dynamics model, which yields a linear second order system $f = M(\Theta)\ddot{\Theta}$ and an error model of control system $\ddot{E} + K_v\dot{E} + K_p E = 0$.

However for a parallel mechanism, due to the complicated kinematic coupling of joints, it is impossible to separate the term M from its dynamics model, the above mentioned linearizing law is not available. A revised model-based control is employed in this paper for CaPaMan control. Only take the part I and part II of control scheme in Fig.4 into consideration, the system equation could be written in the form:

$$M(\Theta_d)\ddot{\Theta}_d + V(\Theta_d,\dot{\Theta}_d) + G(\Theta_d) + F(\Theta_d,\dot{\Theta}_d) + K_v\dot{E} + K_p E \tag{15}$$
$$= M(\Theta)\ddot{\Theta} + V(\Theta,\dot{\Theta}) + G(\Theta) + F(\Theta,\dot{\Theta})$$

where $E = \Theta_d - \Theta$. By simplifying Eq.(15) under the assumptions $M(\Theta_d) \cong M(\Theta)$, $V(\Theta_d,\dot{\Theta}_d) \cong M(\Theta,\dot{\Theta})$, $G(\Theta_d) \cong G(\Theta)$ and $F(\Theta_d,\dot{\Theta}_d) \cong F(\Theta,\dot{\Theta})$, the error equation of system is found as Eq.(16).

$$\ddot{E} + M^{-1}(\Theta)K_v\dot{E} + M^{-1}(\Theta)K_p E = 0 \tag{16}$$

Clearly, the feed forward control doesn't provide complete nonlinearity decoupling, and the effective feedback gain changes while the configuration of the parallel manipulator changes. However a good set of constant gains can still been found to guarantee a reasonable damping performance of error.

4

b. Disturbance Depressing by Feed forward Control

While the parallel manipulator is used in the machining, the cutting force F could be deemed as a varying disturbance. By applying the feed forward control loop (control part III in Fig.4), then the compensation torque, which is used to cancel out the effect of F through the manipulator, is calculated based on the built up inverse dynamics model. The whole function diagram of the control scheme is presented in Fig.5.
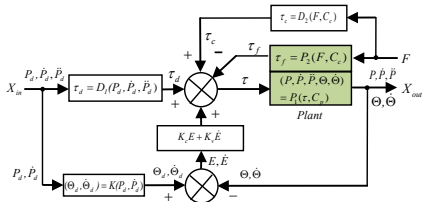

Figure 5. Implementation of control system

The plant consists of two parts: (1) for the P_1, the torques acting on the driving joints are taken as the input parameters of system function, while the position, velocity, and acceleration of end-effector and driving joints are regarded as the output, and it can be expressed by the Eq.(17)

$$(P,\dot{P},\ddot{P},\Theta,\dot{\Theta}) = P_1(\tau, C_p) \qquad (17)$$

where C_p is the configuration of manipulator from the previous calculation step; (2) for the P_2, the external load is taken as the input parameter while the causable effective torque in the driving joints is taken as the output of the system, which is expressed by the Eq.(18)

$$\tau_f = P_2(F, C_c) \qquad (18)$$

where C_c is the current manipulator configuration.

The actual acting torque on the driving joints are formed by the Eq.(19) as follows,

$$\tau = \tau_d + K_c E + K_v \dot{E} + (\tau_c - \tau_f) \qquad (19)$$

where $\tau_d = D_1(P_d, \dot{P}_d, \ddot{P}_d)$ is the torque calculated from reference trajectory, $K_c E + K_v \dot{E}$ the torque calculated from trajectory control error, $\tau_c = D_2(F, C_c)$ the torque used for compensation due to the external force. Substituting Eq.(19) into (17) yields

$$(P,\dot{P},\ddot{P},\Theta,\dot{\Theta}) = P_1((D_1 + K_c E + K_v E + (D_2 - P_2)), C_p) \qquad (20)$$

From Eq.(20), while established inverse dynamics model D_2 of parallel manipulator in control system approximates to P_2 in ADAMS, the difference between the compensation torque and the disturbing torque in the driving joints would approach to zero. Then the effect of the external load could be eliminated significantly or even completely.

4. RESULTS, CONCLUSION AND FUTURE WORK

Based on the proposed control strategy, while a reference trajectory of end-effector is given, which is shown as the Fig.6, several results are obtained and presented in this section.
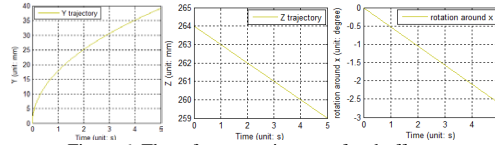
Figure 6. The reference trajectory of end-effector
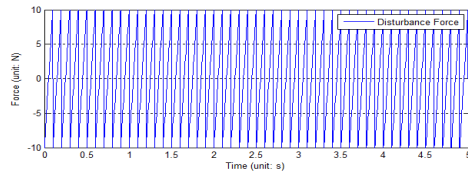
Figure 7. The external disturbance force of 10 Hz
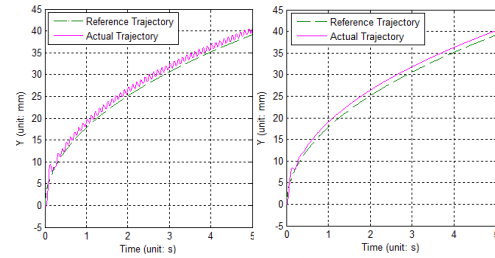
(a) Y trajectory without FDD   (b) Y trajectory with FDD
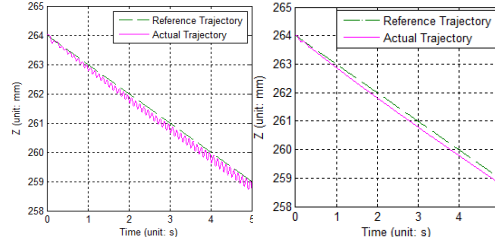
(c) Z trajectory without FDD   (b) Z trajectory with FDD
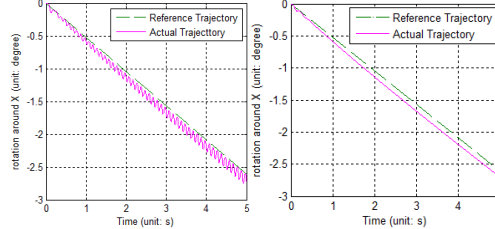
(e) AX rotation without FDD   (f) AX rotation with FDD

Figure 8 The comparison of the trajectory outputs with and without the feedforward control path for external disturbance depression under feed forward model-based control

In the given reference trajectory in Fig.6, the freedoms of end-effector keeps consistent and consists of translations along y and z axes and rotation around x axis.

The external disturbance force is simulated by a 10 Hz triangle wave with the amplitude of 10 N, as shown in Fig.7.

While the feed forward model-based control is applied, with/without the feed forward control path for the disturbance depression (FDD) in the control system, the outputs of obtained trajectories are as shown in Fig.8.

In the figures the dash blue line represents the reference trajectory and the continuous red line represents the actual obtained trajectory. From the Fig.8(a),(c),(e), it is clearly demonstrated that the chatter vibrations occurred in the same frequency of the external disturbance. However, from the results of Fig.8(b),(d),(f), two outcomes could be concluded: (1). the feedforward control for external disturbance depression applied in this paper is validated to be very effective based on the built up inverse dynamics model of the objective manipulator; (2). by the feed forward model-based control, a stable trajectory tracking error could be obtained for the highly nonlinear dynamic system.

Although a good result could be obtained by the software simulation in this paper, several difficulties are still open for us to apply this methodology into the practical application, and our future research would be on: (1) how to build up the theoretical dynamics model close to the actual manipulator? Such as the friction model, the deformation model as well as the inertial matrix identification need to be built up very accurately. As a solution, the intelligent algorithms such as the genetic algorithm, Markov Chain Monte Carlo method etc. would be applied to indentify the dynamics parameters of the parallel manipulator from its highly nonlinear model; (2) since the configuration of robot varies, how to obtain the robust PV gains becomes a very critical issue; (3) for the reference trajectory based control, several kinds of digital filter could be incorporated into the system to attenuate the vibration from the input, however the phase lagging phenomenon would occur to aggravate the control performance, how to utilized the zero phase lagging filter in the actual control system is also a promising research topic.

ACKNOWLEDGMENTS

REFERENCES

[1] Yongbo Wang, Novel methods for error modeling and parameter identification of a redundant serial-parallel hybrid robot, doctoral thesis, Lappeenranta university of technology, Finland, 2012.

[2] Andreas Pott, Manfred Hiller, Kinematic modeling, linearization and first-order error analysis, Parallel manipulators towards new applications, pp155-174, 2008.

[3] John J. Craig, Introduction to robotics mechanics & control, 3'rd edition, 2004.

[4] J.F.He. etc. A survey on control of parallel manipulator, Key engineering materials Vol.339 (2007), pp307-313.

[5] Marcel Honegger, Nolinear adaptive control of a dof parallel manipulator.

[6] O.A VIVAS, Ph. PHOGNET, Model based predictive control of a fully parallel robot, Symposium on robot control, Poland, 2003.

[7] Khalifa H. Harib etc. Parallel, serial and hybrid machine tool and robotics structures: comparative study on optimum kinematic designs, Serial and paralle robot manipulator - kinematics, dynamics, control and optimization, pp109-124, 2012.

[8] Yuehan Wan. etc. A survey on the parallel robot optimization, Second international symposium on intelligent information technology application, 2008.

[9] Ramazan Unal, Multi-criteria design optimization of parallel robots, IEEE Conf on robotic, automation and mechatronics, pp112-118, 2008.

[10] Ming Li, Huapeng Wu, Heikki Handroos, Stiffness-maximum trajectory planning of a hybrid kinematic-redundant robot machine, IECON2011, pp 283-288, 2011.

[11] KOTARO NAGAOKA, TOMONORI SATO, Feedforward controller for continuous path control of CNC machine tools, I.J of simulation, Vol.7, No.8, pp39-46.

[12] D.Econnomou etc. Robust vibration suppression in flexible payloads carried by robot manipulators using digital filtering of joint trajectories, Proceedings of the 200 international symposium on robotics and automation.

[13] HISASHI KATAOKA, Tracking control for industrial robot using notch filtering system with little phase error, Electrical Engineering in Japan, Vol. 175, No.1, 2011.

[14] F. Cus, U. Zuperl, J. Balic, Combined feedforward and feedback control of end milling system, Journal of achievements in materials and manufacturing engineering, Vol.45, pp 79-88, 2011.

[15] S. S. Abuthakeer etc. Prediction and control of cutting tool vibration in CNC lathe with anova and ann, International Journal of Lean Thinking, Vol.2, 2011.

[16] Christoph Henninger, An investigation of pose-dependent regenerative chatter for a parallel kinematic milling machine, 12th IFToMM world congress, 2007.

[17] Marco Ceccarelli, A new 3 D.O.F spatial parallel mechanism, Mech.Mach.Theory Vol. 32, No.8, pp895-902,1997.

Publication II

Ming Li, Huapeng Wu, Heikki Handroos
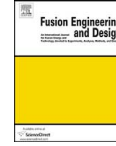
**Static stiffness modeling of a novel hybrid redundant robot machine**

Static stiffness modeling of a novel hybrid redundant robot machine

Ming Li*, Huapeng Wu, Heikki Handroos

Laboratory of Intelligent Machines, Lappeenranta University of Technology, Finland

ABSTRACT

This paper presents a modeling method to study the stiffness of a hybrid serial–parallel robot IWR (Inter-sector Welding Robot) for the assembly of ITER vacuum vessel. The stiffness matrix of the basic element in the robot is evaluated using matrix structural analysis (MSA); the stiffness of the parallel mechanism is investigated by taking account of the deformations of both hydraulic limbs and joints; the stiffness of the whole integrated robot is evaluated by employing the virtual joint method and the principle of virtual work. The obtained stiffness model of the hybrid robot is analytical and the deformation results of the robot workspace under certain external load are presented.

© 2011 Elsevier B.V. All rights reserved.

1. Introduction

The ITER vacuum vessel sectors are made of 60 mm-thick stainless steel which are joined together by the high efficiency structural and leak tight welds. The stringent tolerances of assembly, ±5 mm, are expected, while high dynamic machining force and high accuracy are required for cutting, weld repair and weld preparation. To satisfy the machining capacity of mobility and flexibility in a limited space inside the ITER vacuum vessel, a hybrid parallel robot (IWR in Fig. 1) has been developed, which has ten degrees of freedom (DOF); six degrees of freedom are contributed by a Stewart parallel mechanism and the rest by the serial mechanism [1].

Generally, in the high dynamic force application of assembly of ITER, the deflection of robot will be getting big and the accuracy will be getting poor. To compensate or to limit the deflection, the stiffness of robot should be studied. This paper focuses on the stiffness modeling of the robot. The developed model can be used for compensating the deflection of robot to reach high accuracy, and it can also be used for trajectory planning to find higher stiffness poses of the motion.

In this paper, a stiffness modeling method is developed for the proposed hybrid robot IWR. Based on this method, the matrix structural analysis (MSA) [2] approach is employed to calculate the stiffness of the basic element in the Stewart of robot, e.g., the universal joint (U-joint) and the bearing house; the virtual joint method (VJM) [3,4] combined with the principle of virtual work is also applied to evaluate the stiffness of the combined structure, e.g., the base of the Stewart; the stiffness of the Stewart is evaluated by taking account of the deformations of six base joints and the hydraulic limb deformations; the stiffness of the whole integrated robot is obtained by considering the Stewart and the serial basement as connected in serial.

The remainder of this paper is organized as follows: Section 2 introduces a general methodology of the MSA; Section 3 describes the modeling of the typical Stewart structure; Section 4 gives a finial stiffness model by integrating the parallel mechanism and the serial mechanism; Section 5 presents the numerical results of stiffness; and Section 6 summarizes the main contributions of this work.

2. Description of matrix structural analysis

The schematic representation of the kinematic chain of the IWR is presented in Fig. 2.

The coordinate $X_0^g Y_0^g Z_0^g$ is defined as the global frame, and all local coordinates are related to the global frame: $X_1^g Y_1^g Z_1^g$ moves along the gear track and $X_2^g Y_2^g Z_2^g$ along the ball screw; $X_3^g Y_3^g Z_3^g$ rotates around the Z_2^g axis; $X_4^g Y_4^g Z_4^g$ is the basement coordinate of the Stewart and rotates around the X_3^g axis; $X_5^g Y_5^g Z_5^g$ is fixed in the centre of the end-effector as the tool frame.

The analytical stiffness model of the basic element evaluated in this paper is based on MSA. In order to illustrate the application of the MSA on the multi-beam structure, the stiffness modeling of bearing house and U-joint in the base side of Stewart platform in the robot is taken into account (Fig. 3).

For simplification, the bearing house, U-joint and the base are described by the frame structure in Fig. 4.

For applying the MSA method we firstly define the elements of structure and their nodes. Each element of structure is defined by a number enclosed with a circle, and its two nodes by two numbers. A local coordinate is given for each element.

* Corresponding author at: CEID-Center, Lappeenranta University of Technology, Faculty of Technology, Skinnarilankatu 34, 53850 Lappeenranta, Finland. Tel.: +358 465941828.

E-mail address: hackingming@gmail.com (M. Li).
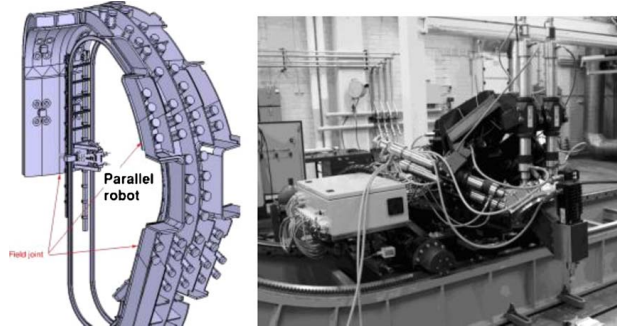
Fig. 1. 10DOF hybrid robot for the assembly of ITER: (i) vacuum vessel and (ii) robot used for the assembly of vacuum vessel.
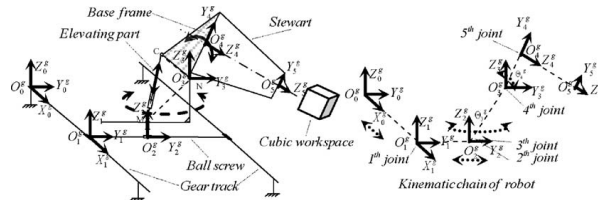
Fig. 2. Schematic diagram of hybrid robot.
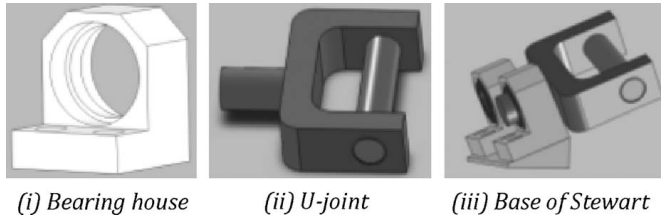
Fig. 3. Base of Stewart: (i) bearing house, (ii) U-joint, and (iii) base of Stewart.

In Fig. 4(iii), $O_0^b A$ is the base frame of Stewart platform, $O_1^u O_6^u$ the frame of U-joint, and ABO_1^u the frame of bearing house including the U-joint shaft. Firstly, we decompose the bearing house and the U-joint into separate beams in Fig. 4(i) and (ii), and then we obtain the stiffness matrix for each beam by applying the MSA. Finally all these stiffness matrices are assembled according to the node connectivity by the superposition principle and expressed in the local coordinate system. Herein, the stiffness modeling of U-joint is:

$$
\begin{bmatrix} F_1 \\ F_2 \\ F_3 \\ F_4 \\ F_5 \\ F_6 \end{bmatrix} = \begin{bmatrix} K_{11}^2 + K_{11}^7 & K_{12}^2 & K_{13}^3 & O & O & O \\ K_{21}^2 & K_{22}^2 + K_{22}^4 & O & K_{24}^4 & O & O \\ K_{31}^3 & O & K_{33}^3 + K_{33}^5 & O & K_{35}^5 & O \\ O & K_{42}^4 & O & K_{44}^4 + K_{44}^6 & O & K_{46}^6 \\ O & O & K_{53}^5 & O & K_{55}^5 + K_{55}^7 & K_{56}^7 \\ O & O & O & K_{64}^6 & K_{65}^7 & K_{66}^6 + K_{66}^7 \end{bmatrix} \begin{bmatrix} \Delta_1 \\ \Delta_2 \\ \Delta_3 \\ \Delta_4 \\ \Delta_5 \\ \Delta_6 \end{bmatrix}
\tag{1}
$$
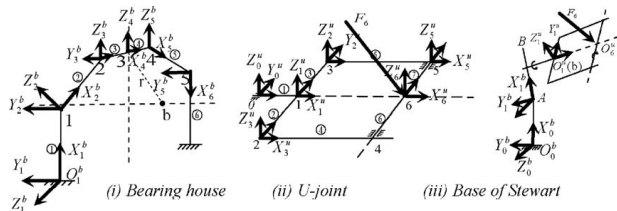
Fig. 4. Schematic diagram of frame structure: (i) bearing house, (ii) U-joint, and (iii) base of Stewart.
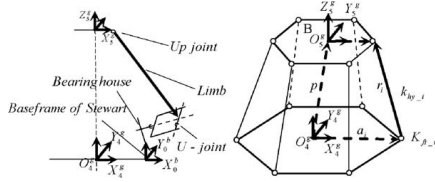
Fig. 5. Schematic diagram of the Stewart structure.
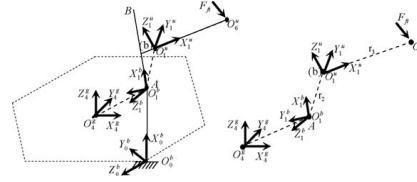
Fig. 6. Kinematic chain of the base in the Stewart.

where the 6×1 vector F_i is the external force exerting on node i, Δ the corresponding deformation of node i, O the $6 \times 6$ zero matrix and K_{ij}^n the 6×6 stiffness matrix of beam n. The deformation of beam 1 in the U-joint is not taken into account, because beam 1 (U-joint shaft) is assembled into the bearing house in the base and considered as rigid.

Eq. (1) was obtained assuming the whole structure of the U-joint is a frame. However, there are two rotational freedoms in the U-joint, and the external forces each are equal to zeros except the forces acting on node 0 and node 6. Therefore, by employing the static condensation technique, further simplification on Eq. (1) is obtained as

$$F_6 = (K_{22} - K_{21}K_{11}^{-1}K_{12})\Delta_6 \tag{2}$$

where K_{11} stands for the upper-left matrix block in Eq. (1), K_{12} the upper-right matrix block, K_{21} the lower-left matrix block and K_{22} the lower-right matrix block.

The force F_6 acting on node 6 is always constrained in the plane crossing the line $O_1^u O_6^u$ and perpendicular to the U-joint plane. Using the static condensation method and substituting the physical parameters of the U-joint into Eq. (2) gives:

$$F_u = K_u \times \Delta_u \tag{3}$$

where $F_u = [f_{u\_x} f_{u\_z}]^T$ and $\Delta_u = [d_{u\_x} d_{u\_z}]^T$ represent the external force and the corresponding deformation of node 6 in U-joint in the local frame $X_1^u Y_1^u Z_1^u$, and K_u is the 2×2 stiffness matrix of node 6 in the U-joint.

Similarly substituting the physical parameters of the bearing house, the stiffness of point b in the bearing house is formulated in the frame $X_1^b Y_1^b Z_1^b$ as follows

$$F_{bearh} = K_{bearh} \times \Delta_{bearh} \tag{4}$$

where $F_{bearh} = [f_{bearh\_y} f_{bearh\_z} m_{bearh\_x} m_{bearh\_x}]^T$ and $\Delta_{bearh} = [d_{bearh\_y} d_{bearh\_z} \theta_{bearh\_x} \theta_{bearh\_z}]^T$ represent the external force and the corresponding deformation in node b of the bearing house in frame $X_1^b Y_1^b Z_1^b$. The force f_{bearh_x} and the moment m_{bearh_y} are equal to zeros and suppressed in the equation since the force f_{bearh_x} acting on the base frame causes no deformation and the moment m_{bearh_y} does not exist around the axis of the bearing house.

3. Stiffness modeling of parallel mechanism

To evaluate the stiffness of the parallel mechanism, the parallel structure is decomposed into the basement frame, the bearing house in the base, the U-joint in the base, the hydraulic limb and the up joint in the end-effector (Fig. 5). The basement frame is considered as rigid structure. The bearing house and the U-joint form the base of Stewart platform, and each has configuration-independent stiffness, while the stiffness of the base of the Stewart platform is configuration-dependent as a function of the orientation of the hydraulic limb. The stiffness of the hydraulic limb is also configuration-dependent as a function of its length. The up-joint in the end-effector is considered as rigid.

3.1. Stiffness evaluation of base in parallel mechanism

The composition of the base by the bearing house and the U-joint is in a serial form. Herein, its stiffness is investigated by employing the virtual joint method and the principle of virtual work. The kinematic chain of the base is shown in Fig. 6.

The hexagon in the figure is the basement of the Stewart, in which the frame $X_4^g Y_4^g Z_4^g$ is defined as the local reference coordinate. Under the external force F_{ft} applied to the point O_6^u, the compliance of the base will cause the point O_6^u to experience a twist $\left[\Delta_{ft}^T \quad \Theta_{ft}^T \right]^T$ in terms of translational and rotational deformations in the frame $X_4^g Y_4^g Z_4^g$. Applying the kinematic relationship in the base results in:

$$\Delta_{ft} = J_{ft}[\begin{array}{cc} \Delta_u^T & \Delta_{bearh}^T \end{array}]^T,$$

$$J_{ft} = [\begin{array}{cccccc} J_{u\_dx} & J_{u\_dz} & J_{bearh\_dy} & J_{bearh\_dz} & J_{bearh\_\theta x} & J_{bearh\_\theta z} \end{array}] \tag{5}$$

where Δ_u and Δ_{bearh} represent the deformations of the U-joint and the bearing house while J_i is the Jacobian of the ith local joint deformation.

Employing the principle of virtual work in kinematic chain of the base leads to:

$$[\delta \Delta_{ft}^T][F_{ft}] = [\begin{array}{cc} \delta \Delta_u^T & \delta \Delta_{bearh}^T \end{array}] \begin{bmatrix} [K_u]_{2\times 2} & O_{2x4} \\ O_{4x2} & [K_{bearh}]_{4\times 4} \end{bmatrix} [\begin{array}{cc} \Delta_u^T & \Delta_{bearh}^T \end{array}]^T \tag{6}$$

where δ represents the virtual displacement of the deformations, K_u and K_{bearh} represent the stiffness matrices of the U-joint and the bearing house. Substituting Eq. (5) into Eq. (6) gives:

$$F_{ft} = K_{ft} \Delta_{ft} \tag{7}$$

$$K_{ft} = \left(J_{ft} \begin{bmatrix} K_u & O_{2\times 4} \\ O_{4\times 2} & K_{bearh} \end{bmatrix}^{-1} J_{ft}^T \right)^{-1} \tag{8}$$

For convenience, K_{ft_i} denotes the stiffness matrix of the ith base in the Stewart later on.

3.2. Stiffness of hydraulic limb

The assembly of components in the hydraulic limb is deemed to be serial, and the limb's stiffness varies with the cylinder stroke:

$$K_{hy} = \frac{A_1^2}{(A_1 x + V_h)/B_w + A_1 x/B_c + V_h/B_h} + \frac{A_2^2}{(A_2(l - x) + V_h)/B_w + A_2(l - x)/B_c + V_h/B_h} \tag{9}$$

where A is the area, V the volume, x the cylinder stroke, and l the cylinder length. B_w, B_c and B_h are the bulk modulus of water, cylinder and hose respectively. Subscripts 1 and 2 denote the corresponding chambers of the double-acting cylinder.
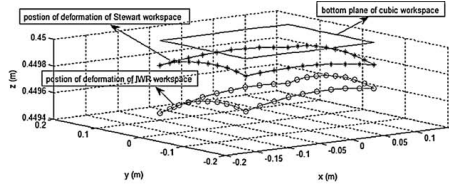
Fig. 7. Deformation of robot workspace: (i) on bottom plane of workspace; (ii) on top plane of workspace; (iii) on left plane of workspace; (iv) on right plane of workspace (v); on back plane of workspace (vi) and on front plane of workspace.
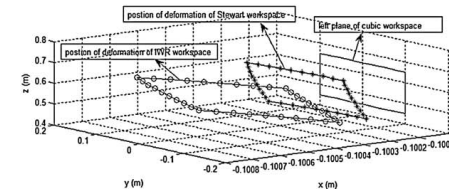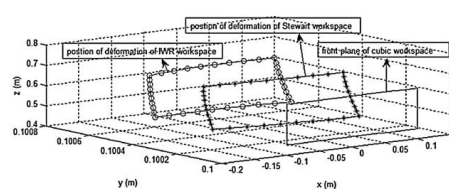
3.3. Stiffness evaluation of parallel mechanism

In Fig. 4, the coordinate frame $X_4^g Y_4^g Z_4^g$ is attached to the basement in the geometric centre. The coordinate frame B ($X_5^g Y_5^g Z_5^g$) is attached to the moving platform, and its origin is located at the mass centre. Taking account of the deformations in the six base joints and hydraulic limbs, the stiffness matrix of the parallel mechanism is obtained in the same way achieving Eq. (8)

$$K_{stw} = (J_{stw}[diag[K_{li}]]^{-1} J_{stw}^T)^{-1} \qquad (10)$$

where J_{stw} is the Jacobian matrix of the Stewart, and $K_{li} = diag[K_{hy\_i} K_{ft\_i}]$.

4. Stiffness modeling of hybrid robot

The hybrid robot (Fig. 2) is composed of the Stewart, the elevating part and the track basement. Through the mechanism analysis, the elevating part is considered as a crank-slider mechanism: the base frame of Stewart platform is regarded as the crank while the hydraulic limb is the actuator of the mechanism. The stiffness of the actuator is transformed into the local compliant spring located at the crank joint O_3^g and denoted by $k_{\theta 4}$. The stiffness of the gear pair in the track is denoted by k_{x1}. The rotation around Z_2^g axis is driven by an epicycle gear, and its stiffness is denoted by $k_{\theta 3}$. The stiffness of the ball screw, k_{y2}, is the sum of the nut stiffness and the shaft stiffness.

Analyzing the kinematics of the robot results in:

$$[\,\Delta_5^{g^T} \quad \Theta_5^{g^T}\,]^T = J\Delta_q \qquad (11)$$

where $[\,\Delta_5^{g^T} \quad \Theta_5^{g^T}\,]^T$ is the deformation of end-effector, J the Jacobian matrix of the robot, and Δ_q the deformation vector of all joints $\Delta_q = [\,\Delta_5^T \quad \Theta_5^T \quad d_{\theta 4} \quad d_{\theta 3} \quad d_{y2} \quad d_{x1}\,]^T$.

Employing the principle of virtual work on the hybrid robot joints leads to:

$$C = J\chi^{-1}J^T \qquad (12)$$

where C is the 6×6 compliance matrix of the whole hybrid robot, and $\chi = diag[K_{stw} \; k_{\theta 4} \; k_{\theta 3} \; k_{y2} \; k_{x1}]$ is a 10×10 diagonal matrix of the stiffness of all joints. The stiffness of the whole hybrid robot is obtained as the inverse of the compliance matrix: $K = C^{-1}$.

5. Numerical evaluation results

Based on the above model, the deformations of some certain workspace are investigated under the external loads. One example is given for demonstration. The work space of the end-effector was a 200 mm × 200 mm × 200 mm cube (Fig. 2); the end-effector frame has no rotation with respect to the basement frame of the Stewart. The robot worked along the borders of the workspace and the external load of 5 kN was vertical to the Stewart basement. The deformations are illustrated in Fig. 7.

Due to the redundant freedom in the robot, the configuration of the serial part in the robot is pre-determined, while the cubic workspace is reached by the Stewart.

In Fig. 7, the continuous line denotes the borders of the ideal work plane in the cubic workspace without load; the star-line denotes the border positions of Stewart cubic workspace after the deformations, assuming the serial part in the robot to be rigid; the circle-line denotes the border positions of the end-effector workspace after the deformations, taking into account both the stiffness of the Stewart and the serial part of the robot.

By analyzing the data obtained from the stiffness of the robot, it is testified that the deformations of the robot are mainly contributed by the hydraulic limbs in the Stewart and the hydraulic driver in the elevating component of the serial part of IWR. However, all these deformations of hydraulics could be compensated by the closed-form controller in the robot.

6. Conclusions

This paper presents a stiffness modeling method for a hybrid robot machine. In the built model, all the deformations of the base joints in the Stewart platform are taken into account. By applying the MSA, the VJM and the principle of virtual work, the analytical stiffness of the robot can be achieved, and the final numerical results have verified that the model is valid and one advantage of the model is the low calculation consumption.

References

[1] H. Wu, P. Pessi, H. Handroos, Assembling and repairing for ITER vacuum vessel with mobile parallel robot, Fusion Engineering (2007).
[2] D. Deblaise, X. Hernot, P. Maurine, A systematic analytical method for PKM stiffness matrix calculation, in: Proceedings of the IEEE International Conference on Robotics and Automation, Orlando, FL, May, 2006.
[3] C.M. Gosselin, D. Zhang, Stiffness analysis of parallel mechanisms using a lumped model, International Journal of Robotics and Automation 17 (1) (2002) 17–27.
[4] A. Pashkevich, D. Chablat, P. Wenger, Stiffness Analysis of Overconstrained Parallel Manipulators, Journal of Mechanism and Machine Theory 44 (5) (2009).

Publication III

Huapeng Wu, Yongbo Wang, Ming Li, Mazin Al-Saedi, Heikki Handroos

Chatter suppression methods of a robot machine for ITER vacuum vessel assembly and maintenance

Chatter suppression methods of a robot machine for ITER vacuum vessel assembly and maintenance

Huapeng Wu, Yongbo Wang*, Ming Li, Mazin Al-Saedi, Heikki Handroos

Laboratory of Intelligent Machines, Lappeenranta University of Technology, FIN-53851 Lappeenranta, Finland

HIGHLIGHTS

- A redundant 10-DOF serial-parallel hybrid robot for ITER assembly and maintains is presented.
- A dynamic model of the robot is developed.
- A feedback and feedforward controller is presented to suppress machining vibration of the robot.

ARTICLE INFO

ABSTRACT

In the process of assembly and maintenance of ITER vacuum vessel (ITER VV), various machining tasks including threading, milling, welding-defects cutting and flexible hose boring are required to be performed from inside of ITER VV by on-site machining tools. Robot machine is a promising option for these tasks, but great chatter (machine vibration) would happen in the machining process. The chatter vibration will deteriorate the robot accuracy and surface quality, and even cause some damages on the end-effector tools and the robot structure itself. This paper introduces two vibration control methods, one is passive and another is active vibration control. For the passive vibration control, a parallel mechanism is presented to increase the stiffness of robot machine; for the active vibration control, a hybrid control method combining feedforward controller and nonlinear feedback controller is introduced for chatter suppression. A dynamic model and its chatter vibration phenomena of a hybrid robot is demonstrated. Simulation results are given based on the proposed hybrid robot machine which is developed for the ITER VV assembly and maintenance.

© 2014 Elsevier B.V. All rights reserved.

1. Background

The assembly and maintenance of ITER vacuum vessel (ITER VV) involves lots of machining operations, such as boring, threading, milling and drilling. These operations need to be carried out from inside of ITER VV. Commercially available CNC machining center cannot be used for this purpose due to its big size and high weight. Furthermore, the general industrial robot cannot be used due to its poor stiffness in the heavy duty machining process. Therefore, one of the most suitable options should be a light weight mobile robot which has the ability of moving around inside of VV and performing different machining tasks by replacing different cutting tools. Some special heavy duty robots have been designed by other research groups for the application of transporting heavy parts of ITER VV, but very few of them can be used to carry out machining tasks. During the machining process, the main issue would be the chatter vibration since it will cause not only bad accuracy and surface quality but also some damages on the tool and even the robot structures. Consequently, it is important to investigate the mechanism of chatter vibration and find a way to suppress it.

The investigation of vibration control on flexible manipulators and mechanisms has been conducted by many researchers over several decades [1–4]. Generally, it can be divided into two categories, one is passive vibration control and another is active vibration control. The passive vibration control has three types: (i) the mechanism itself has superior damping characteristics and higher stiffness to weight ratios; (ii) the vibration of the mechanism is dissipated by introducing additional damping materials; and (iii) the vibration of the mechanism is attenuated through optimizing the cross-sectional geometry of the mechanism links [1–3]. The active vibration control, probably the most effective method for suppressing vibrations of a robot, has been investigated by several

* Corresponding author. Tel.: +358 5 6212462; fax: +358 5 6212499.
*E-mail addresses:* yongbo.wang@lut.fi, yongbo.wang@hotmail.com (Y. Wang).
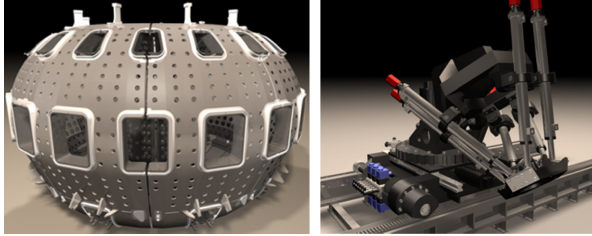
Fig. 1. Mock-up of ITER VV and CAD model of the hybrid robot.

researchers [5–7]. This paper studies both passive and active methods for the vibration control of a hybrid robot [11], which is developed in Lappeenranta University of Technology (LUT) in Finland.

The hybrid robot (Fig. 1) is an inter-sector welding/cutting robot, which is used for the ITER VV assembly and maintenance. This redundant serial-parallel hybrid robot consists of two relatively independent sub-structures: the front-end part is a hexapod parallel mechanism driven by six water hydraulic cylinders which can provide full six degrees of freedom (DOF) to the end-effector; the second part is a serial multi-link mechanism which can support the parallel mechanism and provide four additional redundant degrees of freedom.

For the passive vibration control method, the hexapod parallel mechanism is considered since it can provide not only a relatively high stiffness to weight ratios but also a high position accuracy which is required in the processes of milling, welding and transporting materials, etc.

For the active control method, a hybrid robust controller is considered. It is well believed that the stiffness and the dynamic behavior of parallel robot should be better than that of serial robot but lower than that of CNC machine. However, in real applications, the parallel robot has not been widely used. One of the major hurdles to prevent the adoption of parallel manipulator for machining purposes lies in the chatter vibration. Consequently, it has to be eliminated or suppressed in a high-accuracy-requirement machining process. Based on the controller architectures, the active vibration control algorithm can be categorized into three types: feedforward, feedback, and hybrid controller. To improve the quality of the mentioned active methods, one of the solutions is to add some fast and high accuracy motion actuators (e.g. Piezo-ceramic actuator) or micro manipulators. These actuators can be integrated within a link or on the end-effector of the manipulator. On their integrated spot they can limit or eliminate the residual elastic oscillation [5–9]. But one drawback of this method is that the additional actuators and their accessories are required, therefore, it may not be a cost-effective solution from the economical perspective. Furthermore, the chatter vibration is subject to occur in the continuous motion, while the residual vibration is liable to happen in the point-to-point motion. The residual vibration in point-to-point process can be predicted and eliminated easily than the chatter vibration in machining process. Currently most of the vibration suppression methods have focused on the residual vibration suppression rather than the continuous path control for chatter suppression [10]. This paper will concentrate on the continuous path control to suppress the chatter vibration.

To limit the chatter vibration of the proposed hybrid robot, this paper first studies the dynamics of the robot imposed with machining force, and then presents a hybrid control algorithm for suppressing chatter by using nonlinear feedback technique and feedforward control method.

2. Dynamic analysis

The kinematics of the hybrid robot is shown in Fig. 2. A nonlinear dynamic model of the robot can be written as Eq. (1):

$$\tau = D(q)\ddot{q} + H(q, \dot{q}) + K(q)q + G(q), \quad q = [y, x_1, x_2, \ldots, q_1, q_2, \ldots]^T,$$
$$\tau = [0, F_1, F_2, \ldots, \tau_1, \tau_2, \ldots]^T \tag{1}$$

where y is the generalized coordinates of the end-effector; x_1, x_2, the prismatic displacements of parallel structure limbs; q_1, q_2, the prismatic and revolute displacements of serial structure joints; F_1, F_2, the forces applied to the limbs of parallel mechanism; τ_1, τ_2, the forces and torques applied to joints of serial mechanism; D the inertial matrix of all robot mechanical links; H the matrix in terms of damping, centrifugal and Coriolis coefficients; K the stiffness matrix of joint links and G the gravity matrix.
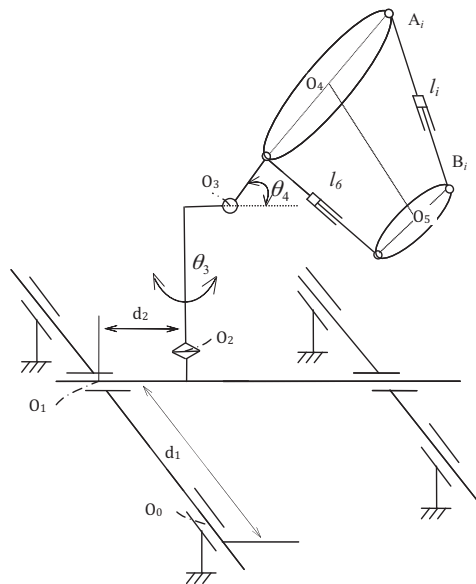

Fig. 2. Kinematics of the hybrid robot (d_1, d_2, θ_3 and θ_4 are prismatic and revolute joints of the serial mechanism; l_1 to l_6 are prismatic joints of the parallel mechanism).
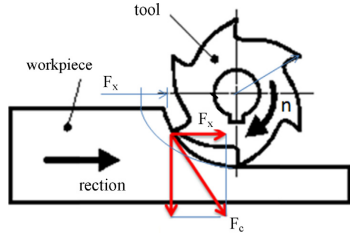
Fig. 3. Cutting force.

The dynamic model of the hybrid manipulator can be further divided into two sub-dynamic models by taking the external force into account. For serial mechanism it can be expressed as:

$$\tau_s = D_s(q_s)\ddot{q}_s + H_s(q_s, \dot{q}_s) + K_s(q_s)q_s + G_s(q_s) + f_{ps}, \quad (2)$$

and for parallel mechanism it can be written as:

$$\tau_p = D_p(q_p)\ddot{q}_p + H_p(q_p, \dot{q}_p) + K_p(q_p)q_p + G_p(q_p) + f_{ep}, \quad (3)$$

where q_s is the generalized coordinates of the serial mechanism; q_p is the generalized coordinates of the parallel mechanism; f_{ps} is the force of parallel mechanism acting on the serial mechanism at point O_4; and f_{ep} is the external force acting at point O_5 of the end-effector of parallel mechanism.

If the serial mechanism of the hybrid robot is fixed to a certain configuration during the machining process, then only the parallel manipulator contributes to motion. Consequently the dynamics of serial mechanism can be neglected and the dynamics of parallel mechanism dominates the vibrations.

3. Machining force

The milling process is shown in Fig. 3.

The machining force can be expressed as

$$F_c = k_c \sum_{i=1}^{m} (f_x \sin(\omega t + \delta\theta_i) + \sqrt{f_x \sin(\omega t + \delta\theta_i) + R^2 - f_z^2}) - R)a_p, \quad (4)$$

where k_c is machining constant; a_p the cutting depth; f_x the feeding rate; ω the cutting frequency; R the tool radius.

The dominated parameters in dynamic cutting force are feeding speed, cutting depth, cutting speed and the number of teeth z. Because of the work-hardening capability and low thermal conductivity of stainless steel (austenitic), the cutting speed cannot be very high. The cutting frequency is mainly determined by the tool rotation speed and the number of teeth. Here an off-the-shelf disk milling cutter is chosen for testing: the tool radius $R = 100$ mm; the number of teeth $z = 51$. The cutting parameters are as follows: feeding speed is 85 mm/min, cutting depth 10 mm, rotation speed 60 rpm. Fig. 4 shows the dynamic machining force. The frequency of the cutting force is about 51 Hz. However, when reduce the cutter teeth number or the rotation speed, the frequency of the cutting force will increase accordingly.

4. Chatter analysis

Regenerative chatter is a self-excited vibration in machining operation, and it is the consequence of interference of wavy surface generated between current machining pass and previous machining passes. All self-excited chatter analysis techniques are started with the development of a force model for machining process and a dynamic model for machine tool workpiece structure [11], and
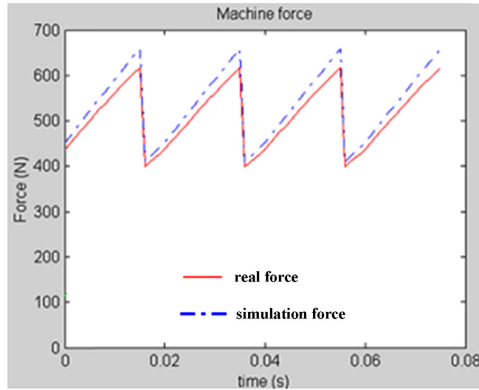

Fig. 4. Calculated cutting force.

then the two models are combined together to form a closed-loop dynamic model for a machining operation. By mounting a workpiece on strong steel table (e.g. the ITER VV), the structure of the workpiece can be regarded as relatively stiff, and its deformation can be ignored in the analysis since its stiffness is much larger than that of robot-tool structure. Typically, the self-excited chatter frequency of a robot is slightly larger than its natural vibration frequency.

Generally, the dynamic model of a robot system can be formulated from Eqs. (2) and (3) as:

$$\tau = D(q)\ddot{q} + H(q, \dot{q}) + C(q) + F_c, \quad (5)$$

where q is the vector of general coordinates of actuators.

The stability of the system depends on the eigenvalues of the above equations. The dynamic model of the robot contains nonlinear items from coupling structures of the parallel mechanism, the traditional linear control method will be difficult to achieve required performance, thus a robust controller need to be considered.

5. Controller design

The control strategy of chatter suppression is developed by using a hybrid controller combining state feedback controller and adaptive feedforward controller. The feedback controller can achieve promising position accuracy when the dynamics of whole robot machine is linearized. To suppress the chatter vibration, feedforward controller can significantly eliminated the external disturbance based on the inverse dynamics of robot machine whenever a disturbance signal is available [10]. Nevertheless, a tracking error will increase due to the delay of feedforward, therefore, a critical task in the future research is to minimize its phase lag effect. Fig. 5 shows the hybrid control strategy.
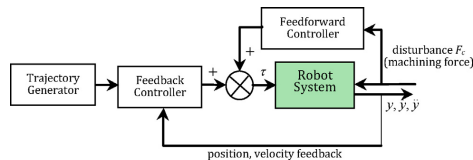

Fig. 5. Hybrid control strategy.
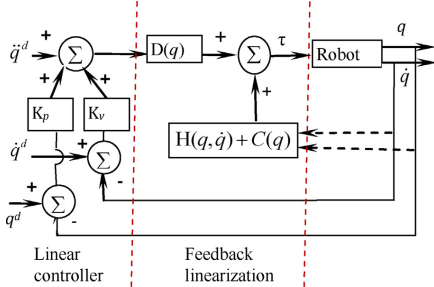
Fig. 6. Feedback linearization control.
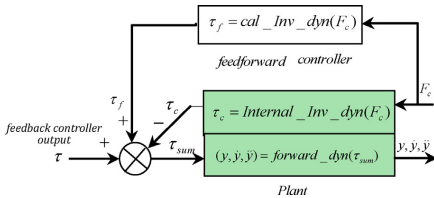
Fig. 7. Feedforward control.

5.1. Feedback linearization

To linearize the dynamic model Eq. (5), feedback linearization technique is applied to the state feedback controller (Fig. 6) by introducing

$$\begin{cases} \tau = \alpha f + \beta \\ \alpha = D(q) \\ \beta = H(q, \dot{q}) + C(q) \end{cases} \tag{6}$$

then the linearized dynamic model of Eq. (5) (without the external force F_c) becomes

$$f = \ddot{q} \tag{7}$$

and the linear control law in Fig. 6 can be written as

$$f^d = \ddot{q}^d + k_v(\dot{q}^d - \dot{q}) + k_p(q^d - q) \tag{8}$$

By combining Eqs. (7) and (8), the characteristic equation of this linear controller can be written as

$$(\ddot{q}^d - \ddot{q}) + k_v(\dot{q}^d - \dot{q}) + k_p(q^d - q) = 0 \tag{9}$$

5.2. Feedforward controller

Compared to a single feedback controller, the hybrid control strategy combining the feedback and feedforward controllers can significantly improve the performance of a robot whenever a coupled disturbance is available, since the feedforwad controller can completely eliminate the effect of measured disturbance on the system. The machining force, which is deemed as the external disturbance herein, can be calculated from the measurement of a 3D acceleration sensor mounted on the machine header. Then the machining force is manipulated by an inverse dynamic model and fed forward to the output of feedback controller as illustrated in Fig. 7.

If without the external disturbance, which is the varying cutting force F_c, the robot end-effector reference trajectory y, $\dot{y}$, $\ddot{y}$ could be obtained by applying the driving torques τ in the actuators, which is
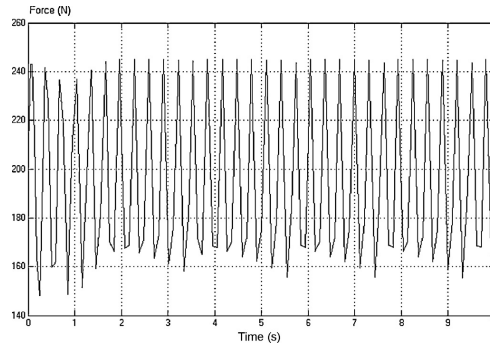

Fig. 8. Machining force in lower frequency.
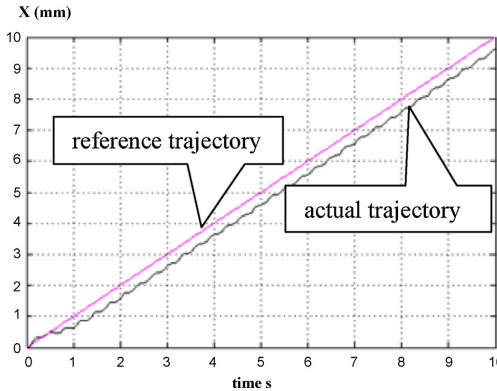

Fig. 9. Result of feedback controller.
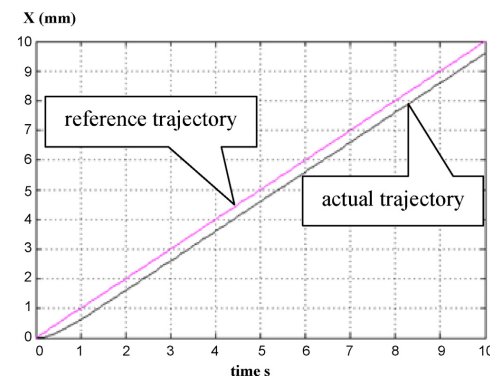

Fig. 10. Result of feedback–feedforward controller.
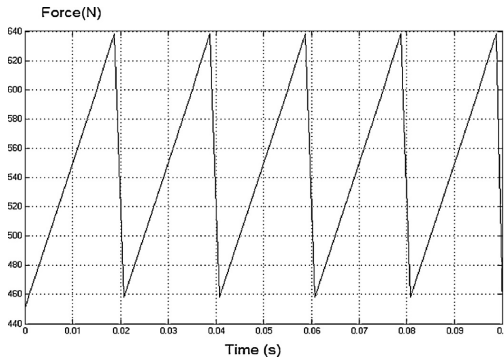
Fig. 11. Machining force in high frequency.

Fig. 13. Result of feedback–feedforward controller (High frequency).

calculated by the feedback position-velocity (PV) controller as well as the feedback linearization as shown in Fig. 6. Then the forward dynamics of the end-effector is expressed by Eq. (10):

$$(y, \dot{y}, \ddot{y}) = forward\_dyn(\tau) \tag{10}$$

Whenever the disturbance (cutting force) is applied to the end-effector of robot system, the corresponding joints disturbance τ_c is yielded from the internal inverse dynamics of the robot system, which will cause the actual trajectory be deviated from the reference. However, by applying the feedforward controller from the cutting force, the compensation torque τ_f can be produced, and the actual torque acting on the driving joints can be expressed as:

$$\tau_{sum} = \tau + (\tau_f - \tau_c) \tag{11}$$

While the inverse dynamics of the robot system is built accurately in the feedforward controller, then the feedforward output τ_f equals the joints disturbance τ_c, consequently the causative disturbance on the robot driving joints due to the external cutting force would be eliminated completely, and the chatter vibration phenomenon of end-effector also vanishes.

5.3. Simulation results

To evaluate the algorithm, a one degree-of-freedom disturbance force with a frequency closes to the robot natural vibration


**Fig. 12.** Result of feedback controller (High frequency force).

frequency is applied to the system as shown in Fig. 8. For the feedback control without feedforward, the output of control system vibrates as shown in Fig. 9. However, the vibration can be eliminated (Fig. 10) when the feedforward path is introduced, regardless of any frequency change in the disturbance force. If the force frequency is changed to be much higher (0.1 s period shown in Fig. 11) than the nature frequency of robot, then the chatter will not happen even without a feedforward path. Therefore, there is no difference between the feedback controller and feedback–feedforward controller as seen in Figs. 12 and 13. A feedback controller is easy to be built up in simulation as the parameters of the studied dynamic model are known. However, the performance of feedforward controller may not be as sound as the simulations results in a real system since the parameter errors may occur and acceleration sensor signals may have a delay.

6. Conclusion

In ITER VV assembly and maintenance, lots of machining tasks need to be carried out by on-site robot machine. Chatter vibration will be inevitable during the machining process when using a low stiffness robot. The vibration would deteriorate surface quality and even cause some damages to the robot system. To suppress the vibration, dynamic models of a hybrid robot with machining force were developed and a hybrid controller was studied. According to the simulation results, the vibration can be eliminated by employing a hybrid controller which combines feedforward and feedback controller. The experimental validation of the control algorithm for a real robot will be carried out in near future.

References

[1] M.O. Tokhi, A.K.M. Azad, Control of flexible manipulator systems, Proc. IMechE I: J. Syst. Control Eng. 210 (1996) 283–292.
[2] A. Preumont, Vibration Control of Active Structures: An Introduction, Kluwer Academic Publishers, Dordrecht, 2002.
[3] R.L. Clark, W.R. Saunders, Adaptive Structure: Dynamics and Control, John Wiley & Sons, New York, 1998.
[4] S.K. Tsoa, T.W. Yangb, W.L. Xuc, Z.Q. Sun, Vibration control for a flexible-link robot arm with defection feedback, Int. J. Non-Linear Mech. 38 (2003) 51–62.
[5] X. Zhang, J.K. Mills, W.L. Cleghorn, Flexible linkage structural vibration control on a 3-PRR planar parallel manipulator: experimental results, Proc. IMechE I: J. Syst. Control Eng. 223 (2009).
[6] A. Sharon, N. Hogan, D.E. Hardt, The micro manipulator: an improved architecture for robot control, Robotics Comput. Integrated Manufact. 10 (3) (1993) 209–222.
[7] K. Nagaoka, T. Sato, Feedforward controller for continuous path control of CNC Machine Tools[J]. Advanced Technology R&D Center, Mitsubishi Electric Corporation8-1-1 Tsukaguchihonmachi, Amagasaki, Hyogo, 2006: 661-8661.

[8] G. Pan, H. Xu, C.M. Kwan, C. Liang, L. Haynes, Z. Geng, Modeling and intelligent chatter control strategies for a lathe machine, Control Eng. Pract. 4 (12) (1996) 1647–1658.

[9] S. Kumagai, K. Ohishi, N. Shimada, High-performance robot motion control based on zero-phase notch filter for industrial robot, in: IEEE International Workshop on Advanced Motion Control, March 21–24, Nagaoka, Japan, 2010.

[10] Y. Wang, P. Pessi, H. Wu, H. Handroos, Accuracy analysis of hybrid parallel robot for the assembling of ITER, Fusion Eng. Des. June (2009).

[11] Z. Pan, H. Zhang, Analysis and suppression of chatter in robotic machining, in: Process International Conference on Control, Automation and Systems, October 17–20, 2007 in COEX, Seoul, Korea, 2007.

Publication IV

Ming Li, Huapeng Wu, Heikki Handroos

Stiffness-maximum trajectory planning of a hybrid kinematic-redundant robot machine

Stiffness-Maximum Trajectory Planning of a Hybrid Kinematic-Redundant Robot Machine

Ming Li, Huapeng Wu, Heikki Handroos
Laboratory of Intelligent Machines, Lappeenranta University of Technology, Finland
Ming.Li@lut.fi

Abstract-The paper presents an approach for the trajectory planning of a hybrid serial-parallel redundant robot by investigating the best stiffness performance. The robot under study has 10 degrees of freedom (DOF); six DOF are contributed by a parallel mechanism, and four DOF from serial-link carriage. Due to these redundant degree freedoms, the robot body configuration is under constrained even when the position and orientation of the end-effector has been fixed. In this case, the stiffness of robot varies in all the possible joints configurations. When the path of the end-effector has been prescribed, the robot body configuration can be dominated by taking into account of the stiffness of robot, i.e. among of all the possible configurations, the joints take a value when the stiffness of robot reaches maximum. To solve the stiffness optimization problem differential evolution (DE) algorithm is employed. In the paper the stiffness model as an object function has been built. The evaluation results demonstrate that the DE is an effective method for searching joints parameters in optimum stiffness, and the results with respect to the optimum stiffness show that the joints trajectory planning is feasible for the robot control.

I. INTRODUCTION

The hybrid kinematic redundant robot machine under study is developed to carry out welding, machining and remote handling for the assembly of vacuum vessel (VV) of ITER (International Thermonuclear Experimental Reactor) which consists of nine sectors made of 60mm thick stainless steel (Fig. 1) [1]. In order to join two adjacent sectors together by continuous welding, the robot has the ability to work along the track mounted on the inner surface of VV sector and can provide full six degrees of freedom in task space by end-effector tool bit. Because of great machining force and heavy E-beam gun, the robot is demanded to possess high stiffness performance while the stringent accuracy tolerances of assembly, ±5mm, are expected. To satisfy all these special requirements, a hybrid kinematic redundant robot is built which possesses 10 degrees of freedom (DOF) (Fig.1). The robot consists of two sub-structures — the Stewart-platform-based parallel mechanism driven by six water hydraulic cylinders contributes the full six degrees of freedom for the end-effector; the H-driven carriage with two rotating motions offers additional four degrees of freedom to the robot. For the H-driven carriage, the motion along the track is driven by a pair of motors with pinion; the motion perpendicular to the track is driven by the ball screw; the rotation table rotates

1. Carriage base   2. Ball screw   3. Rotation table   4. Support frame   5. Stewart base
6. End-effector   7. track motor with pinion   8. Rotation drive motor   9. Tip drive cylinder   10 Stewart drive cylinder   11 Hybrid robot   12 Gear track   13 Vacuum vessel sector
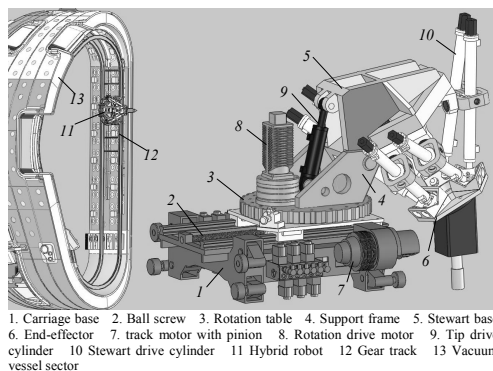
Fig. 1. 10DOF hybrid robot for assembly of ITER: (i) vacuum vessel sector and (ii) robot used for the assembly of vessel.

around the direction vertical to the carriage plane; the Stewart base is tipped by another water hydraulic cylinder.

Although plenty of research works have been done on the parallel mechanism, the acceptance of parallel robot by the industry as manufacturing equipment is quite slow. One of the major reasons is the small workspace, and another is that the stiffness of parallel mechanism varies in different configurations and even is rather weak near the edge of the workspace constrained by kinematic-bounded posture [2] - [4]. Regard to this hybrid serial-parallel robot, the workspace has been relatively enlarged, but the stiffness performance is dominated not only by the parallel mechanism but also by the serial system. Based on this point, the stiffness performance of the hybrid robot needs to be investigated intensively so as to guarantee the better machining performance.

For this hybrid robot, the kinematic redundancy occurs since the 10DOF possessed by the robot is more than the demanded (6DOF) in the task space. Hereby, the four degrees of freedom contributed by the carriage base are referred to the redundant driving joints. Consequently, during the robot control process the joints trajectory admits an infinite number of solutions even while the path of end-effector is prescribed. Meanwhile, the stiffness varies depending on the robot body configuration determined by the joints trajectory. This paper presents a stiffness-maximum-based trajectory planning for such hybrid kinematic redundant robot machine in the joint space. The objective of this work is to provide an optimal joints trajectory such that it offers the best stiffness

performance while the end-effector tool moves along a prescribed path.

In this paper, the analytical stiffness model of the hybrid robot is derived and the minimum eigenvalue of the stiffness matrix is preferred to be the reasonable index to evaluate the stiffness performance. It is found that the stiffness is restricted in between the minimum and maximum eigenvalues of the stiffness matrix [5]. In order to get the better stiffness performance, we should get the larger index value. When the position and orientation of end-effector is fixed, the stiffness varies over the underconstrained body configuration dominated by redundant joints. In the particular robot body configuration when the index value is maximum, the stiffness performance is better than the one in any other configurations, the robot is then regarded to hold the best stiffness performance. Hence, the objective function for optimizing stiffness is subject to maximum index values. The DE is proposed for searching the input parameters of the redundant joints, while the position and orientation of the end-effector has been fixed.

The remainder paper is organized as follows: Section 2 describes the stiffness modeling of such a redundant freedom robot machine; Sections 3 discusses the most suitable stiffness performance index by analyzing the stiffness matrix characteristics; Section 4 demonstrates the application of DE and presents the best stiffness surface in a 200x200mm^2 Cartesian workspace; Section 5 presents the example of the joints trajectory of hybrid robot subject to the best stiffness along a straight line path of end-effector within the 200x200mm^2 workspace.

II. STIFFNESS MODELING OF HYBRID SERIAL-PARALLEL ROBOT

Since the robot consists of parallel mechanism and serial mechanism in a serial manner, the Stewart structure can be deemed as a lumped virtual link in view of serial robot, and the stiffness of hybrid robot can be derived by taking account of the serial joints compliance.

The schematic diagram of the hybrid robot is presented in Fig. 2.

The coordinate $X_0^g Y_0^g Z_0^g$ is defined as the global frame, located at a fixed point on the gear track, and all other local coordinates are related to the global frame. $X_1^g Y_1^g Z_1^g$ is fixed on the carriage base and can move along the gear track; $X_2^g Y_2^g Z_2^g$ is fixed on the screw nut and moves along the ball screw; $X_3^g Y_3^g Z_3^g$ is fixed on the support frame, and rotates around the Z_2^g axis driven by the motor on the rotation table; $X_4^g Y_4^g Z_4^g$ is the coordinate of the Stewart base and rotates around the X_3^g axis driven by the elevating part (crank-slider mechanism); $X_5^g Y_5^g Z_5^g$ is fixed at the center of the end-effector as the tool frame.

### A. Stiffness evaluation of Stewart structure
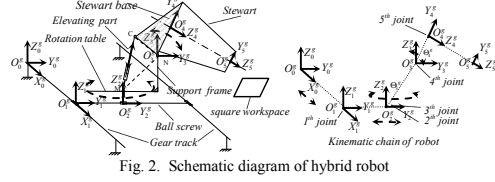
Fig. 2. Schematic diagram of hybrid robot

To evaluate the stiffness of the parallel mechanism, the parallel limb is decomposed into the up joint in the end-effector, the hydraulic limb, and the base of Stewart which consists of bearing house and U-shape joint (Universal-joint) (Fig 3).

The matrix structural analysis (MSA) is widely used to calculate the stiffness of the frame-based structure [6] [7]. By applying the MSA on the frame elements of bearing house and U-joint, the corresponding stiffness matrices have been calculated. Based on these results, the stiffness matrix of the base joint of Stewart in the i'th limb, denoted by K_{ft_i}, can be deduced by employing principle of virtual work [8]. The up-joint in the end-effector is considered to be perfectly rigid and the stiffness of the i'th hydraulic limb is represented by k_{hy_i}.

For the purpose of analysis, as demonstrated in the Fig. 4, let the coordinate frame $X_4^g Y_4^g Z_4^g$ be attached to the Stewart base in the geometric centre, the coordinate frame $X_5^g Y_5^g Z_5^g$ be attached to the moving platform, and its origin be located at the mass centre.

Hence, the stiffness matrix of the parallel mechanism in the frame $X_4^g Y_4^g Z_4^g$ is generated by taking account of the deformations in the six base joints and hydraulic limbs:

$$K_{stw} = (J_{stw} * [diag [K_{li}]]^{-1} * J_{stw}^{T})^{-1} \qquad (1)$$

where J_{stw} is the Jacobian matrix of the Stewart with $K_{li} = diag [k_{hy\_i} \quad K_{ft\_i}]$, $i = 1,2...6$.

B. Stiffness evaluation of hybrid robot

From Fig. 2, we can see that the hybrid robot is composed of the Stewart, the elevating part and the carriage base.
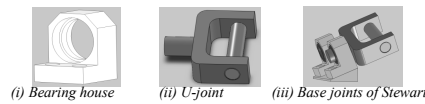
(i) Bearing house (ii) U-joint (iii) Base joints of Stewart
Fig. 3. Base of Stewart
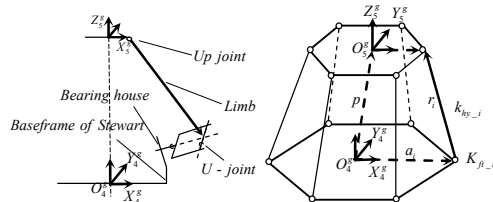
Fig. 4. Schematic diagram of the Stewart structure

Through the mechanism analysis, the elevating part is considered as a crank-slider mechanism: the Stewart base is regarded as the crank while the hydraulic limb is the actuator of the mechanism. For convenience, the stiffness of crank-slider mechanism dominated by the hydraulics driver is transformed and lumped into a virtual rotatory spring which is located at the crank joint O_3^g and denoted by $k_{\theta 4}$. For the deformations of rest joints in the carriage base, let k_{x1} be the stiffness of the robot along the gear track in the X_0^g direction, k_{y2} represent the stiffness of the ball screw in the Y_0^g direction, and $k_{\theta 3}$ denote the rotation table stiffness around the Z_2^g axis.

Analyzing the kinematics of the robot results in:

$$\left[\Delta_S^{g\,T} \quad \Theta_S^{g\,T} \right]^T = J * \Delta_q \qquad (2)$$

where $[x^r \ \Theta^r]$ is the deformation of end-effector, J the Jacobian matrix of the hybrid robot in terms of serial manner, and Δ_q the deformation vector of all joints $\Delta_q = [\Delta_S^T \ \Theta_S^T \ d_{\theta 4} \ d_{\theta 3} \ d_{y2} \ d_{x1}]^T$.

Then, employing the principle of virtual work on the hybrid robot joints leads to:

$$C = J * \chi^{-1} * J^T \qquad (3)$$

where C is the 6x6 compliance matrix of the whole hybrid robot, and $\chi = diag[K_{stw} \quad k_{\theta 4} \quad k_{\theta 3} \quad k_{y2} \quad k_{x1}]$ is a 10x10 diagonal matrix of the stiffness of all joints. The stiffness of hybrid robot is obtained as the inverse of the compliance matrix: $K = C^{-1}$.

III. INDEX OF STIFFNESS PERFORMANCE FOR HYBRID REDUNDANT ROBOT

It is well known that the stiffness reflects the certain relationship between the external force and the corresponding displacement experienced. Numerically this property is defined by a 6x6 matrix. However, it is rather difficult to distinguish the stiffness performance in terms of matrix, since it is not comparable by the means of vectors. An instinctive way to evaluate the stiffness performance is the use of interest elements inside the matrix. However, the individual element only represents the relation between the force and the deformation in a certain direction without considering the coupling effects of other terms in the matrix.

The applicable approach for the stiffness performance evaluation is to investigate the characteristics of matrix in the form of scalar, i.e., the eigenvalues, the determination, the diagonal terms as well as the condition number of matrix. Among all these usually used indicators, the eigenvalue is adopted as the most reasonable index in the application of this paper.

To Interpret the eigenvalue of the stiffness matrix geometrically, let the set of displacement vectors is "spherical", in other words, the magnitude of each displacement vector is equal to unit length, as a result, the corresponding set of force vectors is an ellipsoid, in which the lengths of the principle axes are the eigenvalues of the stiffness matrix while the related eigenvectors represent the principle axes directions. Based on this point, the minimum eigenvalue represents the minimum stiffness performance.

Since the stiffness is the most important aspect in the robot performance to ensure the accuracy of the end-effector, the minimum stiffness of the robot machine tool should be higher than a specific value over all the possible body configurations in the redundant robot. Thus, for a fixed position and orientation of end-effector in the robot, the optimum stiffness is defined by the maximum value in all the minimum eigenvalues which are depending on the different body postures. Mathematically, the optimum stiffness is described by λ_{best} in Eq. (6).

$$\{\lambda_{ji}\} = eig(K_j), i = 1, 2...6 \qquad (4)$$

$$\lambda_{min\_j} = \min\{ \lambda_{ji} \} \qquad (5)$$

$$\lambda_{best} = \max_{j \in R}\{\lambda_{min\_j}\} \qquad (6)$$

In above equations, K_j is the stiffness matrix of the redundant robot, the subscript j denotes one of the all possible body configurations (R) after the posture of end-effector is fixed; $\{\lambda_{ji}\}$ is the set of six eignvalues of matrix K_j. and λ_{min_j} represents the minimum value in the set of six eigenvalues of the stiffness matrix in current specified configuration.

Therefore, for a given position and orientation (posture) of end-effector, taking the configuration J, which is described by the driving joints parameter, as the input argument in (6), the best stiffness performance can be obtained when λ_{best} reached the maximum. Consequently, the control values for driving the joints can be obtained for the required posture in the path of end-effector. While the stiffness performances along the path of end-effector are optimized, the joints trajectory is also deduced. In the following context, the maximum λ_{best} is adopted as the optimality criteria so as to get the best joints value for a prescribe end-effector coordinate.

IV. STIFFNESS OPTIMIZATION VIA DIFFERENTIAL EVOLUTION

Considering the properties (highly nonlinear, non-differentiable) of the stiffness performance model obtained in (6), the DE is a desirable choice to be used to search the optimum stiffness performance since the advantages of DE fulfill the requirements for solving the problems concerned with this model optimization [9].

The basic DE algorithm steps can then be described as follows in Fig. 5:

285

Firstly, initialize all the populations with random positions in the search space and set the control parameters for the DE algorithm (e.g. D, NP, F, and CR). Herein, the population represents a set of driving joints values. Then check if the termination criterion is satisfied or not (e.g. number of iterations performed, or adequate fitness reached). If the criterion is not met, the new population, produced by the following algorithm: Mutation, Crossover and Selection, would be taken to be compared with the old one by calculating the cost values. Using this procedure, all individuals of the next generation are as good as or better than individuals of the current population. Repeat this process until the criterion is reached.

A Input variables and objective function for DE

The configuration determination of the redundant robot involves 10 driving joints parameter: as shown in Fig.6, let l_1 represent the linear displacement of frame $X_1^g Y_1^g Z_1^g$ along the gear track, l_2 the linear displacement of frame $X_2^g Y_2^g Z_2^g$ along the ball screw, a_3 the rotation angular of frame $X_3^g Y_3^g Z_3^g$ around the Z_2^g axis, a_4 the rotation angular of frame $X_4^g Y_4^g Z_4^g$ around the X_3^g axis; for the parallel mechanism, let h_i $(i = 1,2...6)$ denote the length of Stewart limb. The full six DOF of end-effector required by the task space can be satisfied only by the Stewart, while the rest four degrees are considered as the redundant freedoms. When the position and orientation of end-effector are fixed, the Stewart limbs length depends on the determination of redundant 4 joints values, namely l_1, l_2, a_3 and a_4. It means that the robot body configuration can be decided by the selection of a set of redundant 4 joints values if the path of end-effector is prescribed. For this reason, the independent parameters l_1, l_2, a_3 and a_4 are selected to construct the population of DE while the optimum stiffness performance λ_{best} is regarded as the objective function and demonstrated by (7):

$$\lambda_{best} = f(l_1, l_2, a_3, a_4) \qquad (7)$$

Concerning the physical constrains in the robot joints, the values of input variables in population (l_1, l_2, a_3, a_4) for the DE are limited to be in the ranges of $[0m, 4m]$, $[0m, 0.5m]$, $[0, 360^0]$ and $[-88^0, -42^0]$ respectively, and the initial values of population are assigned by randomly picking up in between the range boundaries.

In the practical application of this redundant robot machine, when the path of the end-effector is given, we firstly calculate all the 10 driving joints value at the beginning point of the path (assuming located at the point A in Fig.6) subject to the optimized stiffness performance by adopting DE algorithm. We postulate that the robot ($X_1^g Y_1^g Z_1^g$) has moved to the point B. During the machining along the end-effector path, the carriage, however, will be stopped on the track, and
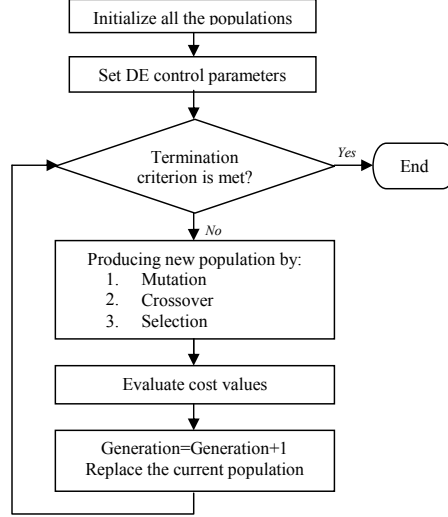

Fig.5 Flow chart of DE algorithm
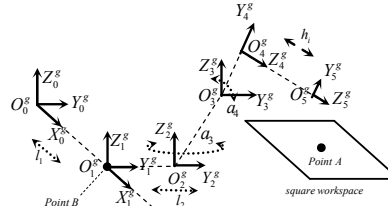
Fig.6 Kinematic chain of hybrid redundant robot

the path of end-effector will be accomplished by driving the rest 9 joints due to the lower position control accuracy on the track under the external machining force. In this case, the number of redundant freedoms is reduced to three, and the population of DE is reduced to a set of parameters l_2, a_3 and a_4. Therefore, the objective function of DE for the rest points of the path is reconstructed as (8).

$$\lambda_{best} = f(l_2, a_3, a_4) \qquad (8)$$

In another word, for the first work point A in workspace, the optimum stiffness performance is searched in the joint space of 10 freedoms. Thereafter, the robot will be working under 9 freedoms, the workspace excluding point A is reached by driving l_2, a_3, a_4 as well as the Stewart limb h_i subject to the best stiffness performance.

In order to apply the DE to optimize the objective function, several critical issues need to be determined firstly. For the control variables of DE, CR is assigned to be 0.7, F is equal to 0.8 and NP is set to be 40 for the first optimization, 30 for the rest optimization procedures. The standard deviation of

286

the population (1.0E-5) is regarded as the termination criterion.

B Optimum results

For the purpose of demonstration, the best stiffness performance for a random point within the workspace is investigated. Herein, postulate the point of end-effector (frame $X_5^g Y_5^g Z_5^g$) located at the point A (Fig. 6) with the coordinate of $[1.5m, 1.0m, 0m, 150^0, 0, -150^0]^T$ in which the first three entries specify the position of end-effector while the rest three entries specify the orientation by means of Roll-Pitch-Yaw angles in the global frame $X_0^g Y_0^g Z_0^g$. The convergence process for searching the optimum stiffness is illustrated in Fig 7.

It is observed that the DE reaches the convergence after around 50 iterations. In addition, the best input parameters are obtained as $l_1 = 1.8682\,m$, $l_2 = 0.3621\,m$, $a_3 = 30.0206^0$, $a_4 = -74.9323^0$ respectively. The length of Stewart limb could be calculated by the inverse kinematics.

In following step, we extend the workspace from the beginning point A to a 200x200mm^2 square and let point A locate at the geometric centre of this area, the height of the end-effector and its orientation maintain the same as what in point A. Thereafter, applying the DE to search the best stiffness with the objective function (8) over this specific workspace, the optimum stiffness surface is found and shown in Fig 8.

In Fig 8, the x axis direction is parallel to the track while the y axis direction is perpendicular to the track. It is found that the stiffness performance of point A is the best in the 200x200mm^2 plane workspace, because the best stiffness of point A is searched in the joint space of 10 freedoms while the others are searched in the joint spaces of 9 freedoms due to the fixed carriage position on the tack. The stiffness decreases along both positive and negative directions of x axis when the end-effector moves away from point A, because the displacement of the end-effector along the track is contributed mainly by the stretching of Stewart, and the stiffness of Stewart becomes weaker if the limb stretches long. The stiffness also decreases along the both directions of y axis, but the change is much slighter compared with the one in the x axis, because the displacement along the y axis is implemented mainly by the ball screw which has much smaller stiffness deviation than the hydraulic limb's in the Stewart.

V. TRAJECTORY PLANNING EXAMPLES

In the following example, the end-effector moves along a straight line of 200mm length which is parallel to the track on the xy plane in global frame $X_0^g Y_0^g Z_0^g$ (Fig 9).The speed of the end-effect is set to 2mm/s. The middle point of the path is selected as the optimization initial point under 10 joints freedom, the coordinate of middle point is set to $[1.5m, 1.0m, 0m, 150^0, 0, -150^0]^T$ with respect to the global frame.
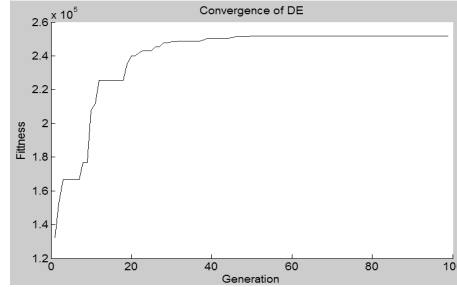
Fig.7 Convergence of DE for searching the optimum stiffness
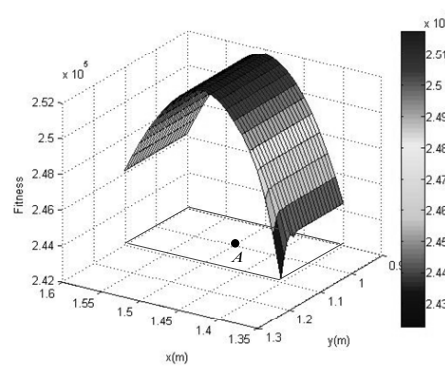
Fig 8 Optimum stiffness surface over the 200x200mm^2 square
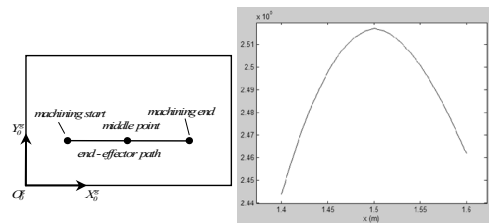
Fig 9 Straight line path and best stiffness along the path

Although the optimization of joint trajectory begins from the middle point of the path, in the practical machining process the robot end-effector starts to work from one end of the line. Adopting DE algorithm to optimize the stiffness performance along the straight line-path of end-effector, the corresponding joints trajectories are obtained and plotted in Fig 10.

From Fig.10(i), the trajectory of the first joint maintains constant because the carriage base is fixed on the track after the first optimization.

287

(i). Linear position trajectory of joints parallel to the tack and vertical to the tack

(ii). Rotation trajectory of rotation table and Stewart base

(iii). Linear position trajectory of limb1 and limb2 in Stewart

(iv). Linear position trajectory of limb3 and limb4 in Stewart
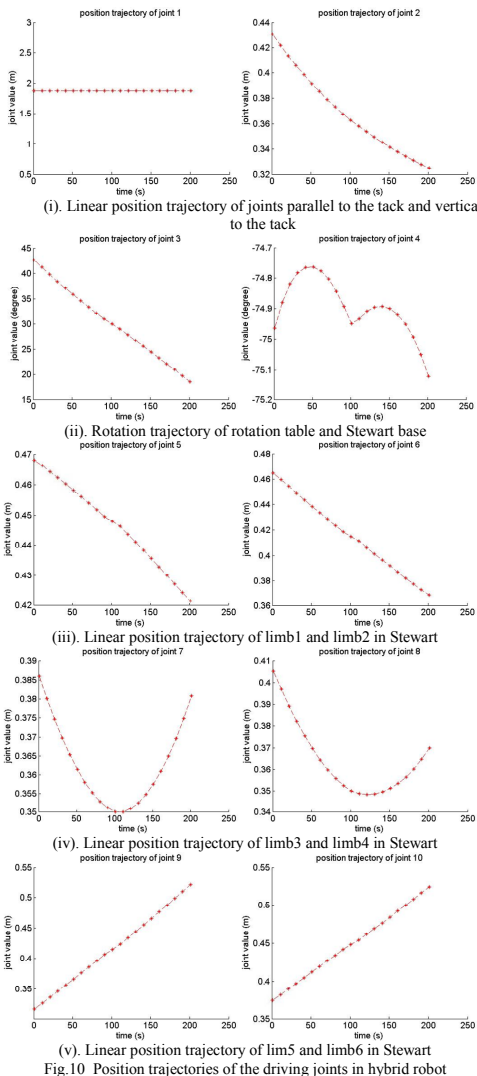
(v). Linear position trajectory of lim5 and limb6 in Stewart
Fig.10 Position trajectories of the driving joints in hybrid robot

VI. CONCLUSIONS

Due to the redundant kinematics in the hybrid serial-parallel robot machine, when the coordinate of the end-effector is given, the robot body configuration is underconstrained. Meanwhile, the stiffness of end-effector varies depending on the body configuration over all the possible body configurations. Taking the redundant driving

joints values as the input parameters in DE algorithm and the best stiffness performance as the optimized objective, the joints driving values for the robot are obtained. Repeating such procedure along the path, the optimized joints trajectories are finally plotted while the end-effector is subject to the best stiffness performance along the machining path.

In this paper, if the end-effector path is prescribed, the corresponding joints trajectories are deduced subject to the best stiffness performance. However, such trajectory only contains the position information for robot controlling, because the stiffness performance only reflects the static property of the robot. In order to control the robot in the practical machining, the velocity and acceleration of the driving joints are needed to be investigated. The future work will concentrates on the velocity and acceleration as constrain condition in the trajectories planning subject to the stiffness, energy-efficient and time-efficient strategy [10] – [12].

The main contribution of this paper is to have proposed a method for the controlling of kinematic redundant robot machine based upon the best stiffness performance.

REFERENCES

[1] H. Wu, P. Pessi, H. Handroos, "Assembling and repairing for ITER vacuum vessel with mobile parallel robot", Fusion Engineering, 2007.
[2] Jiri Tlusty, John Ziegert and Shannon Ridgeway. "Fundamental comparison of the use of serial and parallel kinematics for machines tools". CIRP Annals – Manufacturing Technology. Volume 48, issue 1, 1999, pages 351-356.
[3] J. Hesseleach, M. B. Helm and H. Kunzmann. "Workspace enlargement for parallel kinematic machines". CIRP Annals – Manufacturing Technology, volume 52, issue 1, 2003, pages 343-346.
[4] Günter Pritschow. "Parallel kinematic machines (PKM) –limitations and new solutions". CIRP Annals – Manufacturing Technology. Volume 49, issue 1, 2000, pages 275-280.
[5] B. S. El-Khasawneh and P. M. Ferreira, "Computation of stiffness and stiffness bounds for parallel link manipulator". Int. J. Machine Tools and Manufacture, vol. 29, no. 2, pp. 321-342, 1999.
[6] Jamal J. Azar. Matrix Structural Analysis. Pergamon press inc, 1972.
[7] D. Deblaise, X. Hernot and P. Maurine, "A systematic analytical method for PKM stiffness matrix calculation". Proceedings of the IEEE International Conference on Robotics and Automation, Orlando, Florida, May, 2006.
[8] Ming Li, Huapeng Wu and Heikki Handroos. "Static stiffness modeling of a novel hybrid redundant robot machine". Fusion Engineering, 2011, in press.
[9] Rainer Storn and Kenneth Price. "Differential evolution – a simple and efficient heuristic for global optimization over continuous spaces". Journal of Global Optimization. 11: 241-259,1997.
[10] A. Gasparetto, V. Zanotto. "Optimal trajectory planning for industrial robots". Advances in Engineering Software, Volume 41, Issue 4, April 2010, Pages 548-556.
[11] Chun-Ta Chen, Te-Tan Liao. "A hybrid strategy for the time- and energy-efficient trajectory planning of parallel platform manipulators". Robotics and Computer-Integrated Manufacturing, Volume 27, Issue 1, February 2011, Pages 72-81.
[11] Amar Khoukhi, Luc baron, Marek Balazinski. "Constrained multi-objective trajectory planning of parallel kinematic machines". Robotics and Computer-Integrated Manufacturing, Volume 25, Issues 4-5, August-October 2009, Pages 756-769.
[12] Ingo Pietsch, Carlos Bier, Oliver Becker and Jurgen Hesselbach. "How to assign time-optimal trajectories to parallel robots – an adaptive jerk-limited approach". ABCM symposium Series in Mechatronics, Vol 2, pp 174 – 181.

Publication V

Ming Li, Huapeng Wu, Heikki Handroos

Stiffness modelling of hybrid parallel robot machine

Reprinted from
Proceeding of ICMC 2010, Volume 54, Pages 743-750, International Chemnitz Manufacturing
Colloquium, Chemnitz, Germany, September 29-30, 2010, with permission from CIRP

Stiffness modeling of hybrid parallel robot machine

Li M, Wu H, Handroos H

Laboratory of intelligent machines, Lappeenranta university of technology, Lappeenranta, Finland

Abstract

This paper proposes a stiffness modeling method for a novel 10 degree-of-freedom hybrid parallel robot machine which consists of a parallel mechanism and a movable serial basement. The stiffness matrix of the basic element in the robot is evaluated by matrix structural analysis and the stiffness of the whole robot is evaluated by employing the virtual joint method and the principle of virtual work. The stiffness analysis of parallel mechanism is investigated by taking account of both hydraulic limb translational deformation and the joint deformation. The obtained stiffness model of the hybrid robot is analytical and can be used to optimize the trajectory of machining.

1   Introduction

Stiffness is a very important property of the robot machine which can directly affect the performance of machining. During recent years, parallel robots have been prevailing in industrial applications for having higher structural rigidity compared with serial manipulators. However, the stiffness of parallel robot cannot be finite high.

The robot under study is a hybrid parallel robot machine named IWR [1] which merges the advantages of both the serial and parallel mechanisms (Stewart platform) as shown in Fig. 1. To investigate the stiffness matrix of the robot, several approaches have already been proposed in the robot engineering, such as finite

element analysis [2], the matrix structural analysis (MSA) [3], and the virtual joint method (VJM) [4]. In addition, the analytical method of calculating the Jacobian matrix of the robot is also widely used.
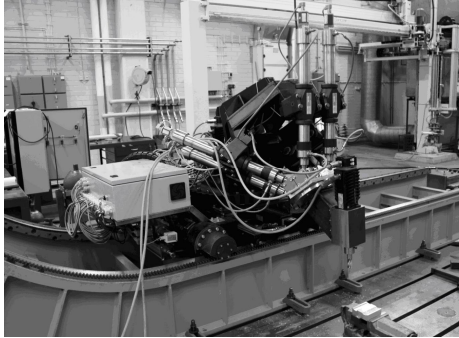

**Figure 1:** *10DOF hybrid robot in Lappeenranta University of Technology*

In our study, the MSA approach is employed to calculate the stiffness of the basic element in the robot, such as U-joint, bearing house, etc. It provides an analytical stiffness matrix as a function of the structure posture according to the global coordinate; the VJM method combined with the principle of virtual work is also applied to evaluate the stiffness of the structure, such as feet composed of basic elements in the parallel mechanism.

2   Description of matrix structural analysis

The analytical stiffness model developed in this paper is based on matrix structural analysis. In order to illustrate the application of the MSA on multi-beam structure, the stiffness modeling of bearing house and U-joint in the foot of Stewart platform in our robot is taken into account (Fig. 2).

(i) Bearing house   *(ii) U-joint*   *(iii) Foot of Stewart*

Figure 2: *bearing house, U-joint and foot of Stewart*

For the convenience of analyzing, the bearing house, U-joint and the foot are simplified into the frame structure described in Fig. 3.

(i) Bearing house (ii) U-joint (iii) Foot of Stewart
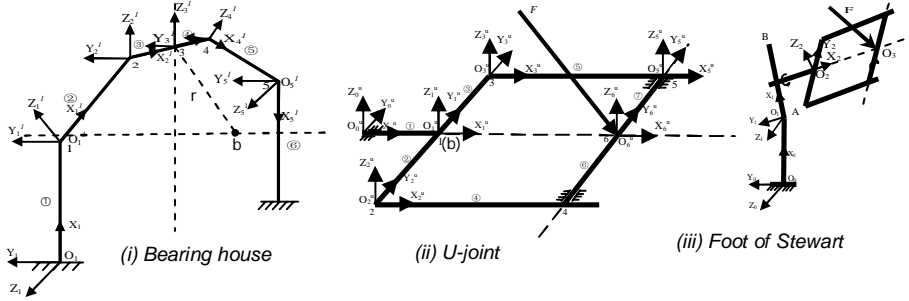
Figure 3: *Schematic diagram of bearing house and U-joint in the foot of Stewart platform*

The first step for applying the MSA method is to define the elements of the structure and their nodes. Each element of the structure is defined by a number enclosed with a circle, and its two nodes are indentified by two numbers.

In Fig. 3(*iii*), O_0A is the base frame of Stewart platform, ABO_2 the frame of bearing house including the U-joint shaft, and O_2O_3 the frame of U-joint. Firstly, we decompose the bearing house and U-joint into separate beams in Figs. 3*(i) and 3(ii)*, and then we can get the single stiffness matrix of each beam according to application of MSA on single beam [3], finally we assemble all these stiffness matrices according to their nodes connectivity by using superposition principle and express in the local coordinate. Herein, the stiffness modeling of U-joint is stated in Eq. (1) as follows:

$$
\begin{bmatrix} F_1 \\ F_2 \\ F_3 \\ F_4 \\ F_5 \\ F_6 \end{bmatrix} = \begin{bmatrix}
K_{11}^2 + K_{11}^3 & K_{12}^2 & K_{13}^3 & O & O & O \\
K_{21}^2 & K_{22}^2 + K_{22}^4 & O & K_{24}^4 & O & O \\
K_{31}^3 & O & K_{33}^3 + K_{33}^5 & O & K_{35}^5 & O \\
O & K_{42}^2 & O & K_{44}^4 + K_{44}^6 & O & K_{46}^6 \\
O & O & K_{53}^5 & O & K_{55}^5 + K_{55}^7 & K_{56}^7 \\
O & O & O & K_{64}^6 & K_{65}^7 & K_{66}^6 + K_{66}^7
\end{bmatrix} \begin{bmatrix} \Delta_1 \\ \Delta_2 \\ \Delta_3 \\ \Delta_4 \\ \Delta_5 \\ \Delta_6 \end{bmatrix}
$$

(1)

where vector F_i is the external force exerting on the node i, Δ_i the corresponding deformation of node i, O the 6x6 zero matrix and K_{ij}^n the 6x6 stiffness matrix of the single beam.

In this example, the deformation of Beam ○;1 in the U-joint is not taken into account, because the beam ○;1 (U-joint shaft) is assembled into the bearing house in the foot and considered as rigid.

Equation (1) is obtained under the assumption that the whole structure of the U-joint is considered as a rigid frame. However, there are two rotational freedoms in the U-joint and the force acting on Node 6 is always constrained in the plane which is crossing the line of $O_1^u O_6^u$ and perpendicular to the U-joint plane in Fig. 3.

Therefore, by employing the static condensation technique, further simplification on Eq. (1) is obtained as

$$F_6 = (K_{22} - K_{21} K_{11}^{-1} K_{12}) \Delta_6 \qquad (2)$$

where K_{11} stands for the left-upper matrix block stroke with the dash line in Eq. (1), K_{12} stands for the right-upper matrix block, K_{21} stands for the left-lower matrix block and K_{22} stands for the right-lower matrix block.

In the same way, by using the static condensation method and substituting the physical parameters of the U-joint into Eq. (2) it gives

$$F_u = K_u * \Delta_u \qquad (3)$$

where $F_u = [f_{u\_x} \ f_{u\_z}]^T$ and $\Delta_u = [d_{u\_x} \ d_{u\_z}]^T$ represent the external force and the corresponding deformation in Node 6 of U-joint in its own frame $X_1^u Y_1^u Z_1^u$, and K_u stands for the 2x2 stiffness matrix of Node 6 in U-joint.

Similarly, by substituting the physical parameters of the bearing house, the stiffness of the point b in the bearing house is calculated and expressed in the frame $X_1 Y_1 Z_1$ in Eq. (4) as follows

$$F_{bearh} = K_{bearh} * \Delta_{bearh} \qquad (4)$$

Where $F_{bearh} = [f_{bearh\_y} \ f_{bearh\_z} \ m_{bearh\_x} \ m_{bearh\_z}]^T$ and $\Delta_{bearh} = [d_{bearh\_y} \ d_{bearh\_z} \ \theta_{bearh\_x} \ \theta_{bearh\_z}]^T$ represent the external force and the corresponding deformation in Node b of the bearing house in frame $X_1 Y_1 Z_1$. The force f_{bearh_x} and the moment m_{bearh_y} are equal to zero and suppressed in the equation since the force f_{bearh_x} acting on the base frame causes no deformation and the moment m_{bearh_y} does not exist around the axis of the bearing house.

3 Stiffness modeling of parallel mechanism

To evaluate the stiffness of the parallel mechanism, the parallel mechanism is decomposed into the basement frame, the bearing house in the foot, the U-joint in the foot, the hydraulic limb and the up joint in the end-effector (Fig. 4). Among these components, the basement frame is considered as rigid structure; the bearing house and the U-joint comprise the foot of Stewart platform, and their stiffness

matrices are configuration-independent separately, but the stiffness of the feet of Stewart platform is configuration-dependent as a function of the orientation of the hydraulic limb; the stiffness of the hydraulic limb is also configuration-dependent as the function of its length; the up-joint in the end-effector is considered as rigid.
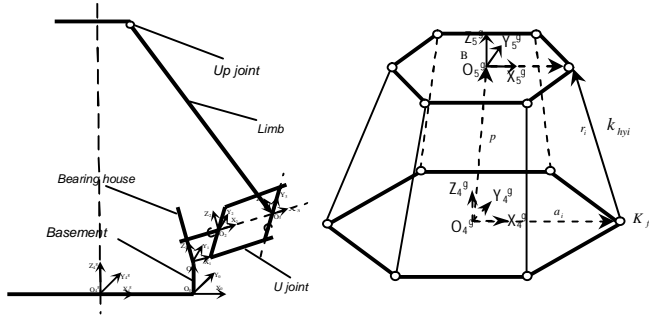

Figure 4: *Schematic diagram of the Stewart structure*

3.1 Stiffness evaluation of foot in parallel mechanism

The composition of the foot by the bearing house and the U-joint is considered to be in a serial manner. Herein, its stiffness is investigated by employing the virtual joint method and the principle of virtual work. The kinematic chain of the foot is shown in Fig. 5.
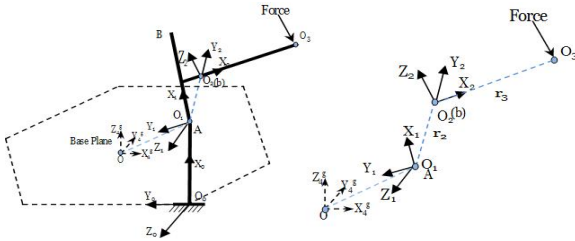
Figure 5: *Kinematic chain of the foot in the Stewart*

The hexagon in the figure is the basement of the Stewart, in which the frame $X_4^g Y_4^g Z_4^g$ is defined as the local reference coordinate. Under the external force F_{ft} applied to the point O_3, the compliance of the foot will cause the point O_3 to experience a twist $[\Delta_{ft}^T \ \Theta_{ft}^T]^T$ in terms of translational and rotational deformations in the frame $X_4^g Y_4^g Z_4^g$. Applying the kinematic relationship in the foot results

$$\Delta_{ft} = \begin{bmatrix} J_{u\_dx} & J_{u\_dz} & J_{bearh\_dy} & J_{bearh\_dz} & J_{bearh\_\theta x} & J_{bearh\_\theta z} \end{bmatrix} * \begin{bmatrix} \Delta_u^T & \Delta_{bearh}^T \end{bmatrix}^T \quad (5)$$

where Δ_u and Δ_{bearh} represent the deformations of the U-joint and the bearing house and J_i stands for the Jacobian of the ith local joint deformation.

Employing the principle of virtual work in the foot kinematic chain leads to

$$\left[\delta\Delta_{ft}{}^{T} \right] * \left[F_{ft} \right] = \left[\delta\Delta_u{}^{T} \quad \delta\Delta_{bearh}{}^{T} \right] * \begin{bmatrix} \left[K_u \right]_{2\times2} & O_{2x4} \\ O_{4x2} & \left[K_{bearh} \right]_{4\times4} \end{bmatrix} * \left[\Delta_u{}^{T} \quad \Delta_{bearh}{}^{T} \right]^{T} \qquad (6)$$

where, δ represents the virtual displacement (small perturbation) on the basis of the deformations, K_u and K_{bearh} represent the stiffness matrices of the U-joint and bearing. Substituting the Eq. (5) into (6) and simplifying the result gives

$$F_{ft} = K_{ft} * \Delta_{ft} \qquad (7)$$

$$K_{ft} = (J_{ft} * \begin{bmatrix} K_u & O_{2x4} \\ O_{4x2} & K_{bearh} \end{bmatrix}^{-1} * J_{ft}{}^{T})^{-1} \qquad (8)$$

where J_{ft} is equal to [J_{u_dx} J_{u_dz} J_{bearh_dy} J_{bearh_dz} $J_{bearh\_\theta x}$ $J_{bearh\_\theta z}$]. For convenience, the symbol K_{ft_i} is used to stand for the stiffness matrix of ith foot in Stewart in the later part of this paper.

3.2 Stiffness of hydraulic limb

The assembly of components in the hydraulic limb is deemed to be in serial, and its stiffness varies depending on the cylinder stroke:

$$K_{hy} = \frac{A_1{}^2}{(A_1 * x + V_h)/B_w + A_1 * x/B_c + V_h/B_h} + \frac{A_2{}^2}{(A_2 * (l-x) + V_h)/B_w + A_2 * (l-x)/B_c + V_h/B_h} \qquad (9)$$

where A is the area, V the volume, x the cylinder stroke, and i the cylinder length. B_w, B_c and B_h are the bulk modulus of water, cylinder and hose respectively. Subscripts 1 and 2 denote the corresponding chambers of the double-acting cylinder.

3.3 Stiffness evaluation of parallel mechanism

In Fig. 4, the coordinate frame $X_4{}^9Y_4{}^9Z_4{}^9$ is attached to the basement in the geometric centre. The coordinate frame $B(X_5{}^9Y_5{}^9Z_5{}^9)$ is attached to the moving

platform, and its origin is located at the mass centre. By taking account of the deformations in the feet and hydraulic limbs, the stiffness matrix of the parallel mechanism is obtained by the same way as Eq. (8)

$$K_{stw} = (J_{stw} * [diag [K_{li}]]^{-1} * J_{stw}^{T})^{-1} \qquad (10)$$

where J_{stw} is the Jacobian matrix of the Stewart, and $K_{li}=diag[K_{hy\_i} K_{ft\_i}]$.

4 Stiffness modeling of hybrid robot

The schema of the hybrid robot, shown in Fig. 6, is composed of a parallel structure, a support frame, an elevating part and a basement.
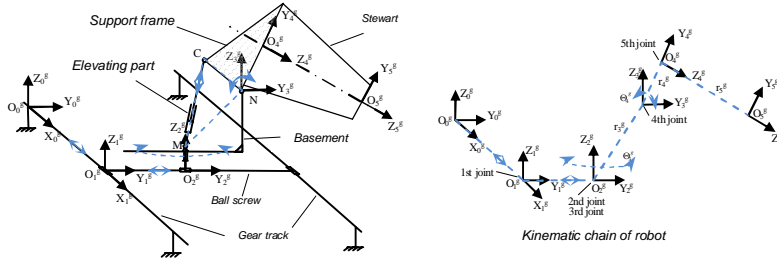

Figure 6: *Schematic diagram of the hybrid robot and its kinematic chain*

Through the mechanism analysis, the elevating part is considered as a crank-slider mechanism, the base frame of Stewart platform is regarded as the crank while the hydraulic limb is regarded as the actuator of the mechanism. The stiffness of the actuator is transformed into the local compliant spring located at the crank joint and denoted by $k_{\theta4}$. The stiffness of the gear pair in the track is denoted by k_{x1} while the stiffness of the rotation around Z_2^g axis is denoted by $k_{\theta3}$ which is driven by an epicycle gear. The stiffness of the ball screw is the sum of the nut and shaft stiffness, denoted by k_{y2}.

Analyzing the kinematics of the robot results in

$$\begin{bmatrix} \Delta_5^{g\,T} & \Theta_5^{g\,T} \end{bmatrix}^T = J * \Delta_q \qquad (11)$$

where $\begin{bmatrix} \Delta_5^{g\,T} & \Theta_5^{g\,T} \end{bmatrix}^T$ is the deforamtion of end-effector, J the Jacobian matrix of the hybrid robot, and Δ_q the vector of each joint deformations $\Delta_q=[\Delta_5\,\Theta_5\,d\theta_4\,d\theta_3\,dy_2\,dx_1]$.

Employing the principle of virtual work on the hybrid robot joints leads to

$$C = J * \chi^{-1} * J^T$$

(12)

where C is the 6x6 compliance matrix of the whole hybrid robot, and χ=diag[K_{stw} $k_{\theta 4}$ $k_{\theta 3}$ k_{y2} k_{x1}] is an 10X10 diagonal matrix consisted of the stiffness of each joint. The stiffness of the whole hybrid robot is obtained equal to the inverse of the compliance matrix, $K=C^{-1}$.

5   Conclusion

This paper presents a stiffness modeling method for a hybrid robot machine. In the built model, all the deformations of the foot joints in the Stewart platform are taking into account. By applying the MSA, the VJM and the principle of virtual work, the analytical stiffness of the robot can be achieved, and another advantage of this method is the low calculation consumption.

Literature

[1]   Pekka Pessi, Huapeng Wu, Heikki Handroos and Lawrence Jones.: A Mobile Robot with Parallel Kinematics to Meet the Requirements for Assembling and Machining the ITER Vacuum Vessel. Fusion Engineering and Design 82 (2007) 2047-2054.

[2]   G. Piras, W.L. Cleghorn and J.K. Mills.: Dynamic Finite-Element Analysis of A Planar High-Speed, High-Precision Parallel Manipulator with Flexible Links. Mechanism and Machine Theory, 40(7) (2005), pp. 849-862.

[3]   Dominique Deblaise, Xavier Hernot and Patrick Maurine.: A Systematic Analytical Method for PKM Stiffness Matrix Calculation. Proceedings of the 2006 IEEE International Conference on Robotics and Automation, Orlando, Florida, May, 2006.

[4]   C.M. Gosselin, and D. Zhang.: Stiffness Analysis of Parallel Mechanisms Using A Lumped Model. Int. J. of Robotics and Automation, 17(1) (2002), pp. 17-27.

ACTA UNIVERSITATIS LAPPEENRANTAENSIS

570.   KALLIO, SAMULI. Modeling and parameter estimation of double-star permanent magnet synchronous machines. 2014. Diss.

571.   SALMELA, ERNO. Kysyntä-toimitusketjun synkronointi epävarman kysynnän ja tarjonnan toimintaympäristössä. 2014. Diss.

572.   RIUNGU-KALLIOSAARI, LEAH. Empirical study on the adoption, use and effects of cloud-based testing. 2014. Diss.

573.   KINNARINEN, TEEMU. Pressure filtration characteristics of enzymatically hydralyzed biomass suspensions. 2014. Diss.

574.   LAMMASSAARI, TIMO. Muutos kuntaorganisaatiossa – tapaustutkimus erään kunnan teknisestä toimialasta. 2014. Diss.

575.   KALWAR, SANTOSH KUMAR. Conceptualizing and measuring human anxiety on the Internet. 2014. Diss.

576.   LANKINEN, JUKKA. Local features in image and video processing – object class matching and video shot detection. 2014. Diss.

577.   AL-SAEDI, MAZIN. Flexible multibody dynamics and intelligent control of a hydraulically driven hybrid redundant robot machine. 2014. Diss.

578.   TYSTER, JUHO. Power semiconductor nonlinearities in active du/dt output filtering. 2014. Diss.

579.   KERÄNEN, JOONA. Customer value assessment in business markets. 2014. Diss.

580.   ALEXANDROVA, YULIA. Wind turbine direct-drive permanent-magnet generator with direct liquid cooling for mass reduction. 2014. Diss.

581.   HUHTALA, MERJA. PDM system functions and utilizations analysis to improve the efficiency of sheet metal product design and manufacturing. 2014. Diss.

582.   SAUNILA, MINNA. Performance management through innovation capability in SMEs. 2014. Diss.

583.   LANA, ANDREY. LVDC power distribution system: computational modelling. 2014. Diss.

584.   PEKKARINEN, JOONAS. Laser cladding with scanning optics. 2014. Diss.

585.   PELTOMAA, JYRKI. The early activities of front end of innovation in OEM companies using a new FEI platform as a framework for renewal. 2014. Diss.

586.   ROZHANSKY, IGOR. Resonant tunneling effects in semiconductor heterostructures. 2014. Diss.

587.   PHAM, THUY DUONG. Ultrasonic and electrokinetic remediation of low permeability soil contaminated with persistent organic pollutants. 2014. Diss.

588.   HOKKANEN, SANNA. Modified nano- and microcellulose based adsorption materials in water treatment. 2014. Diss.

589.   HINKKANEN, JUHA. Cooperative strategy in emerging markets – analysis of interfirm R&D cooperation and performance in Russian manufacturing companies. 2014. Diss.

590.   RUSKOVAARA, ELENA. Entrepreneurship education in basic and upper secondary education – measurement and empirical evidence. 2014. Diss.

591. IKÄHEIMONEN, TUULI. The board of directors as a part of family business governance – multilevel participation and board development. 2014. Diss.

592. HAJIALI, ZUNED. Computational modeling of stented coronary arteries. 2014. Diss.

593. UUSITALO, VILLE. Potential for greenhouse gas emission reductions by using biomethane as road transportation fuel. 2014. Diss.

594. HAVUKAINEN, JOUNI. Biogas production in regional biodegradable waste treatment – possibilities for improving energy performance and reducing GHG emissions. 2014. Diss.

595. HEIKKINEN, JANNE. Vibrations in rotating machinery arising from minor imperfections in component geometries. 2014. Diss.

596. GHALAMCHI, BEHNAM. Dynamic analysis model of spherical roller bearings with defects. 2014. Diss.

597. POLIKARPOVA, MARIIA.Liquid cooling solutions for rotating permanent magnet synchronous machines. 2014. Diss.

598. CHAUDHARI, ASHVINKUMAR. Large-eddy simulation of wind flows over complex terrains for wind energy applications. 2014. Diss.

599. PURHONEN, MIKKO. Minimizing circulating current in parallel-connected photovoltaic inverters. 2014. Diss.

600. SAUKKONEN, ESA. Effects of the partial removal of wood hemicelluloses on the properties of kraft pulp. 2014. Diss.

601. GUDARZI, DAVOOD. Catalytic direct synthesis of hydrogen peroxide in a novel microstructured reactor. 2014. Diss.

602. VALKEAPÄÄ, ANTTI. Development of finite elements for analysis of biomechanical structures using flexible multibody formulations. 2014. Diss.

603. SSEBUGERE, PATRICK. Persistent organic pollutants in sediments and fish from Lake Victoria, East Africa. 2014. Diss.

604. STOKLASA, JAN. Linguistic models for decision support. 2014. Diss.

605. VEPSÄLÄINEN, ARI. Heterogenous mass transfer in fluidized beds by computational fluid dynamics. 2014. Diss.

606. JUVONEN, PASI. Learning information technology business in a changing industry landscape. The case of introducing team entreneurship in renewing bachelor education in information technology in a university of applied sciences. 2014. Diss.

607. MÄKIMATTILA, MARTTI. Organizing for systemic innovations – research on knowledge, interaction and organizational interdependencies. 2014. Diss.

608. HÄMÄLÄINEN, KIMMO. Improving the usability of extruded wood-plastic composites by using modification technology. 2014. Diss.

609. PIRTTILÄ, MIIA. The cycle times of working capital: financial value chain analysis method. 2014. Diss.

610. SUIKKANEN, HEIKKI. Application and development of numerical methods for the modelling of innovative gas cooled fission reactors. 2014. Diss.